Ore Geology Reviews 127 (2020) 103827

Contents lists available at ScienceDirect

Ore Geology Reviews

journal homepage: www.elsevier.com/locate/oregeorev

Geochemistry and mineralogy of rare earth elements in high-phosphorus ooidal ironstones: A case study of the Kamysh-Burun deposit (Azov–Black Sea iron Province)

Ella V. Sokol [a], Svetlana N. Kokh [a,*], Olga A. Kozmenko [a], Anna V. Nekipelova [a], Maxim Rudmin [b], Pavel V. Khvorov [c], Dmitry A. Artemyev [c,d]

[a] Sobolev Institute of Geology and Mineralogy, Siberian Branch of the Russian Academy of Sciences, 3 Koptyug Avenue, Novosibirsk 630090, Russia
[b] Division for Geology, Tomsk Polytechnic University, 30 Lenin Avenue, Tomsk 634050, Russia
[c] South Urals Federal Research Center of Mineralogy and Geoecology, Urals Branch, Russian Academy of Sciences, Institute of Mineralogy, Ilmeny Reserve Area, Miass 456317, Russia
[d] South Urals State University, Lenin av., 76, Chelyabinsk 454080, Russia

ARTICLE INFO

Keywords:
Ooidal ironstones
Rare earth elements
Fe^{3+}-(oxy)hydroxides
Rhabdophane-tristramite
Vivianite
Anapaite

ABSTRACT

This study is aimed at characterizing the distribution and speciation of the rare earth elements and yttrium (REE + Y) in ooidal ironstones from the Kamysh-Burun deposit (Kerch Peninsula), wit h implications for the depositional environments and contributions of different REE + Y carriers to the ore budget. The Lower Pliocene ooidal ironstone sequence of the so-called Kerch ores, up to 15 m thick, occupies an area of 28 km^2. The ore sequence lies between Miocene – Lower Pliocene shell limestones and Upper Pliocene – Pleistocene sandy and clayey sediments and consists of horizontal ooidal ironstone beds composed mainly of goethite and X-ray amorphous Fe^{3+}-(oxy)hydroxides intercalated with siderite and/or rhodochrosite beds. Iron is a main component in ooidal ironstones (50.03–66.19 wt% Fe_2O_3 and ≤1.61 wt% FeO), as well as in fresh carbonate ores (~34 wt% FeO and ≤14.70 wt% Fe_2O_3). The Kerch ores contain up to 4.59 wt% P_2O_5 and show significant positive correlation between P and Fe ($r = 0.75$). The bulk ore samples and their coarse (1–10 mm) fractions are goethite-dominated and have similar phase, major- and trace-element, and REE compositions. The fine (<1 mm) fractions are poorer in goethite and P_2O_5 but enriched in SiO_2, Al_2O_3, Ti, Zr, Y, and Th due to greater percentages of Fe-saponite and fine detrital matter (including very scarce rutile, zircon, monazite, and xenotime). The average ΣREE values of 400 ppm in bulk ooidal ironstones and 405 ppm in the coarse fractions markedly exceed those in the Post Archean Australian Shale (PAAS). They have similar PAAS-normalized REE + Y patterns, with moderate enrichment in middle REE (MREE), minor Ce* (0.67–1.09), and moderate negative Y* anomalies (0.57–0.70). The fine ore fractions are markedly enriched in ΣREE (*Xav* = 858 ppm) mainly due to the presence of authigenic light REE phosphates of rhabdophane-tristramite series with Ce > La ≈ Nd ≈ Ca > Pr > Sm. The ΣREE content in fresh carbonate ores is below that in PAAS (*Xav* = 103 ppm), but approaches the latter in oxidized crusts (*Xav* = 178 ppm). The Kerch ironstones also contain REE-poor early-diagenetic Fe^{2+} phosphate vivianite (ΣREE *Xav* = 0.93 ppm) and Ca-Fe^{2+} phosphate anapaite (ΣREE Xav = 6.95 ppm) with typical seawater REE + Y distributions. The ooidal ironstones show MREE-enriched patterns with distinct negative Y* anomalies, which reveals Fe^{3+}-(oxy)hydroxides as chief carriers of adsorbed REE (mainly MREE). The Kerch ironstones accumulated REE progressively due to hysteretic dissolution and precipitation of Fe^{3+}-(oxy)hydroxides in oscillating redox conditions. The diagenetic source of REE stored in ooidal goethite ironstones was inferred from the PAAS-normalized values: Ce_N/Ce_N^* *vs* Nd and Ce_N/Ce_N^* *vs* Y_N/Ho_N discrimination diagrams. In general, the REE + Y budget of the Kerch ooidal ironstones mainly formed during early diagenesis and scavenging from pore water, with a minor contribution of siliciclastic inputs, in the absence of hydrothermalism.

* Corresponding author.
E-mail address: s.n.kokh@gmail.com (S.N. Kokh).

https://doi.org/10.1016/j.oregeorev.2020.103827
Received 11 April 2020; Received in revised form 28 September 2020; Accepted 4 October 2020
Available online 10 October 2020

1. Introduction

The rare earth elements (REE) are a group of fourteen naturally occurring lanthanides and yttrium, which show similar physical and chemical properties. The REE have unique catalytic, metallurgical, nuclear, electrical, magnetic and luminescent properties, and their strategic importance shows up in their use in emerging and diverse technologies. Applications range from routine (e.g., lighter flints, glass polishing mediums, or car alternators) to high technology (lasers, magnets, batteries, fiber-optic telecommunication cables), green energy, defense, and those with futuristic purposes (high-temperature superconductivity, storage and transport of hydrogen, and energy efficiency issues) (Wall, 2014; Emsbo et al., 2015; Krishnamurthy and Gupta, 2005; Balaram, 2019).

The REEs are informally subdivided into light REE (LREE, La through Nd) and heavy REE which start with Sm, followed by Eu through to Lu. The heavy REE are sometimes subdivided further into middle REE (MREEs comprising Sm, Eu, Gd, Tb and Dy) with the remainder of the group, Ho to Lu, referred to as the heavy REE (HREE) (Rollinson, 1993). HREE are particularly important to emerging technologies, but these very elements are scarce in natural rocks. The REE upper crustal abundances vary from Ce at 63 ppm to Lu at 0.31 ppm (Rudnick and Gao, 2003) and their budget in the overwhelming majority of REE minerals (96%) is dominated by Ce, Y, La, or Nd (Chakhmouradian and Wall, 2012). A number of geological processes can lead to concentration of rare earth minerals in specific types of igneous and metasomatic rocks or sediments and to enrichment in either LREEs or HREEs by fractionation within the REE series (Bao and Zhao, 2008; Chakhmouradian and Zaitsev, 2012; Kynicky et al., 2012; Mariano and Mariano, 2012; Williams-Jones et al., 2012). Over the past two decades the global demand for REE has increased significantly and almost the entire world's REE supply (~97%, or 120–130 kt REE oxides in 2006–2010) comes from China, with 40–50% of this production contributed by the giant Fe–REE–Nb carbonatite deposit at Bayan Obo that sources 80% of the world's LREEs, but is low in HREEs (Hatch, 2012; Kynicky et al., 2012; Fan et al., 2016). The ion-adsorption clay-type deposits of South China, although being small and low-grade, dominate the HREE market because they are enriched in HREE and are cheap to mine and process (Hatch, 2012; Kynicky et al., 2012).

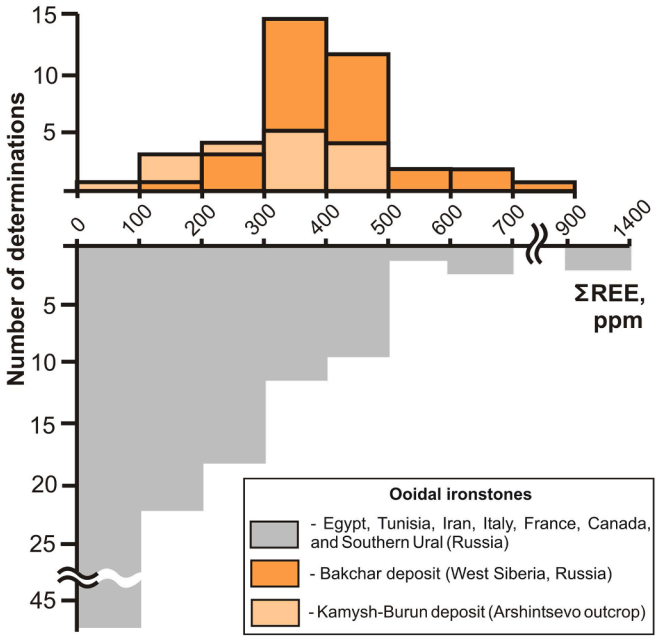

Fig. 1. ΣREE contents in ooidal ironstones of the Kamysh-Burun deposit (Kerch Peninsula) compared to those from the Bakchar deposit (West Siberia) and from other Phanerozoic ooidal ironstone deposits worldwide. Ooidal ironstones of Egypt (Salama et al., 2012; Baioumy et al., 2014, 2017; Afify et al., 2018), Tunisia (Garnit and Bouhlel, 2017), Iran (Rahiminejad and Zand-Moghadam, 2018), Italy (Franceschelli et al., 2000), France (Gloaguen et al., 2007), Canada (Kafle, 2011) and Southern Urals, Russia (Novoselov et al., 2018) (mean value = 183 ppm; number of analyses = 148). Ooidal ironstones of Bakchar deposit (West Siberia, Russia) (mean value = 416; number of analyses = 36) (Rudmin et al., 2019). Ooidal ironstones of Kamysh-Burun deposit (Arshintsevo outcrop) (mean value = 257 ppm; number of analyses = 21).

The REE prices rose by a factor of ten after the supply crisis of 2010, and the price spike of 2011 triggered a worldwide scramble to discover new sources of REE + Y (Hatch, 2012; Seredin and Dai, 2012; Emsbo et al., 2015; Dai et al., 2018; Zhao et al., 2019) and quickened the interest to the contents and speciation of REE + Y in unconventional raw materials, including ooidal ironstone (Afify et al., 2018; Baioumy et al., 2014, 2017; Garnit and Bouhlel, 2017; Rudmin et al., 2019, 2020a,b). The available estimates of REE + Y contents in ooidal ironstones vary from <100 ppm to >1400 ppm, being 183 ppm ΣREE on average (Fig. 1). Bulk ore samples from the giant Bakchar ooidal iron deposit in West Siberia contain ~300 ppm ΣREE on average and >750 ppm in some instances (Rudmin et al., 2019, 2020a, 2020b), which is commensurate with the respective amount in the Chinese industrial ion-adsorbed clay deposits that range from 500 to 2000 ppm of total REEs (ΣREE), with 50–200 ppm ΣHREE (Wu et al., 1996; Bao and Zhao, 2008; Hatch, 2012; Kynicky et al., 2012; Wall, 2014). Like other recently discovered unconventional REE sources, these ironstones are challenging with regards to REE extraction because they reside within a diverse array of fine-grained minerals that are difficult to physically concentrate.

Marine or less often alluvial ooidal ironstones occur broadly in Phanerozoic rocks worldwide (Table S1) and store about 300 billion metric tons of Fe (an average Fe_2O_3 content of 38–48 wt%) or about 14% of total global iron (Zitzmann, 1978). Historically the prime impetus for the study of the REE + Y distribution in Fe-(Mn)-(oxy)hydroxide marine sediments, including ooidal ironstones, has been the investigation of their depositional conditions and the behavior of REE + Y during sedimentation and diagenetic alteration (Ohta and Kawabe, 2000, 2001; Dubinin, 2004; Bau and Koschinsky, 2009; Kim et al., 2012; Surya Prakash et al., 2012; Bau et al., 2014; Baioumy et al., 2014, 2017; Bekker et al., 2014; Afify et al., 2015, 2018; Chen et al., 2015; Garnit and Bouhlel, 2017; Yang et al., 2017; Novoselov et al., 2018). The viability of REE resources is heavily dependent on the cost of beneficiation and chemical REE extraction (Hatch, 2012; Emsbo et al., 2015). The highest potential is expected from the ironstones in which ΣREE is coupled with P, where the latter is leachable biologically (Wang et al., 2010). Therefore, REE + Y can be obtained as a byproduct from high-phosphorus iron ores, which makes ooidal ironstones more attractive commercially (Rudmin et al., 2020a,b).

Judging by high positive correlation between ΣREE and P contents, phosphates are considered as important REE + Y carriers in ooidal ironstones (Novoselov et al., 2018; Rudmin et al., 2019, 2020; Sturesson, 2003; Yang et al., 2017). The ores most often contain minerals of the apatite group, which are mainly sedimentary cryptocrystalline or amorphous carbonate-fluorapatite (Golubovskaya, 2003; Taylor and Konhauser, 2011), as well as clastic fluorapatite and Cl-enriched apatite inherited from the provenance metamorphic and igneous rocks. For example, apatite of this kind is the main REE host in the Aswan ooidal ironstone (Baioumy et al., 2017; Garnit and Bouhlel, 2017). Authigenic LREE phosphates with $CePO_4$ stoichiometry were recently revealed as common accessories in the Bakchar and Sinara-Techa ooidal ironstones (Novoselov et al., 2018; Rudmin et al., 2019, 2020). However, long before these discoveries, relatively abundant early-diagenetic LREE phosphate minerals had been characterized as important REE carriers in shallow-marine sandstones (Rasmussen, 1996; Rasmussen et al., 1998) and in banded iron formations (Smith et al., 2008). The Kerch iron ores are rich in Fe and Ca-Fe phosphates (Chukanov, 2005), but nothing has been known about their REE + Y signatures, and no REE phosphate

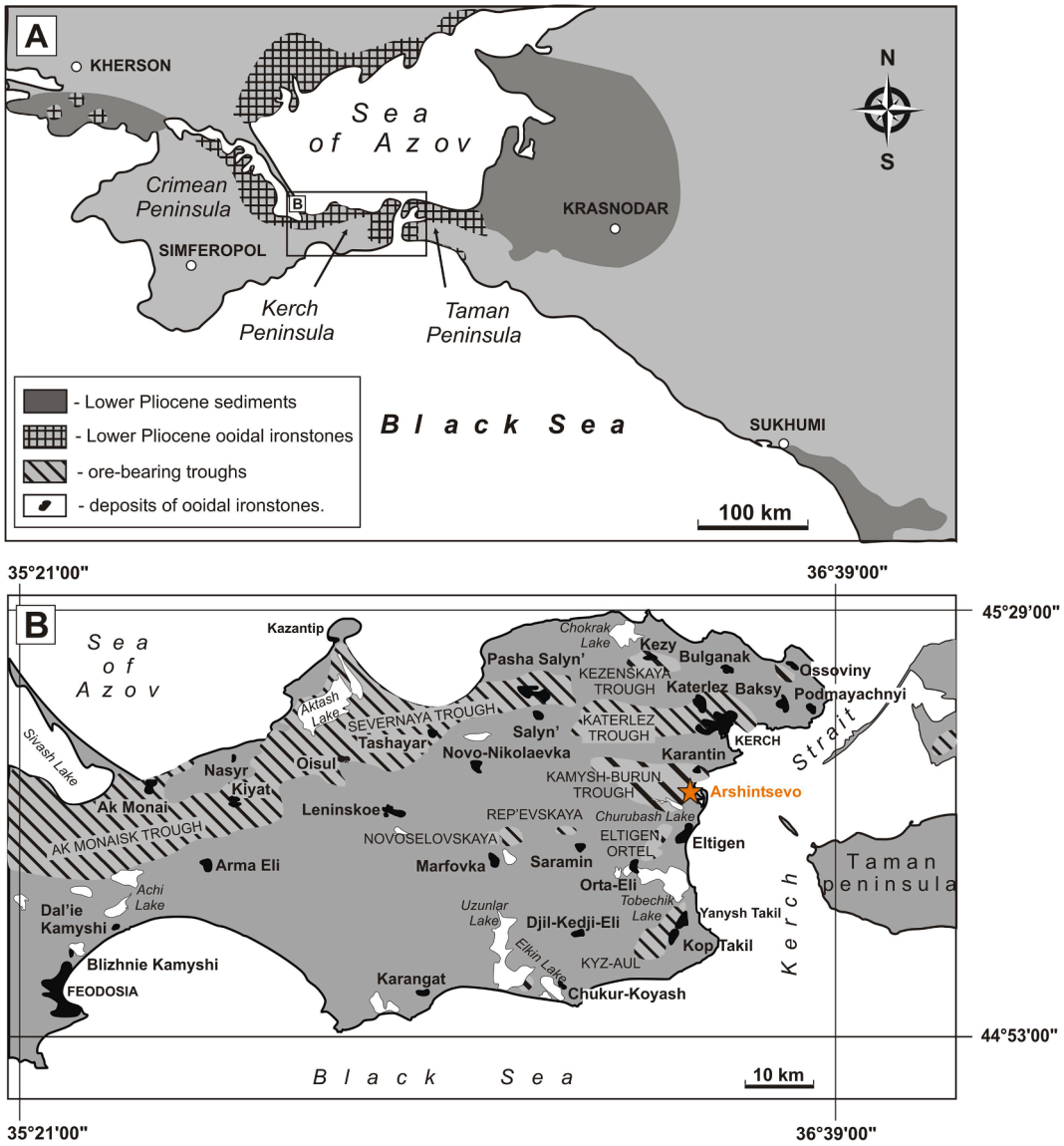

Fig. 2. Early Pliocene ooidal ironstones in the Azov-Black Sea province. (A) Sketch map of Early Pliocene ores of the Azov-Black Sea iron provinces, after (Shnyukov, 1965). (B) Distribution of ooidal ironstone deposits in the Kerch Peninsula, modified after (Chukanov, 2005).

minerals have ever been reported.

In this contribution, we discuss the REE + Y signatures and their distribution in bulk samples and different constituents of ooidal ironstones from the Kamysh-Burun deposit in the Kerch Peninsula (Black Sea-Azov iron province), with implications for the depositional environments. Another issue concerns Fe^{3+}-(oxy)hydroxides, Fe-Mn carbonates, LREE- and Fe^{2+}-bearing phosphate minerals as REE and Y carriers. Their individual signatures and contributions to the bulk REE + Y budget of the Kerch ironstones have been revealed and constrained for the first time.

2. Kerch ooidal ironstone

2.1. General background

The Early Pliocene Azov–Black Sea iron province (Zanclean stage, 5.2–3.6 Ma, or Cimmerian Formation in the Russian terminology) includes iron fields in the Kerch and Taman Peninsulas and over other large areas in Russia, Ukraine, and Georgia. The contours of the province almost coincide with those of the Cimmerian shallow paleo-sea (Shnyukov, 1965; Nedumov, 1994; Shnyukov et al., 2005; Golubovskaya, 2001; Popov et al., 2004, 2010; Kholodov et al., 2014) (Fig. 2). The total area of onshore ore deposits exceeds 7500 km^2, while the resources reach 1.2–2.7 billion tons (Lugovskaya et al., 2015).

Since the Early Cenozoic, the province has evolved as a foreland basin after the continental collision of Arabia and Eurasia. The Azov, Black, and Caspian seas are the currently shrinking remnants of the Tethyan ocean that closed in the Early Miocene, about 20 Ma ago. After that time, all geological structures in the North Black Sea region (including the Kerch Peninsula) were controlled by the Caucasian orogeny (Zonenshain and Le Pichon, 1986; Philip et al., 1989; Mosar et al., 2010). The Greater Caucasus structure has affected significantly the lithology of sediments and the extent of deposition in the Indol-Kuban and Terek-Caspian foredeeps. The mineral deposits are small and contain no more than 30% iron in the eastern part of the province (Krasnodar region and Georgia) where rapid deposition has been maintained by voluminous clastic inputs from the Caucasus Range. In contrast, chemogenic deposition of ooidal ironstones with an average Fe_2O_3 content of 54–64% occurred in shallow brackish lagoons of the present Kerch Peninsula, away from the Caucasus Mountains (Shnyukov, 1965; Nedumov, 1994; Golubovskaya, 2001; Kholodov et al., 2014).

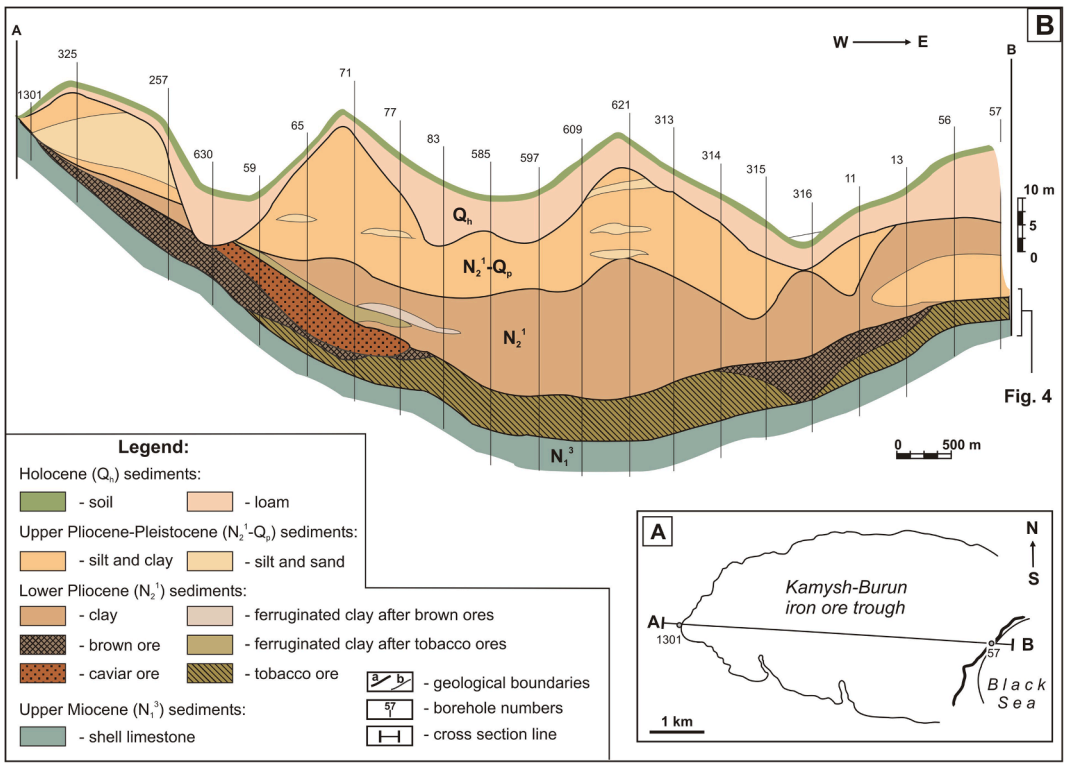

Fig. 3. Geology of the Kamysh-Burun trough, modified after (Malakhovsky, 1956). (A) Sketch map of the Kamush-Burun trough. (B) Geological cross section along profile A–B, Kamysh-Burun trough. The corresponding stages in the Russian stratigraphy: Kuyalnik (N_2^1-Q_p), Cimmerian (N_2^1), and Pontian (N_1^3).

In Late Miocene (Tortonian-Messinian stages, 7.6–6.1 Ma), horizontal compression of the Kerch–Taman sedimentary basin produced an echelon of W–E folds, totaling over thirty-five large structures (Fig. 2B) (Chukanov, 2005; Shnyukov et al., 2005; Kokh et al., 2015; Sokol et al., 2018, 2019). In Zanclean time (5.2–3.6 Ma), some of the syndepositional brachysyncline structures acted as particular traps for ooidal ironstones (Malakhovsky, 1956; Shnyukov, 1965; Arbuzov et al., 1967; Kholodov et al., 2014). The ore-bearing basins are grouped into two ~500 km long W–E belts in the northern coast of the Kerch Peninsula and in the southern Taman shore. Main commercial deposits of Kamysh-Burun and Eltigen-Ortel are located in a 30–40 km N–S zone along the eastern shore of the Kerch Peninsula between these belts (Fig. 2B).

2.2. Types of the Kerch ironstones

The ooidal ironstones known as Kerch iron ores were deposited in lagoon-like brackish estuaries (limans) by several processes: coagulation of Fe colloids at the chemical barrier of fresh/saline water, sedimentation, and redistribution and accumulation of allochems near the shore in a setting of abnormally high biological productivity (Shnyukov, 1965; Arbuzov et al., 1967; Golubovskaya, 1999, 2001; Chukanov, 2005; Kholodov et al., 2014). All Kerch ooidal ironstone deposits share similar stratigraphy, with ore beds sandwiched between Miocene – Lower Pliocene (6.1–5.2 Ma) shell limestones below and Upper Pliocene – Pleistocene (3.6–1.9 Ma) sandy and clayey sediments above. Within the largest Kamysh-Burun and Eltigen-Ortel deposits, the ore beds are quasi-horizontal (dip angles of 1–3° or less often 5–7°) (Fig. 3). The earliest reports (Malakhovsky, 1956; Shnyukov, 1965) distinguished three types of commercial Kerch ooidal ores (tobacco, brown and caviar-like). Siderite and rhodochrosite ores are of low quality and have no practical value. Later on, this classification also acquired genetic significance.

The tobacco ores lying at the base of the ore strata are mainly composed of Fe-rich trioctahedral smectite (ferrosaponite). Ores of this type were considered as colloidal sediments deposited in shallow brackish bays and lagoons (Shnyukov, 1965; Golubovskaya, 2001; Chukanov, 2005; Kholodov et al., 2014). The brown ores are predominant at the trough margins and result from oxidation of tobacco ores exposed to aeration. During oxidation, Fe^{2+}-rich trioctahedral smectite converts to an aggregate of partially amorphous Fe^{3+}-bearing dioctahedral smectite and Fe^{3+}-(oxy)hydroxide (Tsipursky and Golubovskaya, 1989; Chukanov, 2005). The brown ores commonly bear abundant Fe phosphates, siderite or rhodochrosite layers and nodules, and baryte concretions. The caviar-like ores occur at the top of ore bed sets only in the northeastern terminations of five troughs in the Kerch Peninsula. In the Kamysh-Burin deposit, they are 1.5–6 m thick and have prominent cross stratification indicating deposition in a high-energy setting (Fig. 3). They were considered as beach facies deposited in sand bars under the water or in surge zones (Shnyukov, 1965; Golubovskaya, 1997, 2001; Kholodov et al., 2014).

The Kerch iron ores bear abundant fossils, including gigantic forms of brackish fauna, as well as pseudomorphs after terrestrial plants. They also contain diverse phosphatic minerals: anapaite ($Ca_2Fe^{2+}(PO_4)_2{\cdot}4H_2O$), vivianite ($Fe^{2+}{}_3(PO_4)_2{\cdot}8H_2O$), metavivianite ($Fe^{2+}{}_{3-x}Fe^{3+}{}_x(PO_4)_2(OH)_x{\cdot}(8-x)H_2O$), santabarbaraite ($Fe^{3+}{}_3(PO_4)_2(OH)_3{\cdot}5H_2O$), messelite ($Ca_2(Fe^{2+},Mg)(PO_4)_2{\cdot}2H_2O$), and fairfieldite ($Ca_2Mn^{2+}(PO_4)_2{\cdot}2H_2O$) (Chukanov, 2005).

2.3. Site description

Kamysh-Burun is a large trough in the eastern Kerch Peninsula located about 5–8 km south of Kerch city (Fig. 2). The trough is slightly elongated in the W–E direction and is mainly filled with Pliocene sediments. The Zanclean ooidal ironstone sequence occupies an area of 28 km^2 and varies in thickness from 0.5 to 15 m (Fig. 3). The ore strata in the northeastern Kamysh-Burun deposit include tobacco ore at the base of the section, brown ore in the middle, and caviar-like ore at the top. The ironstone beds lie over ~45–50 m thick shell limestone and sandy

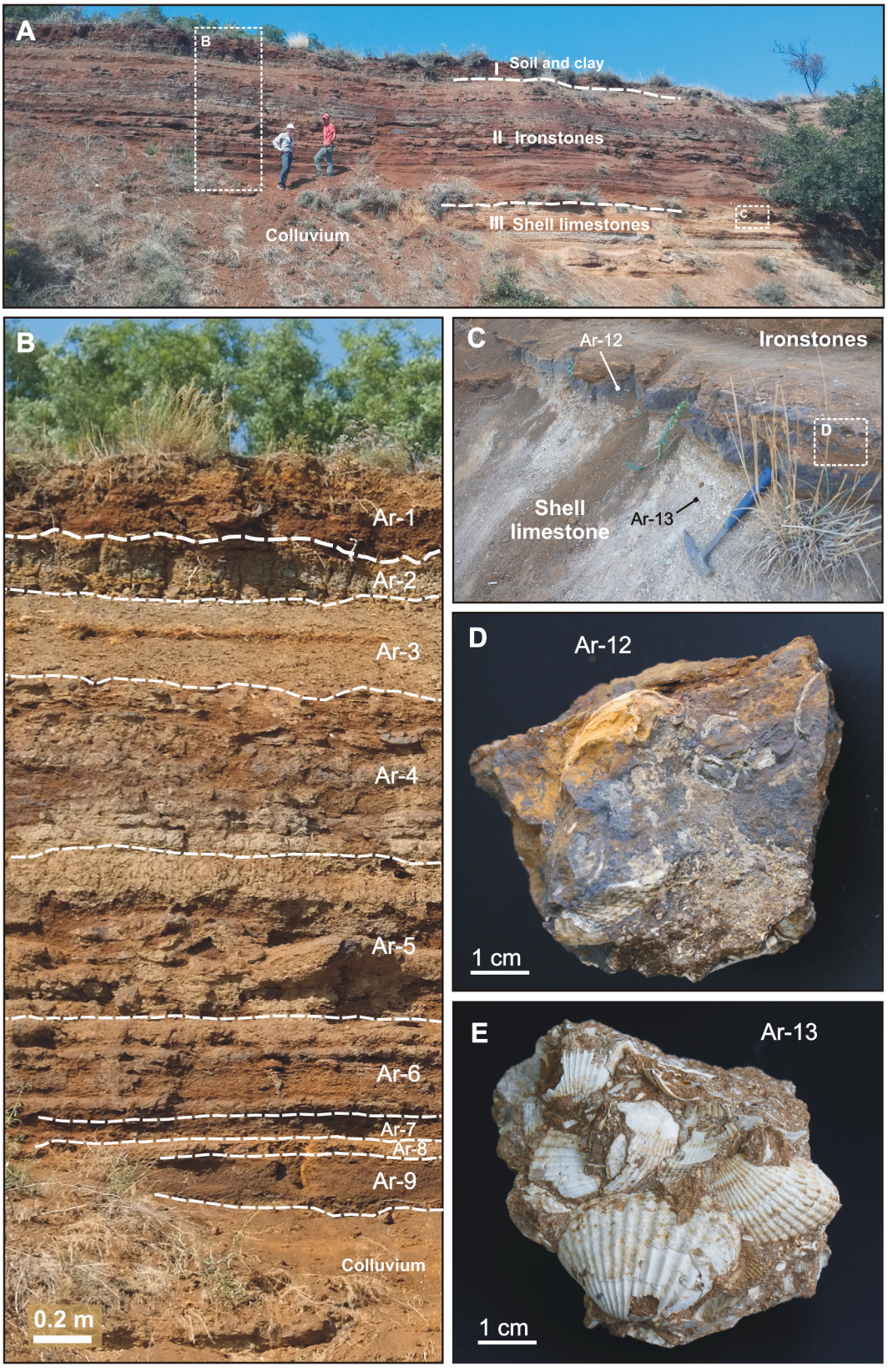

Fig. 4. Outcrop of ooidal ironstones along a nearly vertical cliff of the Kerch strait (Arshintsevo, Kamysh-Burun deposit). (A, B) Field panoramic view. Ooidal ironstone sequence with beds of ooidal ironstone and carbonate ores above the basal Upper Miocene-Lower Pliocene shell limestone (N_1^3), with Upper Pliocene-Pleistocene ferruginate clay (N_2^1-Q_p) and Holocene soil (Q_h) on the top. (C, D) Massive ore with scarce ferruginous allochems at the base of the ore sequence. The basal bed contains numerous shell fragments, rare mineralized mammal bones, as well as gypsum, barite, and alunite. (E) Shell limestone impregnated with Fe^{3+}-(oxy)hydroxides. Ar-1–Ar-9 = numbers of ironstone beds; Ar-12 = number of basal bed; Ar-13 = number of shell limestone bed.

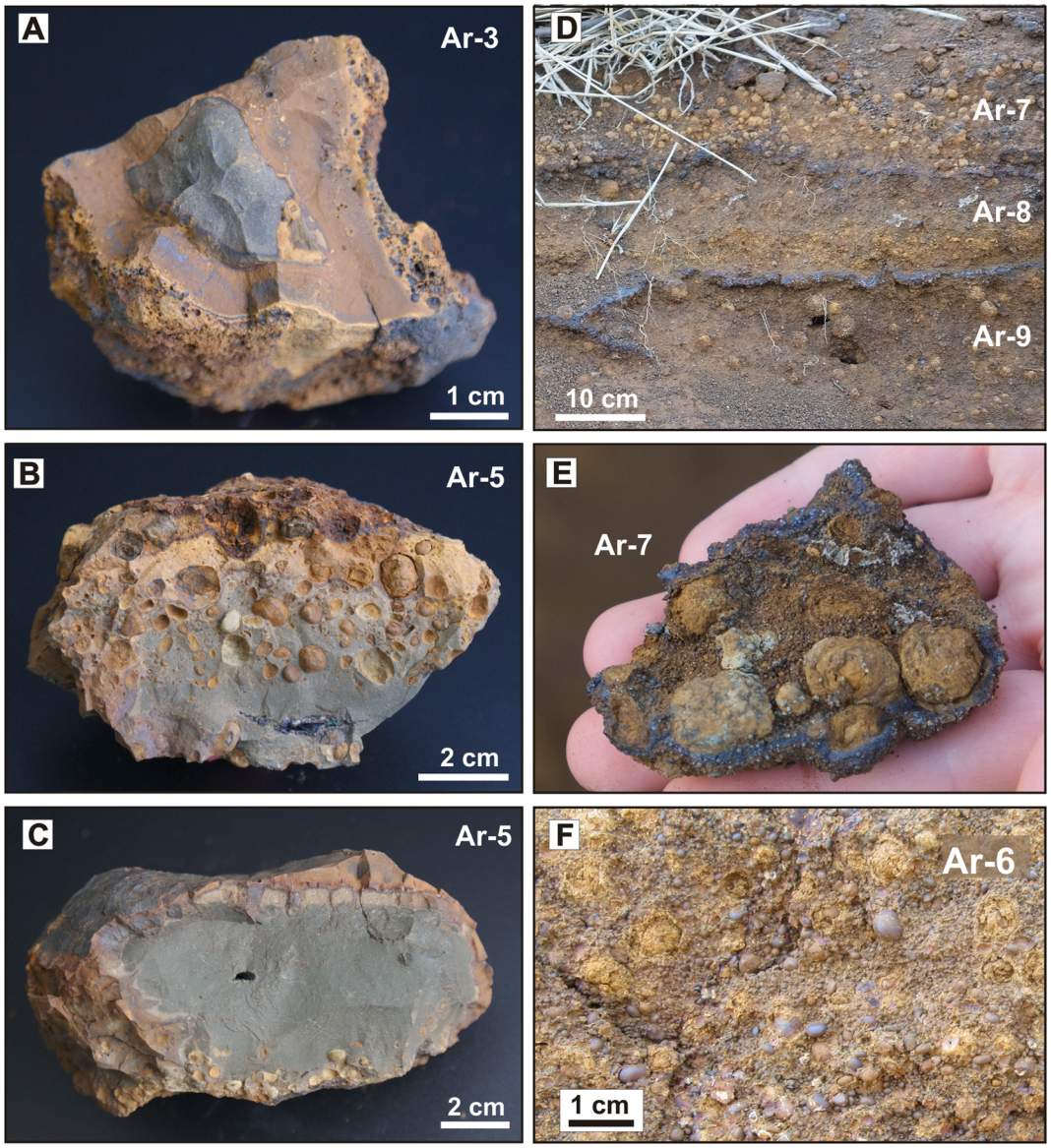

Fig. 5. Carbonate (A–C) and ooidal (D–F) ironstones, Arshintsevo outcrop. (A–C) Structure of carbonate ironstone concretions and nodules. The massive greenish cores of concretions are composed of Fe-rich or Mn-rich carbonates and contain rare ferruginous allochems. Carbonate cores are rimmed by brown oxidized crusts mainly composed of Fe^{3+}-(oxy)hydroxides. (D) Unconsolidated or weakly cemented ooidal ironstones in the lower part of the ore sequence, with 80–95 vol% of ooids, pisoids and peloids. (E) Coarse-grained ooidal ironstones with abundant gypsum. (F) Weakly cemented medium-grained ooidal ironstone. Ar-1, Ar-3, Ar-5 – Ar-9 = numbers of ironstone beds.

clay and are overlain by ferruginated clay, marl and soil (from 1 to 2 to 12 m) (Malakhovsky, 1956; Shnyukov, 1965; Golubovskaya, 2001; Chukanov, 2005).

We focus on a representative ooidal ironstone sequence of the Kamysh-Burun deposit extending N–S for more than 2 km along a huge vertical cliff of the Kerch strait near the Arshintsevo community (Fig. 4). The foot-wall shell limestone impregnated with Fe^{3+}-(oxy)hydroxides (Fig. 4A, C and E) lies at a 1–3° angular unconformity under a ~4 m thick horizontal sequence of ooidal ironstone. The sequence of typical brown ores starts with a ≤0.2 m basal bed of massive ore composed of Fe^{3+}-(oxy)hydroxides with scarce peloids and ooids (Fig. 4C and D). The bed encloses numerous shell fragments (mainly aragonitic), rare mineralized mammal bones (apatite group minerals), gypsum, bassanite ($CaSO_4 \cdot 0.5H_2O$), baryte and alunite ($KAl_3(SO_4)_2(OH)_6$). The ore strata consist of seven ooidal ironstone beds composed mainly of goethite and X-ray amorphous Fe^{3+}-(oxy)hydroxides and four beds of siderite and/or rhodochrosite ores, and is capped by clay and soil.

Ooidal ironstones (type 1) form a set of 0.1–0.5 m beds at the base or in the middle of the sequence. They are reddish, and brown to black medium- to coarse-grained unconsolidated or weakly cemented rocks, with 80–95 vol% ooids and peloids (up to 2.5 cm in diameter), 5–20% cement, and trace amounts of detrital matter (mainly quartz), gypsum, and minor halite (Fig. 5). Fe-rich layered silicates and products of their oxidation mainly occur in cement, but some layers are cement-free.

Carbonate iron ores (type 2) occur mainly as 0.1 m beds in the upper part of the sequence or as broken intercalations, lenses, and concretions in ooidal ores (Fig. 5). The rocks are massive, fine-grained, pale green to greenish-brown. The central parts of the beds and the cores of lenses and concretions are composed of Fe- or Mn-carbonates with 5–20% of ooids and peloids. The cores are rimmed by oxidized crusts with abundant Fe^{3+}- and Mn-(oxy)hydroxides, which are commonly enriched in baryte. The ores may also contain mollusk shells composed of aragonite or more rarely of siderite or rhodochrosite.

In the upper part of the Arshintsevo outcrop, there are sporadic

1–0.5 cm wide anapaite veins almost parallel to the lamination of ore beds. Intergrowths of vivianite crystals (commonly inside fossil shells) regularly occur in the basal bed and sporadically appear in carbonate layers up the section (Fig. 6).

3. Materials and methods

The ooidal ironstones of the Kamysh-Burun deposit were examined during a field trip in September 2017. The field work focused on a detailed description and sampling of the ore sequence exposed near the Arshintsevo Village. We collected about 150 samples of ooidal ironstone, Mn- and Fe-rich fresh and oxidized carbonate iron ores, foot-wall shell limestone, ferruginated clay, as well as fossils, vivianite, and anapaite and selected about 100 representative samples for further petrographical, mineralogical, and geochemical analyses. Three bulk samples of cement-free ooidal ironstones were sieved, and nine size fractions were separated: ≤0.07 mm (A); 0.07–0.1 mm (B); 0.1–0.25 mm (C); 0.25–0.5 mm (D); 0.5–1 mm (E); 1–3 mm (F); 3–5 mm (G); 5–10 mm (H); and >10 mm (I). The samples were not put through any mechanical treatment (crushing or milling) prior to sieving.

The analytical work was carried out mainly at the Analytical Center for Multi-Elemental and Isotope Research (Sobolev Institute of Geology and Mineralogy (IGM), Novosibirsk, Russia) and at the Institute of Mineralogy (Miass, Russia). Ironstone samples were prepared as polished thin sections for petrographic study under transmitted polarizing and reflected light using an *Olympus BX51* optical microscope. Scanning electron microscopy (SEM) was applied to determine the texture and morphology of mineral grains and aggregates. The chemistry of minerals and amorphous phases was analyzed by scanning electron microscopy (SEM) from energy-dispersive spectra (EDS), back-scattered electron (BSE) images, and elemental maps (EDS system) in carbon-coated samples. The measurements were performed on a Tescan *MIRA 3MLU* scanning electron microscope (Brno, Czech Republic) equipped with an INCA Energy 450 XMax 80 microanalysis system (Oxford Instruments, High Wycombe, UK), at IGM (Novosibirsk). The operation conditions were: an accelerating voltage of 20 kV and a beam current of 1 nA in low-vacuum (40–60 Pa) or high-vacuum modes, at a count time of 20 s.

X-ray diffraction analysis (XRD) was applied to bulk ore samples and separate fractions. The measurements were performed on a *Shimadzu XRD-6000* diffractometer ($CuK_{\alpha 1+2}$ radiation with graphite monochromator), at 4° to 70° 2θ, at a step of 0.02°, at the Institute of Mineralogy (Miass). The percentages of minerals relative to the total

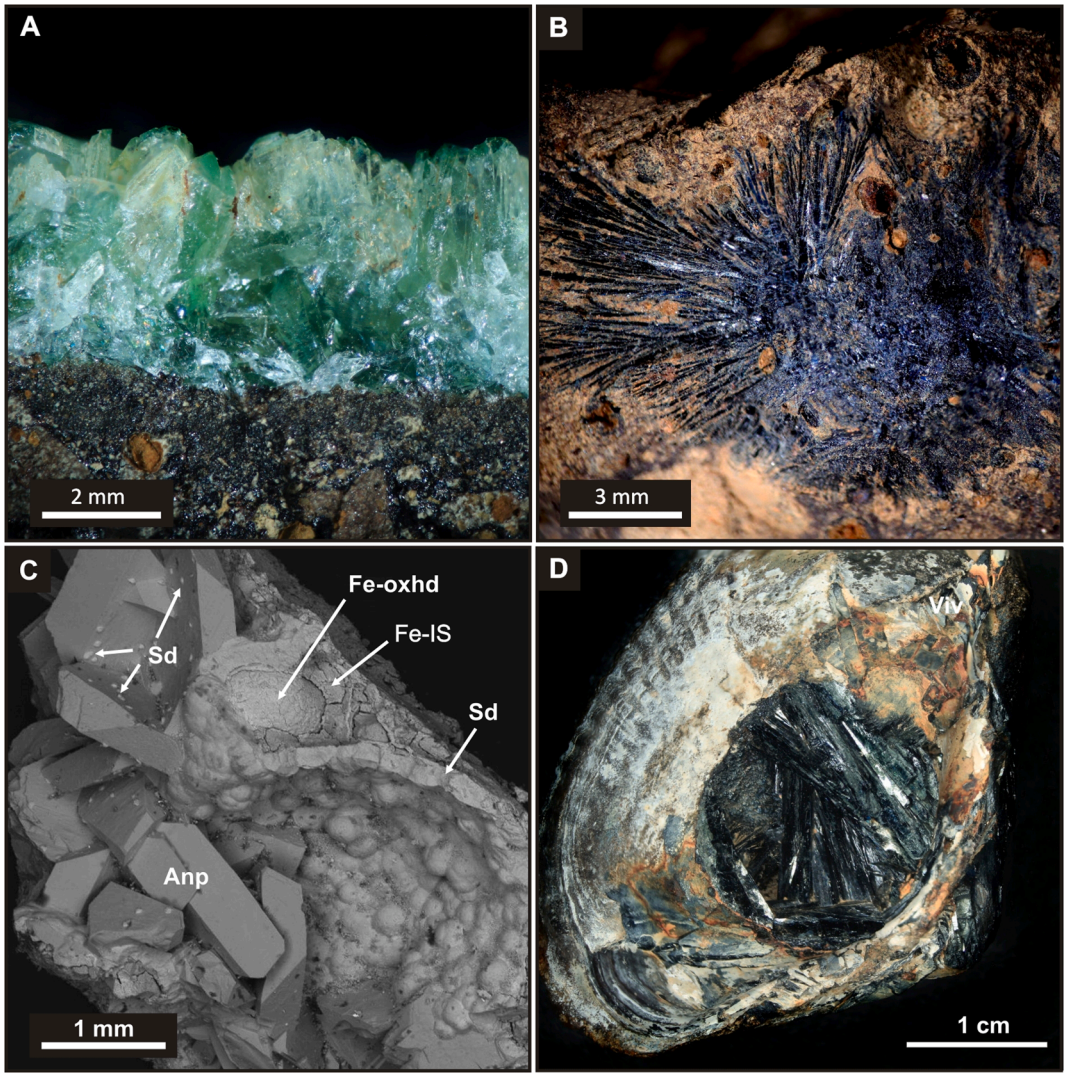

Fig. 6. Fe^{2+}-bearing phosphates and associated minerals in ooidal ironstones, Arshintsevo outcrop. (A) A druse of green anapaite crystals growing in voids of thin cracks that cut the ooidal ironstones. (B) Fan-shaped radiating aggregate of indigo-blue needle-like transparent vivianite in ooidal ironstones. (C) Intergrowths of small perfect anapaite crystals encrusted with numerous later fine siderites, upon a siderite crust with Fe^{3+}-(oxy)hydroxide ooids and patches of Fe-rich IS. BSE image. (D) Radial aggregate of bottle-green vivianite in a fossilized mollusk shell. Anp = anapaite; Fe-IS = Fe-rich smectite-dominated mixed-layer illite–smectite; Fe-oxhd = Fe^{3+}-(oxi)hydroxide; Sd = siderite.

Table 1
Representative analyses of Fe-Mn-Ca carbonates from carbonate ironstone concretions, Arshintsevo outcrop. EDS data, wt%.

Sample	Position	MnO wt%	FeO	CaO	MgO	CO_2	Total	$MnCO_3$ mol%	$FeCO_3$	$CaCO_3$	$MgCO_3$
Rhodochrosite											
Ar-5-5	matrix	30.51	19.75	9.11	<0.3	–	59.37	0.50	0.32	0.19	0.00
Ar-5-11	matrix	33.05	21.00	6.02	<0.3	–	60.07	0.53	0.34	0.12	0.00
Ar-5-12	matrix	34.16	19.15	6.28	<0.3	–	59.59	0.55	0.31	0.13	0.00
Ar-5-12	matrix	37.85	17.24	5.23	<0.3	–	60.32	0.61	0.28	0.11	0.00
Ar-3-1	matrix	39.95	13.62	6.14	0.32	–	60.03	0.65	0.22	0.13	0.01
Ar-3-1	matrix	42.12	10.15	6.95	0.38	–	59.60	0.68	0.16	0.14	0.01
Ar-3-1 †	matrix	46.51	5.34	8.00	0.32	–	60.17	0.74	0.08	0.16	0.01
Ar-3-1	matrix	47.21	5.31	7.21	<0.3	–	59.73	0.77	0.09	0.15	0.00
Ar-3-1 †	crystal	49.75	<0.3	9.22	<0.3	–	58.97	0.81	0.00	0.19	0.00
Ar-3-1	matrix	50.81	<0.3	8.23	<0.3	–	59.04	0.83	0.00	0.17	0.00
(1)		61.71	–	–	–	38.29	100.00	1.00	0.00	0.00	0.00
Mn-rich siderite											
Ar-5-12	matrix	14.93	38.48	6.06	<0.3	–	59.47	0.25	0.63	0.13	0.00
Ar-5-12 ††	matrix	16.46	37.06	5.58	<0.3	–	59.10	0.27	0.61	0.12	0.00
Ar-5-12	matrix	19.15	34.16	6.28	<0.3	–	59.59	0.31	0.55	0.13	0.00
Ar-5-11	matrix	21.00	33.05	6.02	<0.3	–	60.07	0.34	0.53	0.12	0.00
Ar-5-11	matrix	21.58	32.07	5.71	<0.3	–	59.36	0.36	0.52	0.12	0.00
Ar-5-12	matrix	22.56	29.22	7.25	<0.3	–	59.03	0.37	0.48	0.15	0.00
Ar-5-12	matrix	23.26	29.69	5.79	0.58	–	59.32	0.38	0.48	0.12	0.02
Ar-5-12	matrix	24.38	28.12	6.74	0.38	–	59.62	0.40	0.45	0.14	0.01
Ar-5-12	matrix	24.64	27.88	7.39	<0.3	–	59.91	0.40	0.45	0.15	0.00
Ar-5-11	matrix	25.00	26.35	7.70	0.36	–	59.41	0.41	0.42	0.16	0.01
Siderite											
Ar-5-12 ††	crystal	1.39	55.87	3.88	<0.3	–	61.14	0.02	0.90	0.08	0.00
Ar-5-23	matrix	4.27	52.06	4.74	0.46	–	61.53	0.07	0.82	0.10	0.01
Ar-5-23	matrix	4.96	50.55	4.56	0.48	–	60.55	0.08	0.81	0.09	0.01
Ar-5-12	matrix	6.88	47.33	5.25	0.66	–	60.12	0.11	0.76	0.11	0.02
Ar-5-5	matrix	8.06	48.10	3.64	<0.3	–	59.80	0.13	0.79	0.08	0.00
Ar-5-23	matrix	9.23	45.28	5.55	<0.3	–	60.06	0.15	0.73	0.12	0.00
Ar-5-5	matrix	10.33	45.07	4.00	<0.3	–	59.40	0.17	0.74	0.08	0.00
Ar-5-5	matrix	11.17	43.11	4.86	<0.3	–	59.14	0.19	0.71	0.10	0.00
Ar-5-11	matrix	13.88	40.13	5.00	<0.3	–	59.01	0.23	0.66	0.11	0.00
Ar-5-11	matrix	14.33	39.16	6.24	<0.3	–	59.73	0.24	0.64	0.13	0.00
(2)		–	62.01	–	–	37.99	100.00	0.00	1.00	0.00	0.00

(1) = theoretical composition of rhodochrosite $Mn(CO_3)$; (2) = theoretical composition of siderite $Fe(CO_3)$. "†" and " ††" = crystal-marix pairs.

amount of crystalline phases were calculated in SIROQUANT V.4.

Major elements in bulk samples and separate size fractions were analyzed by the solution ICP-OES technique on a ThermoJarrell Intertechs *IRIS Advantage* atomic emission spectrometer (US) at IGM (Novosibirsk). The preconditioning procedure included fusion of powdered whole rock samples with lithium borate following Shatsky et al. (2006). The concentration of Fe(II) was determined by wet chemistry (Jeffery, 1970).

Trace elements in bulk samples of ironstones and separate fractions were determined by mass spectrometry with inductively coupled plasma (ICP-MS) on an Agilent Technologies *7700x* spectrometer (USA) at the Institute of Mineralogy (Miass, Russia). The sediments (50 mg) were digested in a mixture of 2 ml 69% HNO_3, 6 ml 30% HCl, and 2 ml of 40% HF in closed *Teflon* bombs using a Berghof *SpeedWave* microwave digestion system. The procedure was run in steps, programmed to a temperature of 180 °C and a ramp time of 5 min at step 1 and 180 °C, 5 min hold time, a constant power of 500 W and a pressure of 20 bar at step 2. Then the residue was re-dissolved in 5 ml HCl (1:1 V/V) and evaporated. Finally, the residue was dissolved in 10 ml of HNO_3 (20%; 1:5 V/V) and the solution was heated at 150 °C for 30 min. After cooling at room temperature, the solution was poured into 100 ml volumetric flasks and then filled with ultrapure water until the final designed volume for analysis. The quality control and quality assurance procedures included processing and analysis, at each batch, of two blanks and the BCR-2 certified reference material (NIST, USA). Minor and trace elements were quantified using 5-point daily calibration. The analyses were run in triplicate, and the results differed for <5%. Two blanks were prepared and included ten samples in each batch. The procedural blanks accounted for <1% of element concentrations. Precision and accuracy were estimated to be 10–15 rel% for all elements. The detection limits for trace elements were in the range 0.01–0.5 μg/l. The analytical reproducibility was monitored using the BCR-2 standard, in which the measured values were consistent with the certified ones, with extraction efficiencies ranging from 93% to 120%. The method was slightly modified after those reported in USEPA (2007) and Carvalho et al. (2018). Raw REE + Y concentrations were normalized to the Post-Archean Australian Shale (PAAS) (Taylor and McLennan, 1985). As all bulk Kerch ooidal ironstones are mainly composed of goethite, the geochemical data were interpreted using approaches designed for reconstructing the depositional conditions of Fe(Mn)-rich marine sediments (Surya Prakash et al., 2012; Bau et al., 2014; Yang et al., 2017).

The trace element composition of Fe^{2+}-bearing phosphate minerals (vivianite and anapaite) was determined by the laser ablation-inductively coupled plasma-mass spectrometry (LA-ICPMS) at the Institute of Mineralogy (Miass). The LA-ICPMS analysis was applied to selected high-quality crystals of vivianite and anapaite free from signatures of alteration and inclusions. The analysis was run on a *NewWave Research UP-213* laser ablation system coupled with an Agilent 7700x (Santa Clara, CA, USA) plasma mass spectrometer. The procedure was as in (Artemyev and Ankushev, 2019), with an Nd: YAG UV source, frequency quadrupled (wavelength 213 nm) with fluence settings of 4.0–5.5 J/cm^2, helium cell carrier gas and a flow rate of 0.6–0.7 L/min. The mass spectrometer settings were as follows: RF Power–1550 W; Ar as a carrier gas; a flow rate of 0.95–1.05 L/min; a plasma gas flow (Ar) of 15 L/min; and an auxiliary gas flow (Ar) of 0.9 L/min. Each analysis was performed with a laser spot size of 80–100 μm at a frequency of 5 Hz. Each sample was measured for 90 s (30 s measurement of the background plus 60 s analysis), with 5 s pre-ablation before each analysis and

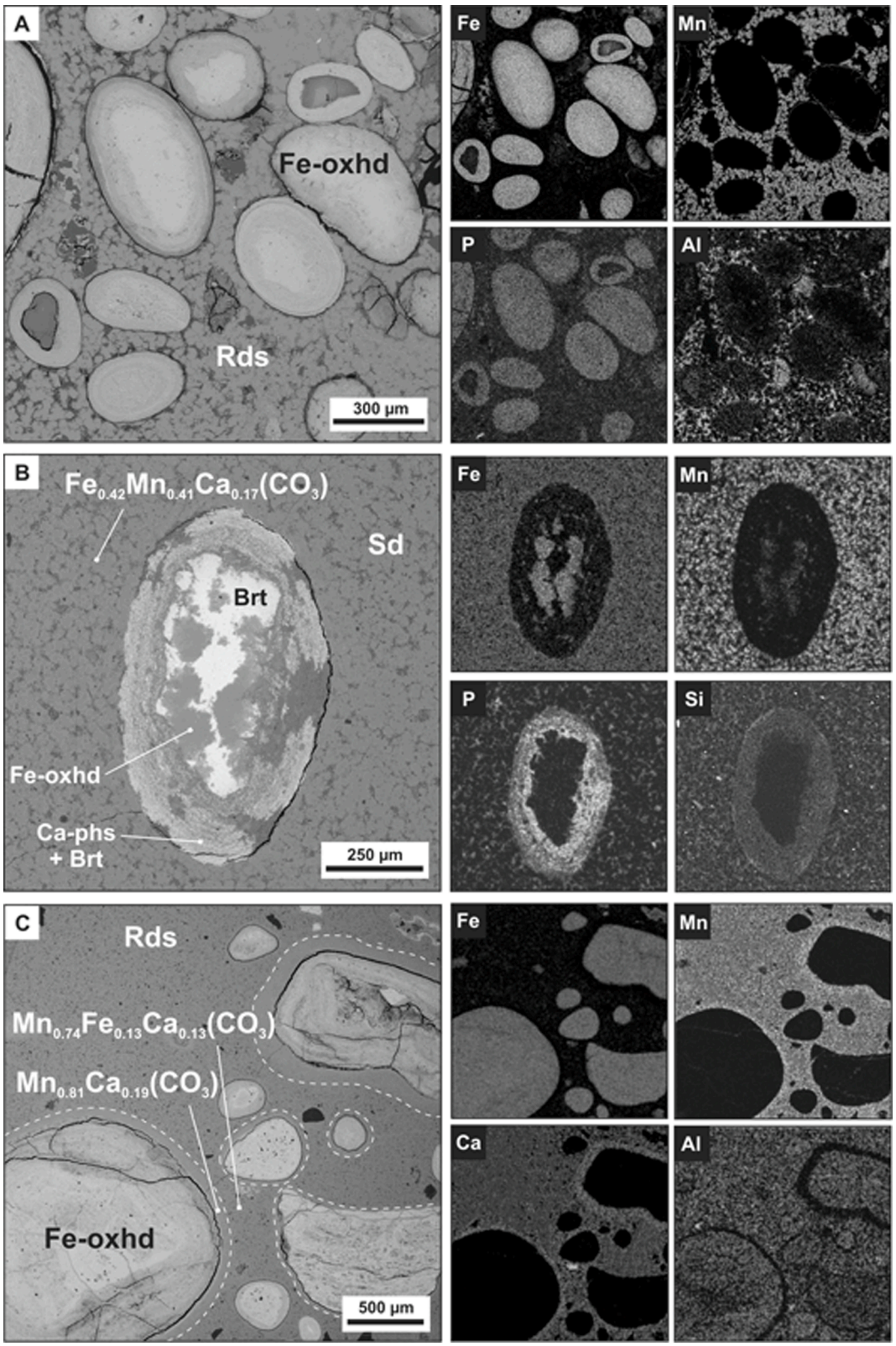

Fig. 7. BSE images (A,B,C) and elemental maps (Fe, Mn, P, Al, Si, Ca) of Fe^{3+}-(oxi)hydroxide allochems and carbonate matrix (carbonate ironstone concretions, Arshintsevo outcrop). (A) Fe^{3+}-(oxi)hydroxide ooids in a rhodochrosite matrix. The pore space between rhodochrosite grains with festooned contours is filled with Fe-rich IS phase. (B) An ooid in a siderite matrix. An ooid nucleus composed of Fe^{3+}-(oxi)hydroxides and baryte and a laminated cortex composed of baryte and Ca-phosphate. (C) Micrite matrix, composed of Fe-bearing rhodochrosite ($Mn_{0.74}Fe_{0.13}Ca_{0.13}(CO_3)$) and larger Fe-poor rhodochrosite grains ($Mn_{0.81}Ca_{0.19}(CO_3)$ rimming ferruginous allochems. Brt = baryte; Ca-phs = Ca phosphate; Fe-oxhd = Fe^{3+}-(oxi)hydroxides; Rds = rhodochrosite; Sd = siderite.

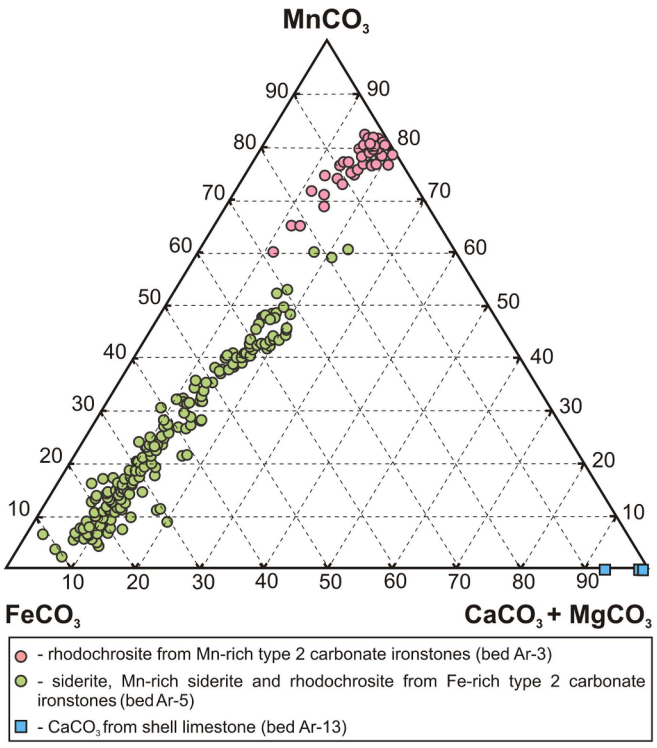

Fig. 8. $FeCO_3$–$MnCO_3$–($CaCO_3$ + $MgCO_3$) ternary diagram showing the composition of Fe-Mn-Ca carbonates from concretions and nodules, Arshintsevo outcrop.

30 s washout between the analyses. Production of molecular oxide species (i.e., $^{232}Th^{16}O/^{232}Th$) and doubly charged ion species (i.e., $^{140}Ce^{++}/^{140}Ce^{+}$) was maintained at <0.2%. The element contents were calibrated against reference materials of NIST SRM-612 and USGS GSD-1g using ^{43}Ca and ^{57}Fe as internal standards for anapaite and vivianite. The major-element composition of every anapaite and vivianite grain (including Ca, Fe, Mg, Mn, P contents) was determined in advance by electron microprobe analysis (EMPA).

All mass fractions for NIST SRM-612 and USGS GSD-1g were taken from the GeoReM base preferred values. The calibration standard was analyzed every 10–15 spots to account for the instrument drift. Data were processed using the *Iolite* software package (Paton et al., 2011).

4. Results

4.1. Mineralogy and petrography

4.1.1. General characteristics

Type 1 ironstones have oolitic textures and comprise 80–95% of ooids, peloids and pisoids. Hereafter allochems in the Kerch ironstones are typified using the classification of Young (1989). They vary in morphology (spheroidal, from perfectly round to ellipsoidal, or less often irregular) and texture, all being composed mainly of microcrystalline goethite (α-FeO(OH)) with minor amounts of other FeO(OH) modifications and amorphous Fe^{3+}-(oxy)hydroxides. Ooids and pisoids commonly have a concentrically laminated cortex but lack any clear nucleus, except for a few specimens with a clayey nucleus (Fig. 5D-F and 7). The allochems are cut with concentric or radial cracks.

The bulk samples of type 1 ironstones contain predominant goethite (75–95% relative to the total amount of crystalline phases); about 5% of a Fe-rich smectite-dominated illite–smectite (IS) phase (ferrosaponite), and minor gypsum (~2%), Fe-Mn carbonates (up to 3%); ≤1% quartz, halite, and baryte. The percentage of X-ray amorphous Fe^{3+}-(oxy)hydroxides ranges from 20% to 60%. The coarse fractions of 1–10 mm ooids and pisoids are mostly composed of goethite (~85–95%) and bear within 5% of the IS phase and up to 8% of Fe-Mn carbonates. The fine fractions (≤0.25 mm) contain no more than 70% of goethite, ~15–25% Fe-rich IS, 3–8% baryte, up to 5% detrital quartz, ~4% gypsum, and 1–3% kaolinite.

Type 2 carbonate ironstones are mainly composed of siderite or rhodochrosite with sporadic allochems buried in a carbonate matrix (Table 1; Figs. 5A–C; 7; 8). Carbonates form micritic aggregates of 5–10–50–70 μm subhedral to anhedral grains with festooned outlines (Fig. 7A-C). The interstices are filled with a Fe-rich IS phase and are sometimes enriched in phosphate matter. Most of the SEM element maps show homogeneous phosphorus distribution in allochems (Fig. 7A), with few exceptions of P-rich rims (Fig. 7B).

The bulk samples of Mn-rich type 2 ironstones are mainly composed of rhodochrosite (Table 1; Fig. 8) and bear no more than 7% siderite, while the Fe–rich varieties contain 23–31% siderite and 3–19% rhodochrosite. Goethite in the bulk type 2 ironstones ranges from 17 to 56% depending mainly on the alteration degree of primary Fe-Mn carbonates. The fresh cores of concretions almost fully (≥90%) consist of Fe-Mn carbonates, while the oxidized crusts around them are composed of 40–80% goethite (Fig. 5A-C). Minor phases are Fe-rich IS (3–8%), quartz (1–4%), gypsum (1–2%), and baryte (up to 3–8%). No authigenic Ca-rich carbonates were found.

Fe-Mn carbonates make up an almost continuous series from siderite to rhodochrosite: $(Mn_{0.02\text{-}0.83}Fe_{0.0\text{-}0.90}Ca_{0.06\text{-}0.22}Mg_{0.0\text{-}0.03})(CO_3)$ (Table 1; Fig. 8). Rhodochrosite and Mn-rich siderite commonly contain more CaO ($Xav = 7.79$ wt%, N = 143) than Mn-poor siderite ($Xav = 4.53$ wt%, N = 217), while magnesium is present only as an impurity ($Xav =$ 0.13 wt% MgO, N = 371). The impure micrite carbonate occurs in matrix, whereas larger pure carbonate grains either fill voids or grow over allochems. Their compositions approach siderite $Fe_{0.90}Mn_{0.02\text{-}}Ca_{0.08}(CO_3)$ (matrix $Fe_{0.61}Mn_{0.27}Ca_{0.12}(CO_3)$) or rhodochrosite $Mn_{0.81}Ca_{0.19}(CO_3)$ (matrix $Mn_{0.74}Ca_{0.16}Fe_{0.08}Mg_{0.01}(CO_3)$) end members (Table 1; Fig. 7C and 8).

Both ironstone types from the Kamysh-Burun deposit are depleted in detrital material (quartz and almost no feldspar) and in accessories (ilmenite, rutile, kyanite, sillimanite, zircon, and monazite). Besides common baryte, we only found few segregations of authigenic partly oxidized pyrite, tiny grains of galena, anglesite ($Pb(SO_4)$), ZnS (sphalerite or wurtzite), and orpiment (As_2S_3) (Fig. 9).

The basal bed has a distinct mineralogy (Fig. 4C and D) with predominant goethite (70–77%), amorphous Fe^{3+}- and Mn-(oxy)hydroxides, and 3–5% of Fe-rich IS. This is the only bed with abundant shell fragments composed of Sr-enriched aragonite (7–14%) and calcite (2–3%). The bed also bears alunite (4–6%), gypsum (1–2%), and strontian baryte (with up to 12.7 wt% SrO).

4.1.2. Fe^{2+}-bearing phosphate minerals

Vivianite ($Fe^{2+}_3(PO_4)_2{\cdot}8H_2O$) occurs sporadically in ooidal ironstones from the lower part of the section, as quite large clusters of dark blue or bottle-green crystal druses inside shells, bright blue to indigo blue biomorphs after mollusks, and radial aggregates up to 2–4 cm in size (Fig. 6). Vivianite commonly forms lamellar, wedge- and needle-shaped transparent crystals (from 0.5 to 7 mm) flattened in the {0 1 0} plane. An average vivianite composition is $Fe_{2.25\text{–}2.89}Mn_{0\text{–}0.48}Mg_{0\text{–}0.40}Ca_{0\text{–}0.16}Na_{0\text{-}0.09}P_{1.98\text{–}2.03}O_8{\cdot}8H_2O$ (Table 2), while other impurities (Sr, Ba, As, V, Co, Cr, Zn) are negligible. Our SEM-EDS and XRD analyses failed to detect disseminated vivianite or other Fe-bearing phosphates in P-rich bulk ores or allochems.

Anapaite ($Ca_2Fe^{2+}(PO_4)_2{\cdot}4H_2O$) was found near the surface of the Arshintsevo outcrop as 0.3–0.5 cm thick encrustation on subparallel cracks in ooidal ironstone (bed Ar-3). The anapaite veins are nearly horizontal and have sharp contacts with the host ironstones, where the matrix of predominant Fe^{3+}-(oxy)hydroxide was converted into tiny segregations of mono-phase needle-like goethite. The veins are filled with closely packed and randomly oriented light-green to bluish-green

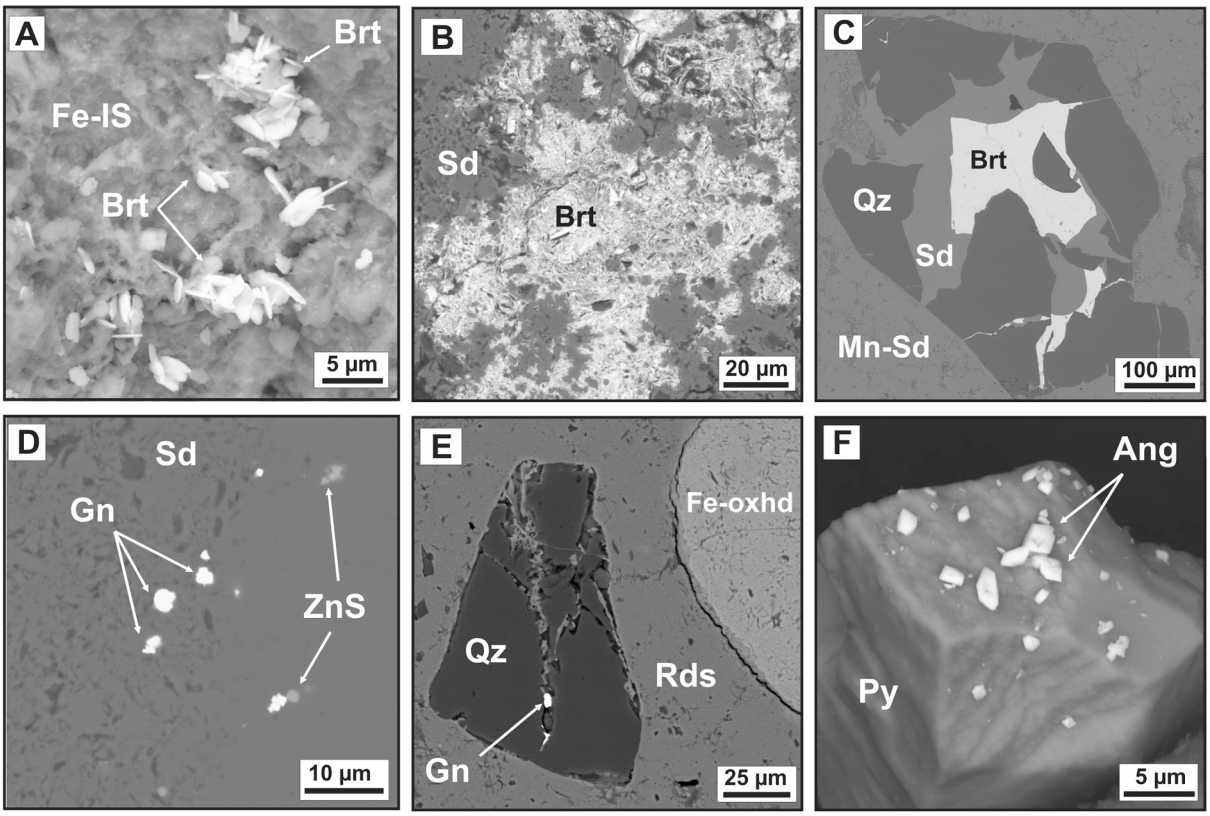

Fig. 9. Accessories from ooidal ironstones, Arshintsevo outcrop. BSE images (A) Baryte encrustation on an illite–smectite matrix. (B) Authigenic baryte patches in a siderite matrix. (C) A cracked grain of detrital quartz in a Mn-rich siderite matrix; cracks are filled with a barite-siderite aggregate. (D) Fine grains of galena and ZnS in a carbonate matrix. (E) A galena grain in a crack that cuts a rounded grain of detrital quartz. (F) Tiny anglesite crystals precipitated on the surface of partly oxidized pyrite. Ang = anglesite; Brt = baryte; Fe-IS = Fe-rich smectite-dominated mixed-layer illite–smectite; Fe-oxhd = Fe^{3+}-(oxi)hydroxides; Gn = galena; Mn-Sd = Mn-rich siderite; Py = pyrite; Qz = quartz; Rds = rhodochrosite; Sd = siderite.

platy split (0.2–2.0 mm) grains in the interior and perfect 0.3 mm to 1 mm anapaite crystals, with euhedral terminations pointing to the vein axis, in the axial part (Fig. 6A). The anapaite composition ($(Ca_{1.93-2.0})(Fe_{0.89-1.01}Mg_{0.02-0.13}Mn_{0.01-0.08})(P_{1.96-2.01}S_{0.0-0.02})O_8{\cdot}4H_2O$) is nearly stoichiometric (Table 2) with low contents of uniformly distributed impurities: 1185 ppm Si, 484 ppm Sr, 151 ppm Na, 8.1 ppm Ba, and 4.8 ppm As (LA-ISPMS data, average values). The anapaite crystals lack any zonation (color, composition, or distribution of inclusions) or regeneration textures, but their surfaces are sporadically encrusted by fine siderites (Fig. 6C). The coexisting phases are subordinate siderite, IS, barite, and very rare pyrite and halite, besides predominant Fe^{3+}-(oxy) hydroxide.

4.1.3. REE phosphate minerals

REE-bearing phosphates are widespread, although minor, accessories in the Kerch ooidal ironstones. They were detected by SEM mainly inside allochems in ooidal ore beds 3–7, and 9–11 and rarely in the oxidized carbonate matrix (beds Ar-3 and Ar-5) (Figs. 10 and 11).

Detrital xenotime (5 μm) occurs in ore beds Ar-3 and Ar-4 (Fig. 10B) as fine grains, with the Y ≫ Gd ≈ Dy > Er ≈ Yb relative contents of cations: $(Y_{0.79}Dy_{0.07}Gd_{0.05}Er_{0.03}Yb_{0.02}Ca_{0.02}Sm_{0.01})PO_4$. Neither diagenetic xenotime nor any other HREE-enriched minerals were found in the Arshintsevo ironstones.

Detrital monazite is present as a few grains (up to 30 μm) and clasts in all beds, including re-crystallizes foot-wall shell limestone. It differs from authigenic LREE phosphates in coarse monolith grains with linear outlines and in a particular chemistry (Table 3): $(Ce_{0.42-0.46}La_{0.21-0.29}Nd_{0.16-0.17}Pr_{0.04-0.05}Ca_{0.00-0.04}Th_{0.02-0.04}Sm_{0.00-0.04}Gd_{0.00-0.02}Dy_{0.00-0.01}U_{0.00-0.01})PO_4$. The relative contents of cations make up the Ce > La ≈ Nd ≫ Pr ≈ Th > Sm > Gd series. All grains contain Th (2.4–4.3 wt% ThO_2) and some also contain up to 0.6 wt% UO_2, while CaO is within 1.06 wt%. The surface of detrital monazites is commonly etched but not encrusted with later authigenic LREE phosphates unlike that reported by Rasmussen (1996). Natural etching in Th-enriched monazite can bring out numerous ≤1 μm wide radiation defects (Fig. 10A). The resorbed detrital monazite sporadically co-occurs with microparticles of galena or anglesite. Pb is a product of radioactive decay of Th and liberates during leaching dissolution of Th-enriched monazite (Berger et al., 2008).

Authigenic LREE phosphates were found in the Kerch ooidal ironstones as a single minute irregular patch of oval or spindle-like particles (up to 3 μm) and their intergrowths or clusters (up to 5–25 μm in size) in allochems (Table 3; Fig. 10). Some SEM BSE images reveal vague alignment of bright LREE phosphate patches along the lamination of allochems. These phosphates commonly fill pores (Fig. 10C-D) or less often appear as abundant 'rash' on the walls of micro-fissures in allochems (Table 3; Fig. 10F and G). No authigenic LREE phosphates have been found in fresh carbonates; they rather occur as impregnation in P-enriched oxidized crusts after siderite.

The pore-filling particles of authigenic LREE phosphates are commonly too small for precise analysis of mineral chemistry which thus can only be presented in atomic ratios of ΣLREE:P≈1:1, as typically in $CePO_4$. They differ from detrital monazite in the absence of Th and enrichment in Ca, with Ce > La ≈ Nd ≈ Ca > Pr > Sm. Judging by the low oxide totals (Table 3) and excess O relative to the $CePO_4$ stoichiometry, authigenic LREE phosphates are hydrated phases. Ca-bearing LREE phosphates with the lowest deficit of totals and ~31–32 wt% oxygen content can be distinguished as rhabdophane $(Ce(PO_4){\cdot}(0.7–1)H_2O)$, according to the criteria of Krenn and Finger (2007). Due to partial metamictization, these phases commonly contain additional

Table 2
Average compositions of anapaite and vivianite from ooidal ironstones. WDS-EDS data, wt%.

	Xav	σ	min	max	Ideal
Anapaite, N = 12					
CaO	27.86	0.13	27.57	28.07	28.18
FeO	17.65	0.29	17.34	18.13	18.05
MgO	0.34	0.19	<0.02	0.65	–
MnO	0.10	0.18	<0.02	0.41	–
P_2O_5	35.53	0.67	34.51	36.40	35.66
SO_3	0.07	0.16	<0.03	0.43	–
H_2O	na	na	na	na	18.11
Total	81.90	–	–	–	100.00
8 oxygens, apfu					
Ca	1.97	–	–	–	2.00
Fe	0.99	–	–	–	1.00
Mg	0.04	–	–	–	–
Mn	0.02	–	–	–	–
P	1.98	–	–	–	2.00
S	0.01	–	–	–	–
H_2O	–	–	–	–	4.00
Vivianite, N = 5					
FeO	39.29	1.35	36.91	40.29	42.97
MgO	1.27	0.71	0.65	2.49	–
MnO	0.17	0.24	<0.02	0.50	–
CaO	0.42	0.58	<0.01	1.12	–
P_2O_5	28.26	0.09	28.12	28.37	28.30
H_2O	na	na	na	na	28.73
Total	69.48	–	–	–	100.00
8 oxygens, apfu					
Fe	2.78	–	–	–	3.00
Mg	0.16	–	–	–	–
Ca	0.04	–	–	–	–
Mn	0.01	–	–	–	–
P	2.00	–	–	–	2.00
H_2O	–	–	–	–	8.00

Ideal = theoretical compositions of anapaite $Ca_2Fe(PO_4)_2{\cdot}4H_2O$ and vivianite $Fe_3(PO_4)_2{\cdot}8H_2O$, respectively;
N = number of analyses; *Xav* = mean value; σ = standard deviation; min = minimum value; max = maximum value; apfu = atoms per formula unit; na = not analyzed.

H_2O, as it was earlier revealed by Berger et al. (2008). Their Ca enrichment might be explained (Berger et al., 2008) by restricted solid solutions or submicrometric $Ce(PO_4){\cdot}nH_2O$ and brockite ($(Ca,Ce,Th)(PO_4){\cdot}H_2O$) intergrowths.

It was possible to characterize the chemistry of authigenic LREE phosphates from clots and intergrowths of spindle-like particles inside allochems (the Ar-9 bed) (Table 3, Fig. 10F and G). The compositions of authigenic LREE phosphates dominated by LREEs (Σ = 17–24 wt% R_2O_3), P_2O_5 (15.3–19.5 wt%), CaO (6.3–8.5 wt%), and SO_3 (2.5–4.8 wt %) are also typical of rhabdophane group minerals. Following Berger et al. (2014), we infer that this phase may be a limited solid solution of a rhabdophane-like compound ($LREE(PO_4){\cdot}nH_2O$) and tristramite ($(Ca,U,Fe^{3+})((PO_4),(SO_4)){\cdot}2H_2O$) or their ultrafine intergrowths. The persistence of Fe in analyses would appear to support the existence of solid solutions or intergrowths with Fe^{3+}-bearing tristramite, but the EDS Fe_2O_3 content (19.6–31.7 wt%) is too high for tristramite (usually <8 wt %). Combined SE and BSE images and element mapping revealed that the clots of authigenic LREE phosphates were coated by Fe^{3+}-(oxy)hydroxide films. The LREE phosphate layers and Fe^{3+}-(oxy)hydroxide films locally produce a thin lamination (Table 3).

4.2. Major- and trace-element chemistry of the Kerch ironstones

4.2.1. Chemistry of bulk rocks, coarse and fine fractions

Major- and trace- element compositions were studied in samples of bulk ooidal and carbonate ironstones, sieved size fractions of ooidal ironstones, basal bed Ar-12, and shell limestone (Tables 4–9; Fig. 11). Iron is a main component in both ore types, but the FeO/Fe_2O_3 ratios are different: Fe_2O_3 ranges from 50.03 to 66.19 wt% at ≤1.61 wt% FeO in ooidal ironstones, while fresh carbonate ores have ~34 wt% FeO and no more than 14.70 wt% Fe_2O_3 depending on the amount of allochems (Table 8). The MnO contents reach ~24 wt% in rhodochrosite ores, but do not exceed ~4.5 wt% in ooidal ones (Fig. 11).

The Kerch ores have high phosphorus enrichment, which is 2.73 wt% P_2O_5 in average in carbonate ironstones and 2.53 wt% in the ooidal samples. Phosphorus (P_2O_5) and iron (Fe_2O_3) in ooidal ironstones show significant positive correlation with $r = 0.75$. (N = 9). The contents of CaO are likewise higher in the carbonate ores (up to 8.23 wt%), but no P *vs* Ca correlation was observed. Both ironstone types have low Al_2O_3 contents (2.90–5.00 wt%) and different ranges of SiO_2: 8.91–11.45 wt% in carbonate ores and 7.85–23.64 wt% in the ooidal ones, mainly due to contamination by detrital quartz with altered Fe-rich IS. Both ore types are depleted in TiO_2, Na_2O, and K_2O (Table 4; Fig. 11).

In carbonate ironstones, Si, Al, and P reside in tiny inclusions of clayey and phosphate matter in interstices between Fe-Mn carbonate grains (Fig. 7). Consequently, the micritic carbonate matrix contains P_2O_5 (*Xav* = 1.19), Al_2O_3 (*Xav* = 0.97), and SiO_2 (*Xav* = 1.19), whereas recrystallized coarse carbonate grains have compositions close to siderite or rhodochrosite (Table 1).

Basal bed Ar-12 stands out in lower contents of Fe_2O_3 (≤49.09 wt%) and P_2O_5 (≤0.92 wt%) but higher MnO (5.72–6.99 wt%); greater Ca and Sr enrichments (7.51–12.89 wt% CaO and 115–328 ppm Sr) due to the abundance of shell detritus (calcite + aragonite), as well as Ba enrichment (666–7065 ppm) associated with baryte-celestite impregnation (Figs. 9 and 11). The shell limestone has the greatest CaO content (30.67 wt%) but bears only 23.21 wt% Fe_2O_3 due to secondary impregnation by Fe^{3+}-hydroxides, and is depleted in all trace elements except Sr (Tables 4 and 5; Fig. 11).

The Kerch ores show contrasting enrichments in Mn (*Xav* = 0.95 wt% against *Xav* = 0.11 wt%), V (*Xav* = 180 ppm against *Xav* = 150 ppm), As (*Xav* = 180 ppm against *Xav* = 10.6 ppm), and Ba (*Xav* = 1981 ppm against *Xav* = 650 ppm) relative to the respective PAAS values (Tables 5, 7, and 9; Fig. 11). Bulk ooidal ironstones are enriched in V and As relative to the carbonate ironstones ($X^V av$ = 250 ppm against $X^V av$ = 157 ppm and $X^{As} av$ = 662 ppm against $X^{As} av$ = 360 ppm). Both ironstone types are depleted in U (0.63–1.61 ppm), Th (2.27–8.93 ppm), and Zr (15.3–42.3 ppm) relative to PAAS.

The coarse fractions (E-I) mainly include 1–10 mm allochems, and thus have their phase, major- and trace-element compositions very similar to that of the bulk goethite-dominated ooidal ironstones. The fine fractions are depleted in Fe_2O_3 and P_2O_5 but enriched in SiO_2 and Al_2O_3 (Table 6), as well as in Co, Ga, Rb, and Cs (Table 7) due to greater percentages of ultrafine particles of IS-phase, its amorphization products, and detrital quartz. They also store fine-grained detrital accessories (rutile, ilmenite, zircon, monazite, xenotime, etc.) and thus are richer in Ti, Zr, Y, and Th relative to allochems. The [Zr] – [ΣREE] diagram (Fig. 12) shows that the contribution of detrital accessories into the ΣREE + Y budget of the Kerch ores is roughly the same in all bulk samples and coarse fractions (Fig. 12). The fine fractions, however, have high ΣREE enrichment (699–1153 ppm), while the Zr excess is minor (58.5–74.5 ppm) (Fig. 12). The kink of the [Zr] – [ΣREE] trend (Fig. 12) records a change of main REE carriers, which was revealed by SEM analyses as relatively abundant authigenic LREE phosphates (see Section 4.1.3.).

Large variations of P_2O_5 contents in the bulk ooidal ironstones and their size fractions are not accompanied by any systematic change of ΣREE. The respective linear correlation coefficient (*r*) values are insignificant (0.16 and 0.21). The Fe_2O_3 – ΣREE correlations are moderate negative, at $r = -0.67$ (bulk samples and coarse fractions) and $r = -0.52$ (fine fractions) (Fig. 12B,C). Moderate positive correlation exists between Al_2O_3 and ΣREE, with *r* of 0.67 in bulk rocks and coarse fractions and 0.69 in fine fractions (Fig. 12D).

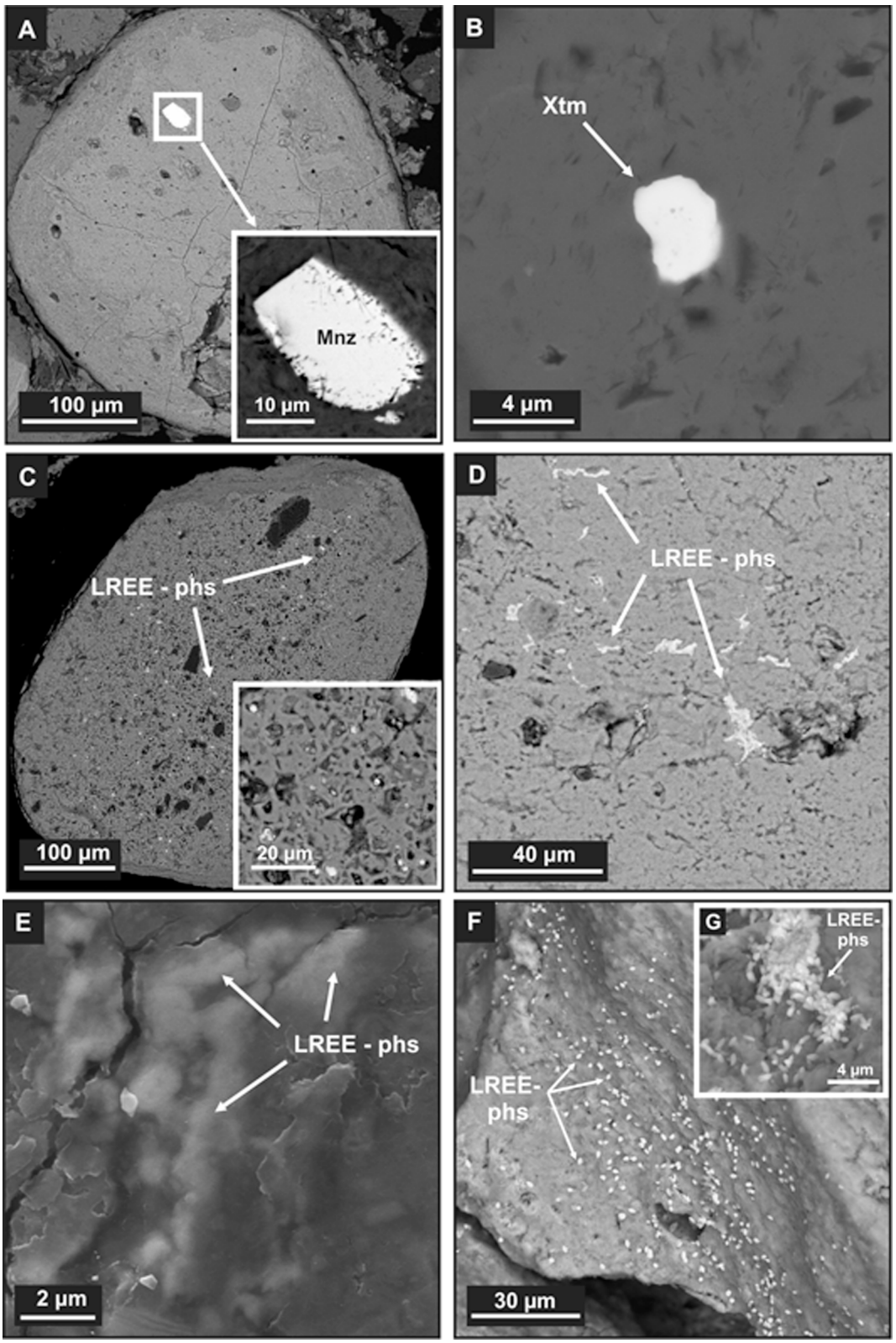

Fig. 10. Morphology of REE- and Y-phosphates from ooidal ironstones, Arshintsevo outcrop. (A) Grain of detrital Th-enriched monazite with numerous radiation defects buried in a Fe^{3+}-(oxi)hydroxide matrix. (B) A fine grain of detrital xenotime in a carbonate matrix. (C) Numerous minute particles of authigenic LREE phosphates (rhabdophane-like phase) filling the pore space in a Fe^{3+}-(oxi)hydroxide peloid. (D, E) Fe^{3+}-(oxi)hydroxide matrix impregnated with authigenic LREE phosphates (rhabdophane-like phase).(F) Abundant 'rash' of authigenic LREE phosphates (rhabdophane – tristramite phase) on the surface of an allochem. (G) A cluster of spindle-like particles of the rhabdophane – tristramite phase. (A-D, F) = BSE images, (E) = SE image. Mnz = monazite; Xtm = xenotime; LREE-phs = authigenic LREE phosphates.

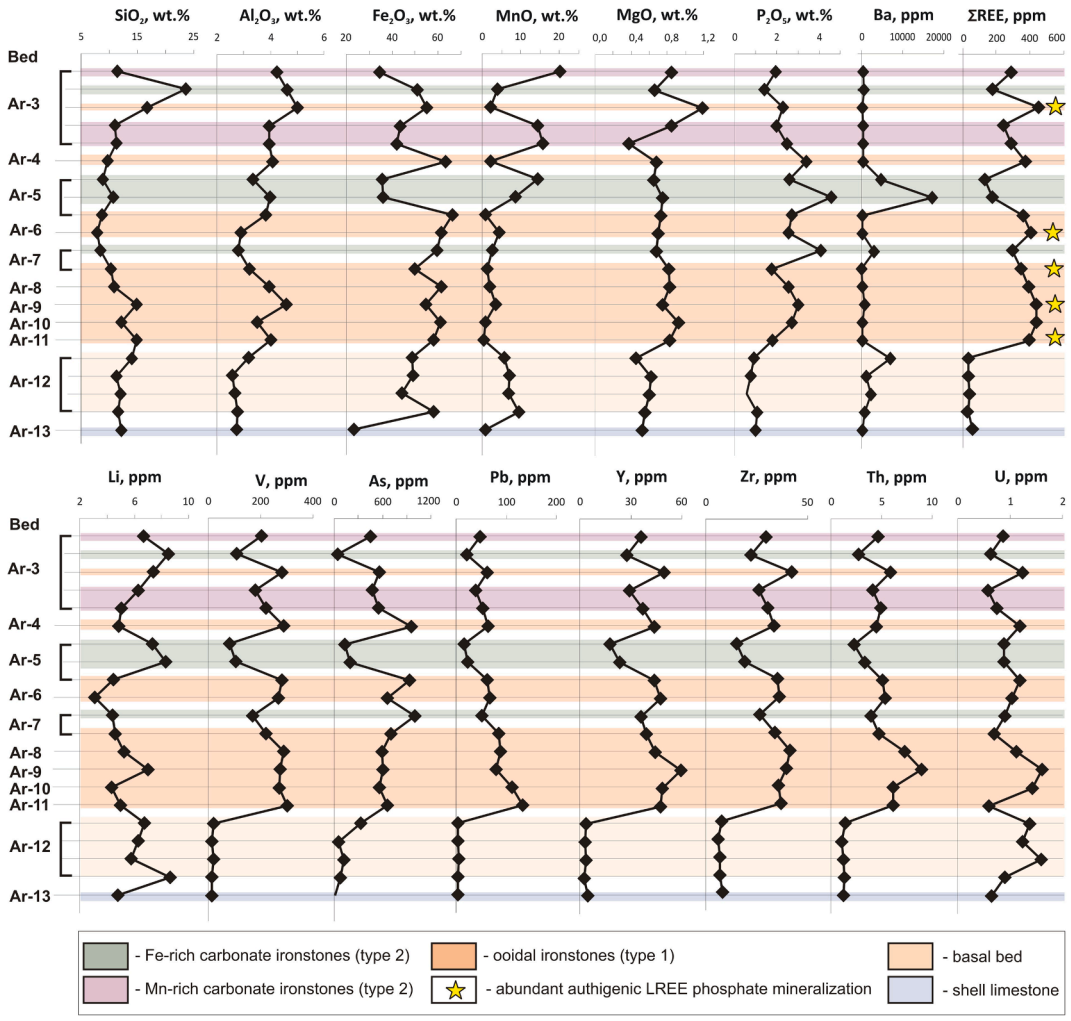

Fig. 11. Major and trace element contents in ooidal and carbonate ironstones of different beds, Arshintsevo outcrop. Element contents are as in Tables 4, 5, 10.

4.2.2. REE + Y geochemistry of the Kerch ironstones, their fractions, and authigenic Fe^{2+} and Ca-Fe^{2+} phosphates

The ΣREE + Y concentrations in ooidal and carbonate ironstones and their constituents as well as in anapaite and vivianite crystals are summarized in Tables 10–13 and Figs. 13 and 14. Both shell limestone and basal bed samples are markedly depleted in ΣREE (*Xav* = 57.6 ppm and 34.6 ppm, respectively) relative to the PAAS value (ΣREE = 183 ppm) (Taylor and McLennan, 1985) (Fig. 13). The ΣREE content in fresh carbonate ironstones is still below that in PAAS (*Xav* = 103 ppm), but it approaches the latter in oxidized crusts after carbonate concretions (*Xav* = 178 ppm). The ΣREE markedly exceeds the PAAS value in bulk ooidal ironstones and in their coarse fractions (*Xav* = 400 ppm and 405 ppm, respectively) but is twice higher (*Xav* = 858 ppm) in fine fractions (Table 10–12).

The PAAS-normalized REE + Y patterns of all ironstones are similar, with moderate MREE enrichment, minor Ce* (0.67–1.09) and moderate Y* (0.57–0.70) negative anomalies, though ΣREE contents vary widely. A prominent positive Eu* anomaly was detected in all carbonate ores, and basal bed samples.

The samples can be more distinctly discriminated according to Gd_N/La_N and Yb_N/La_N ratios (where N denotes PAAS-normalized contents) against the concentrations of ΣREE (Tables 10–12; Fig. 15). The two ratios measure, respectively, MREE and HREE enrichment over LREE. The Gd_N/La_N ratios plotted against ΣREE (Fig. 15A) are comparable (1.9–2.4) in all bulk ooidal ironstones and their size fractions, irrespective of ΣREE contents which vary from 130 to 1153 ppm (insignificant correlation with $r = 0.33$). The shell limestone and basal bed samples are ΣREE-depleted and display only slight MREE enrichment. The carbonate ores show their own correlation trend, where Gd_N/La_N increases from 1.45 to 2.79 with the 34.7–303 ppm ΣREE increase (significant correlation with $r = 0.91$). The HREE enrichment is the lowest in shell limestone ($Yb_N/La_N = 0.43$) and is slightly higher in the basal bed samples (Yb_N/La_N ~0.71 on average) and in bulk carbonate and ooidal ironstones (Yb_N/La_N generally 0.93–1.56) though their ΣREE vary from 130 to 455 ppm. The Yb_N/La_N ratios in fresh carbonate concretions and their oxidized crusts increase with ΣREE (significant correlation with $r = 0.88$) (Fig. 15B).

The ΣREE contents in the size fractions of ooidal ironstones, on the contrary, increase at the account of LREEs and are the greatest (699–1153 ppm) in fine fractions, where the Yb_N/La_N ratios are 0.52–0.83. In coarse fractions, these ratios reach 0.70–1.61, i.e., the samples show both HREE and MREE enrichment (Table 11; Fig. 13A-B and 15).

The PAAS-normalized patterns of LREE phosphates in the Kerch ooidal ironstones (Fig. 13D) highlight the features of REE distribution in authigenic phases compared with those in detrital monazite. Both rhabdophane-tristramite and rhabdophane-like phases are depleted in Gd but enriched in Pr, Nd and Sm (relative to Ce and La), but the enrichment is significant in the former and minor in the latter.

Vivianite and anapaite have ΣREE markedly below that in PAAS, with average contents of 0.93 ppm (0.58–1.73 ppm) in vivianite and 6.95 ppm (1.62–30.0 ppm) in anapaite (Table 13). The PAAS-

Table 3
BSE images and EDS composition (wt%) of authigenic LREE phosphates and detrital monazite from ooidal ironstones, Arshintsevo outcrop.

BSE image

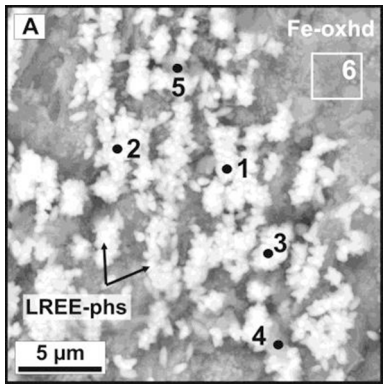

Chemical composition (wt%)

Authigenic LREE phosphate (rhabdophane – tristramite phase)

Point	SiO_2	Al_2O_3	Fe_2O_3	MnO	CaO	Ce_2O_3	La_2O_3	Pr_2O_3	Nd_2O_3	Sm_2O_3	P_2O_5	SO_3	Total
1a	3.06	1.47	22.91	<0.3	7.53	9.92	4.76	1.73	6.01	1.04	19.45	3.92	81.80
2a	2.91	1.66	28.69	<0.3	8.17	9.63	4.59	2.25	5.68	1.68	15.34	3.87	84.47
3a	3.19	1.47	19.62	<0.3	7.96	10.26	5.09	1.85	5.95	1.23	18.77	3.70	79.09
4a	5.61	3.65	44.99	1.30	4.24	4.18	2.43	1.01	3.52	<0.3	10.22	2.52	83.67
5a	7.12	6.10	42.82	1.06	4.83	4.73	2.29	1.01	2.89	<0.3	10.43	2.75	86.03
6a	4.02	3.91	73.41	1.90	1.20	<0.3	<0.3	<0.3	<0.3	<0.3	3.96	<0.3	88.40

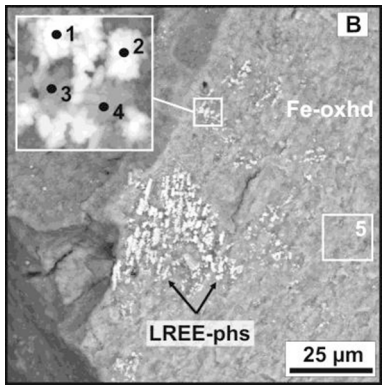

Authigenic LREE phosphate (rhabdophane – tristramite phase)

Point	SiO_2	Al_2O_3	Fe_2O_3	MnO	CaO	Ce_2O_3	La_2O_3	Pr_2O_3	Nd_2O_3	Sm_2O_3	P_2O_5	SO_3	Total
1b	2.76	1.06	22.75	<0.3	6.99	9.21	4.98	1.31	5.25	1.19	16.94	2.72	75.16
2b	1.60	0.91	25.15	<0.3	8.49	9.22	3.85	2.08	5.58	1.46	15.38	4.79	78.51
3b	7.36	4.67	60.32	1.10	1.69	0.69	<0.3	<0.3	0.56	<0.3	4.77	0.62	81.78
4b	10.93	3.23	58.96	1.18	1.80	0.63	<0.3	<0.3	0.56	<0.3	4.56	0.72	82.57
5b	7.10	5.06	69.50	1.83	1.15	<0.3	<0.3	<0.3	<0.3	<0.3	3.60	0.40	88.64

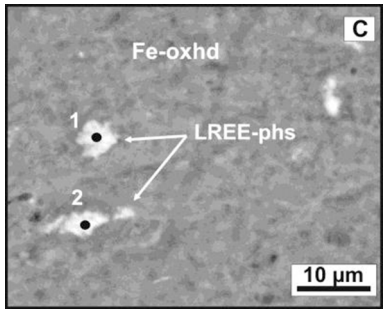

Authigenic LREE phosphate (rhabdophane-like phase)

Point	SiO_2	Al_2O_3	Fe_2O_3	Y_2O_3	CaO	Ce_2O_3	La_2O_3	Pr_2O_3	Nd_2O_3	Sm_2O_3	P_2O_5	SO_3	Total
1c	<0.3	<0.3	19.41	<0.3	8.71	14.18	8.70	1.81	8.22	<0.3	26.23	<0.3	87.26
2c	<0.3	<0.3	18.47	<0.3	8.66	15.65	7.90	1.83	7.79	1.32	27.42	<0.3	89.04

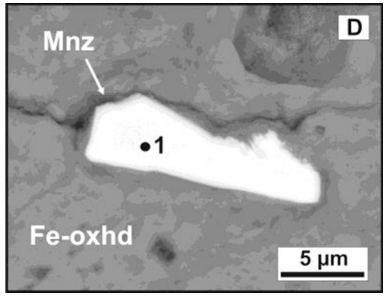

Detrital monazite

Point	La_2O_3	Ce_2O_3	Pr_2O_3	Nd_2O_3	Sm_2O_3	Gd_2O_3	Dy_2O_3	ThO_2	UO_2	CaO	P_2O_5	Total
1d	14.85	29.24	3.44	12.12	2.24	1.28	0.67	4.30	0.58	1.06	29.74	99.52
*	15.30	29.30	3.10	11.90	2.60	1.06	0.65	3.78	0.38	0.90	30.40	99.37
*	14.50	31.40	2.86	12.50	1.97	1.33	0.77	2.56	0.42	0.86	30.82	99.99
*	19.55	31.77	3.57	11.43	<0.3	<0.3	<0.3	2.97	0.30	<0.3	29.86	99.45

Fe-oxhd = Fe^{3+}-(oxy)hydroxides; Mnz = monazite; LREE – phs = authigenic LREE phosphates; 1a-3a, 1b, 2b, 1c, 2c = grains of authigenic LREE phosphates; 4a, 5a, 3b, 4b = grains of authigenic LREE phosphates coated with a thin film of Fe^{3+}-(oxy)hydroxides; 6a, 5b = Fe^{3+}-(oxy)hydroxides, square analysis. * = monazite from other samples.

Table 4
Major-element (in wt%) compositions of bulk ironstone and shell limestone, Arshintsevo outcrop.

Sample	Rock type	SiO_2	Al_2O_3	Fe_2O_3	FeO	MnO	MgO	CaO	Na_2O	K_2O	P_2O_5	SO_3	LOI	Total
Ironstone sequence														
Ar-3-1	c	11.45	4.24	32.06	2.48	20.02	0.85	4.05	0.57	0.32	1.95	0.26	21.05	99.30
Ar-3-2	c	23.64	4.62	51.01	<0.01	4.03	0.66	1.05	0.33	0.50	1.42	<0.03	12.32	99.58
Ar-3-3	o	16.68	5.00	54.97	<0.01	2.15	1.19	1.74	1.04	0.40	2.30	0.14	13.95	99.56
Ar-3-4	c	10.98	3.94	39.60	3.79	14.44	0.85	3.73	0.34	0.34	1.97	0.22	19.11	99.31
Ar-3-4/1	c	11.32	3.94	39.96	1.88	15.82	0.37	4.19	<0.01	0.36	2.47	0.11	19.04	99.46
Ar-4-1	o	9.65	4.07	62.95	0.40	2.11	0.68	1.25	0.60	0.36	3.39	<0.03	14.15	99.61
Ar-5-1	c	8.91	3.34	15.37	20.36	14.33	0.65	6.69	0.44	0.25	2.59	0.66	25.58	99.17
Ar-5-3	c	10.75	3.98	22.96	13.21	8.54	0.75	8.23	0.66	0.36	4.59	1.73	24.32	100.08
Ar-5-4	o	8.65	3.82	66.19	0.12	0.85	0.73	1.40	0.69	0.27	2.71	<0.03	14.17	99.60
Ar-6-1	o	7.85	2.90	59.88	1.61	4.48	0.70	2.47	1.01	0.22	2.55	0.16	16.14	99.97
Ar-7-1	c	8.38	2.80	56.04	3.61	2.63	0.68	4.68	0.70	0.23	4.09	0.37	15.38	99.59
Ar-7-2	o	10.24	3.21	50.03	<0.01	1.28	0.81	7.17	1.08	0.27	1.75	<0.03	24.92	100.76
Ar-8-1	o	10.88	3.96	61.58	<0.01	1.89	0.83	1.92	1.02	0.25	2.54	0.08	15.03	99.98
Ar-9-1	o	14.79	4.59	54.61	<0.01	3.46	0.74	2.92	0.77	0.32	3.01	0.23	14.17	99.61
Ar-10-1	o	12.14	3.51	61.16	<0.01	0.79	0.92	2.16	1.07	0.26	2.72	0.22	14.57	99.52
Ar-11-1	o	14.89	4.01	57.91	<0.01	0.49	0.82	2.70	0.80	0.25	1.80	0.78	14.87	99.32
Basal bed														
Ar-12-3-1	o	13.95	3.17	48.90	<0.01	5.72	0.45	7.51	0.13	0.32	0.92	1.77	16.81	99.65
Ar-12-3-2	o	11.30	2.58	49.08	<0.01	6.99	0.62	10.12	0.16	0.27	0.75	0.54	17.19	99.60
Ar-12-3-3	o	11.95	2.69	44.35	<0.01	6.90	0.60	12.89	0.28	0.25	0.59	0.90	18.00	99.40
Ar-12-8	o	11.54	2.77	58.12	<0.01	9.44	0.55	1.74	0.31	0.33	1.09	0.35	13.74	99.98
Shell limestone														
Ar-13-1	lm	12.11	2.74	23.21	<0.01	0.95	0.52	30.67	0.09	0.36	1.00	0.12	28.02	99.79

Rock type: c = carbonate ironstone, o = ooidal ironstone, lm = shell limestone.

Table 5
Trace-element composition (ppm) of bulk ironstone and shell limestone, Arshintsevo outcrop.

Sample	Rock type	Ti	V	Co	Ni	As	Sr	Zr	Ba	Th	U
Ironstone sequence											
Ar-3-1	c	352	204	46.0	78.7	454	20.5	29.6	316	4.63	0.87
Ar-3-2	c	511	107	53.2	85.4	41.0	56.2	22.0	567	2.74	0.63
Ar-3-3	o	461	280	84.7	129	561	53.8	42.3	157	5.84	1.24
Ar-3-4	c	364	179	32.7	62.4	470	33.5	26.0	376	4.10	0.57
Ar-3-4/1	c	318	219	40.3	75.1	550	31.6	30.5	368	4.87	0.75
Ar-4-1	o	376	287	44.6	77.1	961	46.4	33.6	305	4.50	1.19
Ar-5-1	c	365	80.0	40.6	51.2	129	128	15.3	4674	2.27	0.88
Ar-5-3	c	459	105	41.2	57.1	198	365	19.1	17,254	3.31	0.88
Ar-5-4	o	364	282	46.0	104	938	28.8	35.1	119	5.06	1.18
Ar-6-1	o	265	269	45.6	101	659	56.0	36.2	198	5.33	1.04
Ar-7-1	c	298	170	29.7	56.2	1006	219	26.7	3029	3.99	0.90
Ar-7-2	o	337	220	51.2	84.3	701	69.7	33.9	91.0	4.78	0.69
Ar-8-1	o	381	288	56.6	92.6	594	75.7	41.1	104	7.27	1.12
Ar-9-1	o	448	276	60.6	69.8	602	126	39.6	783	8.93	1.61
Ar-10-1	o	338	272	85.6	110	559	77.2	35.6	95.0	6.13	1.43
Ar-11-1	o	363	300	85.3	80.4	661	47.1	36.9	114	6.13	0.59
Basal bed											
Ar-12-3-1	o	267	18.7	26.7	29.3	330	317	7.94	7065	1.38	1.38
Ar-12-3-2	o	230	13.0	11.7	14.0	58.1	241	6.30	1166	1.08	1.23
Ar-12-3-3	o	206	19.1	12.5	14.5	119	328	7.06	2179	1.23	1.59
Ar-12-8	o	285	13.2	12.8	17.7	71.9	115	7.07	666	1.35	0.89
Shell limestone											
Ar-13-1	lm	258	15.1	7.88	16.3	16.4	310	8.27	261	1.25	0.64

Rock type: c = carbonate ironstone, o = oolidal ironstone, lm = shell limestone.

normalized REE + Y spectra of vivianite show notable LREE depletion (Gd_N/La_N wihtin 15.6–33.9) and HREE enrichment (Yb_N/La_N from 43.4 to 145) but are free from prominent anomalies (Fig. 14). The respective anapaite spectra differ in less pronounced LREE depletion (Gd_N/La_N from 2.44 to 16.2), strong HREE enrichment (Yb_N/La_N from 11.1 to 144), and the presence of moderate negative Ce*, strong positive Y*, and minor positive Eu* anomalies. Thus, the authigenic Fe^{2+}-bearing phosphates have unique REE + Y patterns different from those in any other phase or rock sample we analyzed.

5. Discussion

5.1. REE carriers: Contribution to the total REE budget and individual signatures

The REE distribution in Fe-rich marine sediments and Iron Formations has been widely used as geochemical proxy to provide insights into the ocean water chemistry, as well as into the fractionation of REE and Y during deposition and diagenetic alteration of sediments (Bau et al., 1995; Smith et al., 2008; Bau and Koschinsky, 2009; Kim et al., 2012; Surya Prakash et al., 2012; Bau et al., 2014; Chen et al., 2015; Yang

Table 6
Major-element composition (wt%) of different size fractions of unconsolidated or weakly cemented ooidal ironstones, Arshintsevo outcrop.

Sample	SiO_2	TiO_2	Al_2O_3	Fe_2O_3	FeO	MnO	MgO	CaO	Na_2O	K_2O	P_2O_5	SO_3	LOI	Total
Ar-3-3A	23.16	0.23	5.45	43.23	2.16	2.45	1.21	1.99	1.31	0.49	1.94	0.79	15.71	100.12
Ar-3-3B	26.89	0.26	5.79	42.08	2.08	1.92	1.22	1.91	1.33	0.55	1.66	0.93	14.27	100.89
Ar-3-3C	24.83	0.23	5.52	45.01	1.98	1.26	1.16	1.87	1.18	0.49	1.69	0.82	14.79	100.83
Ar-3-3D	15.05	0.20	4.80	55.30	<0.01	1.26	0.96	1.37	0.89	0.36	2.16	0.33	17.14	99.82
Ar-3-3E	14.26	0.22	4.65	57.80	<0.01	2.03	1.02	1.63	0.89	0.36	2.18	0.10	15.38	100.52
Ar-3-3F	11.86	0.18	3.95	59.99	<0.01	2.27	0.95	1.70	0.80	0.31	2.45	0.40	15.73	100.59
Ar-3-3G	13.14	0.16	3.64	56.49	<0.01	2.36	0.98	2.13	1.07	0.33	3.43	0.24	16.45	100.42
Ar-3-3H	14.76	0.18	4.17	52.27	<0.01	3.31	1.02	2.02	1.02	0.34	2.96	0.25	16.74	99.04
Ar-3-3I	13.38	0.17	4.14	54.98	<0.01	3.96	0.95	1.89	0.79	0.31	2.01	0.16	16.40	99.14
Ar-5-4A	26.14	0.31	7.29	39.50	1.40	2.43	1.07	2.01	1.33	0.79	1.72	0.51	16.14	100.64
Ar-5-4B	27.45	0.30	7.26	38.93	1.58	1.58	1.06	1.83	1.31	0.69	1.53	0.60	15.51	99.63
Ar-5-4C	26.06	0.29	7.13	41.59	1.72	0.92	0.99	1.49	1.19	0.62	1.53	0.14	15.93	99.60
Ar-5-4D	15.32	0.22	5.26	55.46	1.08	0.57	0.78	1.16	0.79	0.40	2.22	<0.03	16.72	99.98
Ar-5-4E	6.15	0.14	3.26	68.12	0.47	0.57	0.62	1.23	0.55	0.19	2.90	<0.03	15.22	99.42
Ar-5-4F	5.71	0.13	2.94	69.26	0.50	0.62	0.67	1.33	0.52	0.21	2.79	<0.03	15.47	100.15
Ar-5-4G	6.16	0.12	2.83	69.99	1.65	0.72	0.65	1.34	0.53	0.20	2.61	<0.03	14.14	100.94
Ar-5-4H	6.49	0.13	2.92	67.80	0.92	0.92	0.63	1.21	0.59	0.21	2.50	0.08	14.83	99.23
Ar-5-4I	7.47	0.14	3.20	65.20	0.48	1.51	0.72	1.68	0.69	0.24	2.38	0.08	15.46	99.25
Ar-9-1A	18.76	0.24	4.78	41.05	<0.01	2.23	0.89	2.65	1.65	0.48	1.36	1.18	23.90	99.17
Ar-9-1B	25.21	0.26	6.82	41.05	<0.01	6.09	0.99	2.12	0.99	0.55	1.38	1.13	13.47	100.06
Ar-9-1C	23.24	0.26	6.47	41.62	<0.01	4.83	0.91	2.25	0.81	0.48	1.50	0.74	15.88	99.99
Ar-9-1D	19.75	0.24	5.95	47.56	<0.01	4.38	0.83	2.14	0.73	0.41	1.73	0.74	15.94	100.40
Ar-9-1E	11.37	0.19	4.49	59.27	<0.01	3.19	0.65	1.72	0.54	0.25	2.42	0.09	15.11	99.29
Ar-9-1F	11.04	0.16	3.86	55.24	<0.01	5.00	0.61	2.86	0.51	0.25	2.25	1.00	16.82	99.60
Ar-9-1G	13.51	0.17	3.90	53.03	<0.01	4.93	0.66	3.18	0.60	0.27	2.46	0.58	15.77	99.06
Ar-9-1H	14.07	0.16	3.85	53.35	<0.01	4.89	0.63	2.48	0.65	0.25	2.51	0.46	16.24	99.54
Ar-9-1I	14.40	0.16	3.71	52.13	<0.01	4.55	0.62	2.82	0.62	0.27	2.92	0.32	16.55	99.07

Fraction size (in mm): $x \leq 0.07$ (A); $0.07 < x \leq 0.1$ (B); $0.01 < x \leq 0.25$ (C); $0.25 < x \leq 0.5$ (D); $0.5 < x \leq 1$ (E); $1 < x \leq 3$ (F); $3 < x \leq 5$ (G); $5 < x \leq 10$ (H), $x > 10$ (I).

Table 7
Trace-element compositions (ppm) of different size fractions of unconsolidated or weakly cemented ooidal ironstones, Arshintsevo outcrop.

Sample	V	Co	Ni	Ga	As	Rb	Sr	Zr	Cs	Ba	Th	U
Ar-3-3A	217	83.7	106	7.33	378	12.3	111	58.5	1.25	1491	14.0	1.59
Ar-3-3B	210	86.5	106	7.92	357	13.5	118	66.1	1.38	1007	14.3	1.50
Ar-3-3C	266	82.7	118	7.30	404	12.5	103	58.7	1.29	247	10.5	1.46
Ar-3-3D	367	92.3	145	5.80	593	10.8	73.7	48.0	1.10	150	6.78	1.61
Ar-3-3E	378	107	157	5.37	631	10.3	90.7	41.7	1.07	247	5.21	2.11
Ar-3-3F	372	109	163	4.87	659	8.79	82.8	41.2	0.92	206	5.10	1.54
Ar-3-3G	308	87.6	136	4.96	644	8.84	112	48.5	0.90	185	5.72	1.39
Ar-3-3H	307	83.9	124	5.16	514	9.25	153	39.0	0.95	269	6.19	1.70
Ar-3-3I	400	107	164	5.08	523	8.58	107	46.2	0.88	226	7.47	2.02
Ar-5-4A	161	142	71.6	9.33	513	21.1	87.2	62.0	2.19	1251	17.1	1.60
Ar-5-4B	146	101	66.5	10.4	493	22.0	80.8	67.4	2.32	779	17.9	1.72
Ar-5-4C	184	51.7	59.9	10.4	489	20.9	65.1	74.5	2.27	259	17.0	1.90
Ar-5-4D	288	43.7	83.7	6.92	744	13.7	42.9	57.6	1.49	115	9.77	1.60
Ar-5-4E	409	49.5	118	3.45	1020	6.55	29.5	38.9	0.73	85.2	6.08	1.56
Ar-5-4F	336	51.7	121	3.20	1041	6.26	33.5	31.0	0.70	85.3	3.84	1.57
Ar-5-4G	264	48.2	112	3.11	1061	6.55	33.6	25.9	0.70	91.9	3.00	1.41
Ar-5-4H	267	41.9	86.8	3.71	967	7.67	44.0	29.8	0.83	110	4.13	1.33
Ar-5-4I	279	35.4	81.9	4.02	944	7.32	51.7	35.1	0.78	128	5.53	1.23
Ar-9-1A	216	90.3	63.6	7.64	415	16.3	119	64.1	1.79	1517	25.9	1.68
Ar-9-1B	205	85.1	61.7	8.08	398	17.3	118	66.5	1.91	1058	24.9	1.85
Ar-9-1C	225	63.0	56.9	7.51	345	16.8	82.2	68.9	1.86	247	21.5	1.51
Ar-9-1D	257	57.3	63.4	6.18	403	14.7	67.9	58.6	1.64	136	14.1	1.41
Ar-9-1E	367	62.0	81.9	4.08	592	9.26	68.0	44.3	1.05	163	9.92	1.72
Ar-9-1F	294	62.8	78.6	4.07	569	8.68	78.6	35.8	0.95	171	6.48	1.59
Ar-9-1G	256	61.7	67.1	4.40	619	9.09	108	35.0	1.00	213	5.98	1.60
Ar-9-1H	261	63.0	64.3	4.37	603	8.77	109	35.2	0.96	186	6.59	1.47
Ar-9-1I	246	59.1	59.0	4.44	595	8.68	122	31.7	0.97	272	6.37	1.68

Fraction size (in mm): $x \leq 0.07$ (A); $0.07 < x \leq 0.1$ (B); $0.01 < x \leq 0.25$ (C); $0.25 < x \leq 0.5$ (D); $0.5 < x \leq 1$ (E); $1 < x \leq 3$ (F); $3 < x \leq 5$ (G); $5 < x \leq 10$ (H), $x > 10$ (I).

et al., 2017). Evidence from experimental (Byrne and Kim, 1990; De Carlo et al., 1997; Ohta and Kawabe, 2000, 2001; Quinn et al., 2006) and natural (e.g., Bau and Koschinsky, 2009; Smith et al., 2008) systems show that co-precipitation of REEs with Fe-rich minerals is accompanied by strong REE + Y fractionation between the solids, sea and/or pore water, as well as within the REE + Y group of elements. Although little has been known so far about the true mineral carriers of REE + Y, the scarce available data on trace-element mineralogy strongly support the

Table 8
Major-element compositions (wt%) of carbonate ironstones, Arshintsevo outcrop: fresh carbonate cores of concretions and oxidized crusts, compared.

Sample	SiO_2	Al_2O_3	Fe_2O_3	FeO	MnO	MgO	CaO	Na_2O	K_2O	P_2O_5	SO_3	LOI	Total
Ar-3-1-s†	8.36	3.81	32.78	1.54	23.82	0.34	4.43	0.01	0.35	1.75	0.14	22.02	99.35
Ar-3-1-ox	10.44	4.47	38.50	3.23	15.47	0.44	4.08	0.17	0.33	1.97	0.21	19.75	99.06
Ar-3-2-s	10.53	3.16	14.70	29.81	6.83	0.34	4.93	0.10	0.35	0.79	0.24	28.01	99.79
Ar-3-2-ox	20.92	4.86	53.79	<0.01	4.09	0.50	0.79	0.06	0.51	1.35	0.20	12.63	99.70
Ar-5-1-s	7.83	3.40	5.80	22.99	19.08	0.57	6.86	0.10	0.25	1.27	0.05	31.63	99.83
Ar-5-1-ox	8.89	3.69	23.35	15.09	7.74	0.41	6.64	0.29	0.26	3.87	2.84	26.42	99.49
Ar-5-2-s	8.77	3.21	9.46	33.55	6.72	0.51	4.24	0.20	0.25	0.65	0.15	32.09	99.80
Ar-5-2-ox	10.51	3.77	33.95	13.40	7.71	0.92	3.89	0.14	0.36	0.91	0.36	23.82	99.74
Ar-5-3-s	10.63	4.16	14.46	15.23	15.09	0.53	8.04	0.24	0.35	2.68	0.49	27.73	99.63
Ar-5-3-ox	13.31	4.72	21.67	10.99	9.52	0.80	7.92	0.50	0.36	4.08	1.80	23.82	99.49
Ar-5-5-s	7.98	3.06	6.61	33.98	9.55	0.47	4.47	0.15	0.33	0.75	0.07	32.43	99.85
Ar-5-5-ox	10.74	3.49	28.83	17.67	8.28	0.61	3.24	0.27	0.32	0.83	0.30	25.02	99.60

Rock type: s = fresh carbonate cores, ox = oxidized crusts. † = fresh carbonate core of concretion, with abundant Fe^{3+}-(oxy)hydroxide allochems.

Table 9
Trace-element compositions (ppm) of carbonate ironstones, Arshintsevo outcrop: fresh carbonate cores of concretions and oxidized crusts, compared.

Sample	Main carbonate	Ti	V	Co	Ni	As	Sr	Ba	Th	U
Ar-3-1-s†	Rds	314	184	31.7	64.5	484	4.50	249	4.16	0.84
Ar-3-1-ox		357	225	44.3	81.2	442	17.7	246	5.05	0.93
Ar-3-2-s	Sd	363	21.5	71.5	106.0	22.9	27.0	996	1.20	0.01
Ar-3-2-ox		453	67.5	56.3	95.3	24.2	48.0	611	1.87	0.51
Ar-5-1-s	Rds	322	14.4	19.5	21.7	15.8	11.8	557	1.12	0.79
Ar-5-1-ox		360	121.0	24.5	44.2	241.0	482	22,165	3.04	1.04
Ar-5-2-s	Sd + Rds	342	46.5	33.3	24.3	25.4	31.7	1331	1.37	0.34
Ar-5-2-ox		376	61.7	34.9	25.7	28.1	83.4	1627	1.67	0.53
Ar-5-3-s	Sd + Rds	408	82.9	27.7	47.4	109.0	118.0	4466	2.44	0.71
Ar-5-3-ox		476	126.0	49.4	70.0	170.0	263.0	11,046	3.54	1.08
Ar-5-5-s	Sd	347	19.4	26.7	19.6	17.3	4.88	739	1.17	0.17
Ar-5-5-ox		387	41.5	32.8	30.9	23.5	53.6	1098	1.57	0.51

Rds = rhodochrosite; Sd = siderite; s = fresh carbonate cores; ox = oxidized crusts; † = fresh carbonate core of concretion, with abundant Fe^{3+}-(oxy)hydroxide allochems.

importance of authigenic REE phosphates (mainly LREE phosphates) as REE carriers in marine sediments, including Fe-rich ones (Rasmussen, 1996; Rasmussen et al., 1998; Rudmin et al., 2020b; Smith et al., 2008). The REE + Y patterns of the Kerch ooidal ironstones highlight the contributions of individual REE carriers to the total REE budget.

5.1.1. *Fe^{3+}-(oxy)hydroxides, clay and detrital minerals*

The Kerch bulk ooidal ironstones, as well as coarse fractions, are mainly composed of goethite and show evident REE enrichment relative to the PAAS values. They have similar shale-normalized REE + Y patterns, with MREE enrichment and a strong negative Y* anomaly (Tables 10 and 11; Fig. 13), which are nearly identical to those of Fe-(oxy) hydroxides (Surya Prakash et al., 2012) and hydrogenic Fe-Mn crusts (Bau et al., 2014). These features of the REE + Y patterns are conventional fingerprints of REE adsorption on Fe^{3+}-(oxy)hydroxides (Kim et al., 2012; Surya Prakash et al., 2012; Yang et al., 2017). Flattened trends of MREE enrichment (expressed as the Gd_N/La_N ratio) *vs* ΣREE indicate that all ooid samples we analyzed have similar percentages of main MREE carriers. The coarse fractions with 85–95% of goethite have the highest MREE contents and Gd_N/La_N ratios (up to 2.41; *Xav* = 2.16), while ΣREE does not exceed 500 ppm. The fine fractions, with lower percentages of Fe^{3+}-(oxy)hydroxides (≤70%), have commensurate Gd_N/La_N ratios (up to 2.22; *Xav* = 2.04) but are richer in ΣREE, mainly at the account of LREE. Therefore, Fe^{3+}-(oxy)hydroxides apparently store most of MREE in the Kerch ooidal ores and provide moderate ΣREE contents, whereas the ΣREE spike of 1153 ppm rather results from greater enrichment in LREE which are stored by other carriers. LREE may potentially reside in clayey phases, detrital heavy minerals, or authigenic REE minerals; each REE carrier is discussed below.

The well-pronounced REE + Y patterns of MREE-enriched and Y-depleted hydrogenic Fe^{3+}-(oxy)hydroxides are commonly attributed to difference in REEs carbonate complexation and subsequent adsorption of REEs on the positively charged surfaces of Fe^{3+}-(oxy)hydroxides (Bau et al., 2014; Ohta and Kawabe, 2000, 2001; Quinn et al., 2006; Surya Prakash et al., 2012). In alkaline solutions (namely in sea water with pH = 7.9), negatively charged bi-carbonate complexes $Ln(CO_3)_2^-$ are predominant for the case of MREE and HREE, while Y occurs as positively charged monocarbonate complex $Y(CO_3)^+$ (Bau and Koschinsky, 2009). Compared to yttrium, HREE complexes are scavenged more on positively charged surfaces of Fe^{3+}-(oxy)hydroxides, which produces an expressed negative Y_N anomaly of the solid host and a large positive Y* anomaly of seawater. HREE sequestration by Fe^{3+}-(oxy)hydroxides during diagenesis likewise produces a MREE-enriched signature in the pore water (Bau et al., 2014).

As described by Yang et al. (2017), the pattern of MREE-enrichment in Fe^{3+}-(oxy)hydroxides during early diagenesis may be as follows. Upon subsiding only few tens of cm, immature Fe-rich sediment moves from the oxygenated pore water zone into the zone where oxygen and other energetically favored oxidants (NO_3^- and Mn^{2+}-(oxy)hydroxides) are consumed and the biotic respiration proceeds through the reduction of Fe^{3+}-(oxy)hydroxides. During the reductive dissolution of primary deposited Fe^{3+}-(oxy)hydroxides, through the mediation by the bacterial and archaeal iron reducers (Raiswell and Canfield, 2012), phosphorus and REE (with MREE enrichment) become desorbed and released into pore water. However, they become re-adsorbed on Fe^{3+}-(oxy)hydroxides as the redox conditions change again (Ruttenberg, 2003; Yang et al., 2017). Thus, coupled P and MREE enrichment can be a geochemical signature of Fe^{3+}-(oxy)hydroxides subject to repeated dissolution and re-precipitation in an early diagenetic process near the oxic/suboxic interface (Yang et al., 2017). As the coupled release of P and MREE is

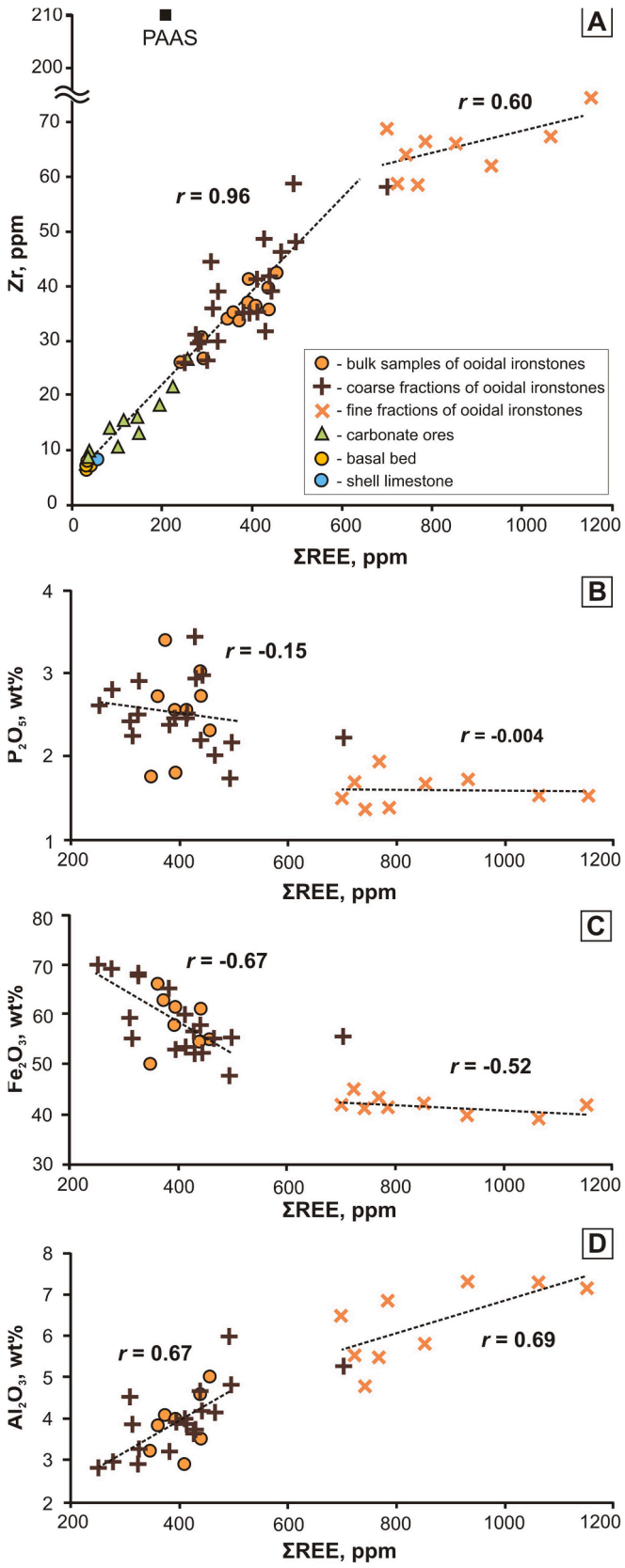

Fig. 12. Zr/ΣREE (A), P_2O_5/ΣREE (B), Fe_2O_3/ΣREE (C) and Al_2O_3/ΣREE (D) ratios in bulk samples and different constituents of ironstones from the Kamysh-Burun deposit, Kerch Peninsula. Element contents are as in Tables 5, 7, 9, 10–12. PAAS composition is according to (Taylor and McLennan, 1985).

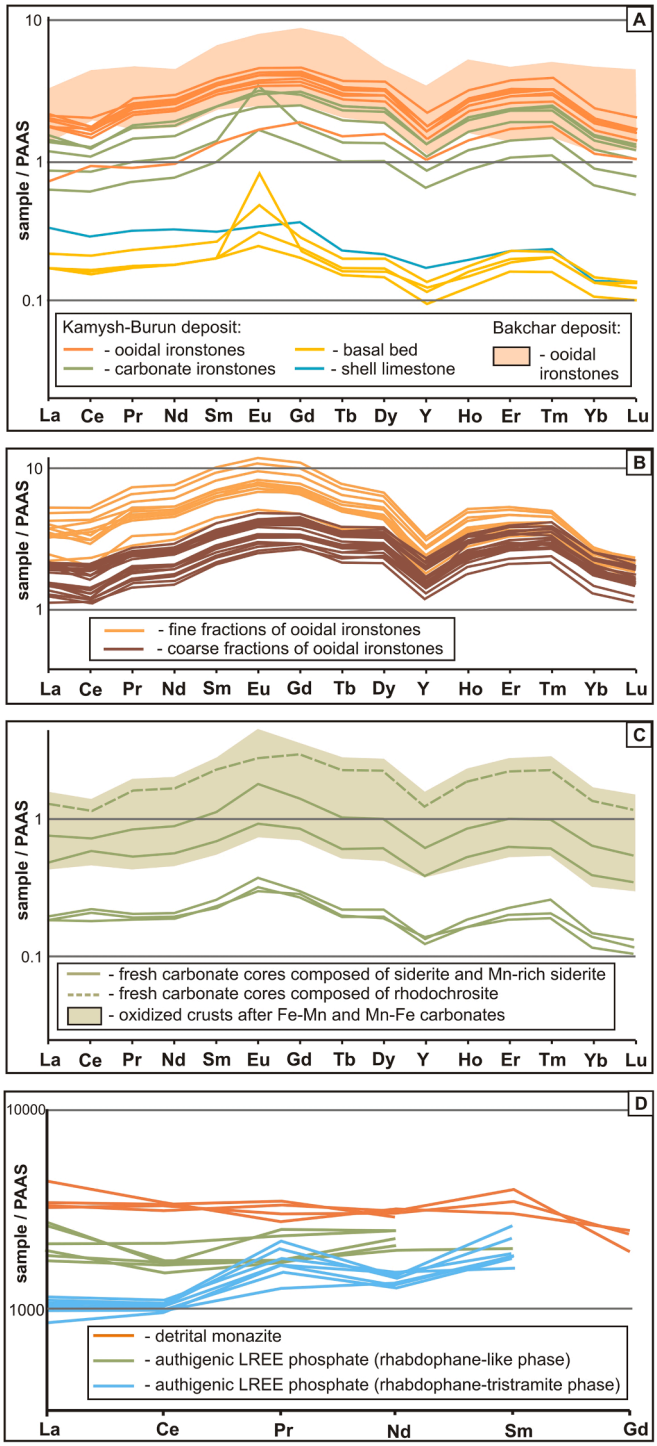

Fig. 13. PAAS-normalized (Taylor and McLennan, 1985) REE + Y spectra of bulk samples and different constituents of ironstones from the Kamysh-Burun deposit, Kerch Peninsula. (A) Kamysh-Burun bulk ironstones in comparison with the ironstones from Bakchar deposit in West Siberia (Rudmin et al., 2019). (B) Fine (<0.25 mm) and coarse (>0.25 mm) fractions of the unconsolidated or weakly cemented ooidal ironstones. (C) Fe-Mn carbonates from carbonate ironstone concretions and nodules. (D) Authigenic LREE phosphates and detrital monazite from ooidal ironstones.

hysteretic, their desorption is never complete, and the total amounts of P and ΣREE captured by Fe^{3+}-(oxy)hydroxides increase with each new oxygenation event. High P and ΣREE contents in pore water during anoxic episodes can lead to precipitation of pore-filling LREE phosphates as it was reported for sandstones (Rasmussen, 1996; Rasmussen et al., 1998) and ironstones (Rudmin et al., 2020b; Smith et al., 2008).

Both Mn-(oxy)hydroxides and clayey minerals with negatively charged surfaces (Sposito et al., 1999) can also act as REE sinks, but cause a different effect on REE + Y fractionation. The greater stability of HREE complexes, such as $Ln(CO_3)_2^-$, in seawater enhances preferential adsorption/sequestration of LREE by clayey particles (Taylor and McLennan, 1985; Bolhar et al., 2004; Xiao et al., 2016; Li et al., 2019). However, no fractionation occurs between Y (as $Y(CO_3)^+$) and HREE, and the negative Y* anomaly disappears (Bau and Koschinsky, 2009; Surya Prakash et al., 2012). Note again that the Kerch ironstone samples we analyzed show a distinct negative Y* anomaly (0.57–0.70) which

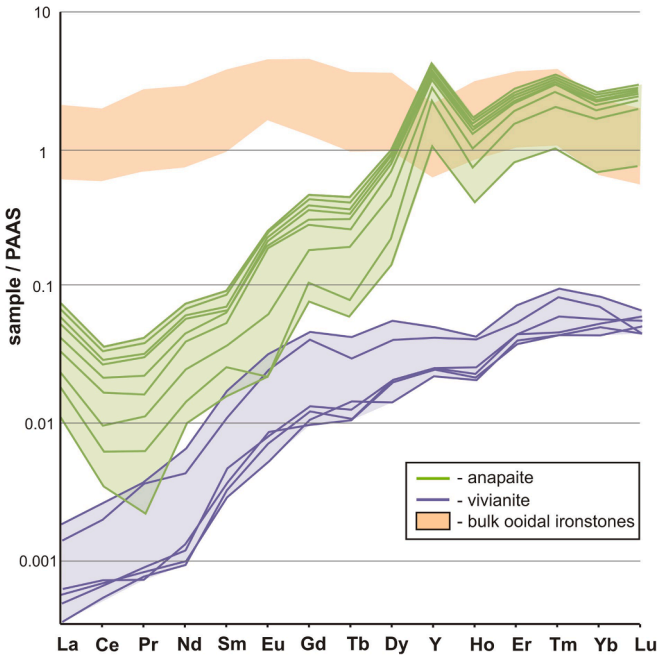

Fig. 14. PAAS-normalized (Taylor and McLennan, 1985) REE + Y spectra of autigenic Fe^{2+}- bearing phosphates (anapaite ($Ca_2Fe^{2+}(PO_4)_2{\cdot}4H_2O$) and vivianite ($Fe^{2+}{}_3(PO_4)_2{\cdot}8H_2O$)) and bulk ooidal ironstones from the Kamysh-Burun deposit, compared.

does not correlate with the Yb_N/La_N ratio (Table 10).

Given the significant positive correlation between ΣREE, SiO_2 and Al_2O_3, it is pertinent to discuss the contribution of clastic material to the ΣREE budget of the Kerch ironstones. The input of illite-dominated river sediments into the ironstones would be expected to produce flattened REE + Y patterns (Taylor and McLennan, 1985; Bolhar et al., 2004; Li et al., 2019; Maslov and Shevchenko, 2019), with weak or absent negative Y_N and Ce_N anomalies. Yet, all REE + Y patterns of the Kerch ooidal ironstones and their fractions look similar and show comparable MREE and HREE enrichments and Yb_N/La_N and Gd_N/La_N ratios. These ratios, as well as the negative Y* and Ce* anomalies, are independent of SiO_2 or Al_2O_3 contents (Tables 6, 10, 11; Fig. 13). For the Y* and Ce* anomalies, the respective *r* values are 0.22 and 0.42 (in the SiO_2 – Y* and SiO_2 – Ce* pairs) and 0.36 and 0.17 (in the Al_2O_3 – Y* and Al_2O_3 – Ce* pairs). Therefore, the contribution of clayey minerals to the ΣREE + Y budget of the Kerch ironstones is minor compared with that of Fe^{3+}-(oxy)hydroxides or LREE phosphates.

The input of detrital heavy minerals is also minor. The Zr contents in all Arshintsevo ore samples (33.6 ppm in bulk ironstones to 74.5 ppm in fine fractions) are much lower than in PAAS (Fig. 12A) and indicate a limited siliciclastic input into the deposition basin. On the other hand, most of the ooidal ironstone samples and all their fractions show prominent ΣREE enrichment over PAAS. The correlation of ΣREE with Zr, indicating progressive contamination of Fe-rich sediments with clastic material from carbonates to ironstones, is significant positive ($r = 0.96$) in the range of low and moderate values of ΣREE but is moderate positive ($r = 0.60$) in ΣREE-rich fine fractions (~600–1150 ppm). Direct mineralogical evidence strongly supports the predominance of relatively abundant authigenic LREE phosphates over sporadic grains of detrital monazite (Table 3).

5.1.2. *Authigenic Fe-Mn carbonates*

Fresh carbonate ironstones are enriched in phosphorus (0.75–2.68 wt%, *Xav* = 1.31 wt% P_2O_5, against 0.44 wt% P_2O_5 in PAAS), but depleted in ΣREE (*Xav* = 103 ppm), though MREE contents are high, with average $Gd_N/La_N = 1.71$ (Table 12; Fig. 13C). Their oxidized varieties have notably higher ΣREE contents (*Xav* = 178 ppm) mainly due to MREE (average $Gd_N/La_N = 2.10$) stored in Fe^{3+}-(oxy)hydroxides that formed after oxidized siderite.

As noted by Yang et al. (2017), less distinct MREE-enriched patterns can be frequently preserved by authigenic phases (both phosphates and carbonates), which precipitate in a suboxic/dysoxic zone directly from MREE-enriched pore water that impregnates the sediment rich in Fe^{3+}-(oxy)hydroxides. These very features appear in the REE + Y patterns of fresh carbonate ironstones from the upper part of the Arshintsevo sequence. Their rhythmic alternation with ooidal ironstones is direct evidence of ironstone deposition in oscillating redox conditions of a shallow sedimentary basin. The rhodochrosite layers were deposited in moderately reduced environments because Mn^{2+} equilibrated with Fe^{3+}-(oxy)hydroxides became reduced ahead of Fe^{2+}. The siderite layers mark episodes of dysoxic (but not euxinic) conditions which maintained partial reduction of Fe^{3+}-(oxy)hydroxides and release of Fe^{2+}, orthophosphates and REE into pore water (Rue et al., 1997; Romanek et al., 2009; Cutter et al., 2018; Sokol et al., 2018).

The REE + Y signatures indicate that the time of Fe- and Mn-carbonate deposition and carbonate cementation of allochems corresponded to the events of decreasing pore water oxygenation and partial reduction of Fe^{3+}-(oxy)hydroxides. The fresh carbonate ironstones (type 2) captured minor amounts of REE and have no economic significance as REE carriers.

A positive Eu* anomaly (Fig. 13C), which is especially prominent in samples from the basal bed with abundant shell detritus, is another fingerprint of REE + Y patterns in fresh carbonate sediments. High Eu* values may suggest hydrothermal inputs to seawater in the time of deposition (Bau et al., 1995), but this hypothesis is inconsistent with the Early Pliocene history of the Kerch region (Nedumov, 1994; Golubovskaya, 2001; Popov et al., 2004, 2010; Kholodov et al., 2014). A better explanation can come rather from the crystal chemistry of carbonate minerals. The REE concentrations in $CaCO_3$ modifications are primarily controlled by the availability of REEs in the solution, whereas Eu and Ce depend also on their oxidation state. Calcite is relatively enriched in LREEs since Ca^{2+} and LREE ions have similar sizes, while the smaller ionic radius of HREEs makes their incorporation into calcite more difficult (Barker, 2007). According to experimental data by Lakshtanov and Stipp (2004), Eu^{3+} incorporates into calcite via the vacancy-substitution mechanism, at a partition coefficient of $10^{2.89}$,

Table 10
Yttrium and REE concentrations (ppm) in bulk ironstones and Pontian shell limestone, Arshintsevo outcrop. ICP-MS data.

Sample	Rock type	Y	La	Ce	Pr	Nd	Sm	Eu	Gd	Tb	Dy	Ho	Er	Tm	Yb	Lu	ΣREE	Ce*	Y*	Yb_N/La_N	Gd_N/La_N	Gd_N/Yb_N	Y_N/Ho_N
Ironstone sequence																							
Ar-3-1	c	35.9	54.0	99.4	15.3	61.0	13.7	3.21	14.4	1.89	11.1	2.02	5.39	0.73	4.24	0.55	287	0.75	0.60	1.06	2.19	2.06	0.65
Ar-3-2	c	27.6	27.6	73.7	7.96	32.4	7.57	1.82	8.78	1.16	7.31	1.39	3.91	0.53	3.19	0.45	178	1.09	0.69	1.57	2.61	1.67	0.73
Ar-3-3	o	49.6	76.8	173	24.2	97.9	21.1	4.80	21.2	2.68	15.6	2.82	7.53	1.00	5.95	0.78	455	0.84	0.59	1.05	2.26	2.16	0.65
Ar-3-4	c	29.3	45.2	85.9	12.8	51.4	11.5	2.61	11.7	1.52	8.86	1.61	4.37	0.57	3.41	0.45	242	0.78	0.62	1.02	2.12	2.08	0.67
Ar-3-4/1	c	37.2	52.8	101	15.3	60.9	13.9	3.26	14.6	1.92	11.3	2.03	5.43	0.74	4.32	0.57	288	0.76	0.62	1.11	2.27	2.05	0.67
Ar-4-1	o	43.7	67.9	133	19.7	79.4	17.9	4.02	18.0	2.31	13.6	2.44	6.69	0.89	5.22	0.69	372	0.79	0.60	1.04	2.17	2.09	0.66
Ar-5-1	c	17.6	23.9	49.1	6.35	26.0	5.59	1.81	6.06	0.77	4.71	0.86	2.45	0.33	1.90	0.25	130	0.92	0.70	1.08	2.08	1.93	0.75
Ar-5-3	c	23.3	33.0	67.0	8.73	36.0	7.82	3.73	8.44	1.06	6.31	1.19	3.25	0.44	2.50	0.34	180	0.92	0.68	1.03	2.10	2.04	0.72
Ar-5-4	o	43.9	67.5	123	19.4	78.5	17.4	3.91	17.2	2.27	13.7	2.47	6.65	0.91	5.43	0.71	359	0.74	0.60	1.09	2.09	1.92	0.65
Ar-6-1	o	47.5	77.3	139	22.6	91.3	19.9	4.49	19.5	2.52	14.7	2.66	7.06	0.97	5.52	0.72	408	0.72	0.60	0.97	2.07	2.14	0.66
Ar-7-1	c	36.0	58.1	97.4	15.9	65.2	13.9	3.43	13.9	1.78	10.5	1.94	5.26	0.69	3.98	0.52	292	0.73	0.63	0.93	1.96	2.11	0.68
Ar-7-2	o	38.9	67.0	117	18.8	77.0	16.7	3.71	16.1	2.13	12.5	2.26	6.02	0.80	4.68	0.61	345	0.74	0.58	0.95	1.97	2.08	0.63
Ar-8-1	o	44.5	74.0	132	21.7	87.3	19.4	4.42	18.9	2.54	14.8	2.63	6.99	0.96	5.58	0.72	392	0.71	0.57	1.02	2.09	2.05	0.62
Ar-9-1	o	59.5	82.6	141	24.7	99.6	21.8	4.97	21.6	2.89	17.2	3.18	8.66	1.17	6.72	0.89	437	0.67	0.64	1.10	2.14	1.95	0.69
Ar-10-1	o	48.3	80.7	161	22.8	93.0	20.2	4.62	20.1	2.63	15.4	2.79	7.54	0.99	5.68	0.74	438	0.84	0.59	0.95	2.04	2.14	0.64
Ar-11-1	o	47.6	74.1	131	20.9	86.5	19.4	4.42	19.7	2.59	15.2	2.71	7.32	0.97	5.64	0.73	391	0.75	0.59	1.03	2.18	2.11	0.64
Basal bed																							
Ar-12-3-1	o	3.47	6.85	12.6	1.55	6.24	1.15	0.89	1.07	0.13	0.78	0.15	0.45	0.06	0.39	0.06	32.4	0.95	0.80	0.77	1.28	1.66	0.84
Ar-12-3-2	o	3.22	6.66	13.0	1.56	6.28	1.18	0.34	1.13	0.13	0.81	0.16	0.47	0.06	0.39	0.06	32.2	0.97	0.70	0.79	1.39	1.75	0.72
Ar-12-3-3	o	3.79	8.53	17.2	2.11	8.50	1.53	0.53	1.35	0.16	0.96	0.18	0.53	0.07	0.43	0.06	42.1	0.95	0.73	0.68	1.30	1.90	0.77
Ar-12-8	o	2.63	6.61	13.3	1.60	6.21	1.15	0.27	0.97	0.12	0.70	0.13	0.38	0.05	0.31	0.05	31.8	0.93	0.70	0.64	1.20	1.89	0.77
Shell limestone																							
Ar-13-1	lm	4.83	13.0	23.9	2.87	11.4	1.81	0.38	1.76	0.18	1.05	0.20	0.54	0.07	0.41	0.06	57.6	0.96	0.84	0.43	1.11	2.60	0.88

Rock type: c = carbonate ironstone, o = ooidal ironstone, lm = shell limestone. $Ce^* = Ce_N/(2Pr_N - Nd_N)$; $Y^* = Y_N/(½\ Dy_N + ½\ Ho_N)$, after (Bolhar et al., 2004). Subscript 'N' stands for PAAS-normalized (Post-Archean Australian Shale, after Taylor and McLennan (1985)).

Table 11
Yttrium and REE concentrations (ppm) in different size fractions of unconsolidated or weakly cemented ooidal ironstones, Arshintsevo outcrop. ICP-MS data.

Sample	Y	La	Ce	Pr	Nd	Sm	Eu	Gd	Tb	Dy	Ho	Er	Tm	Yb	Lu	ΣREE	Ce*	Y*	Yb_N/La_N	Gd_N/La_N	Gd_N/Yb_N	Y_N/Ho_N
Ar-3-3A	73.3	129	299	40.6	166	36.3	8.35	34.9	4.37	24.5	4.22	11.0	1.41	7.89	1.00	769	0.87	0.57	0.83	2.22	2.68	0.64
Ar-3-3B	73.8	145	336	45.5	185	40.0	9.08	37.3	4.58	25.3	4.27	10.9	1.38	7.74	0.96	853	0.87	0.56	0.72	2.11	2.92	0.63
Ar-3-3C	66.5	124	281	38.5	157	33.8	7.60	32.3	3.90	22.2	3.77	9.63	1.27	7.01	0.90	723	0.86	0.58	0.77	2.14	2.79	0.65
Ar-3-3D	53.8	84.4	188	25.8	107	23.2	5.29	22.6	2.89	17.1	3.02	8.27	1.09	6.42	0.85	496	0.88	0.59	1.03	2.20	2.13	0.65
Ar-3-3E	51.5	77.9	164	22.3	91.5	20.1	4.59	20.1	2.66	16.0	2.91	7.93	1.07	6.39	0.86	438	0.88	0.60	1.11	2.12	1.90	0.65
Ar-3-3F	53.1	72.3	151	20.7	85.2	19.1	4.43	19.5	2.64	16.0	2.97	8.22	1.13	6.60	0.89	411	0.87	0.61	1.24	2.21	1.79	0.66
Ar-3-3G	53.9	75.8	158	21.7	88.4	19.9	4.60	20.3	2.72	16.3	3.00	8.27	1.13	6.54	0.87	428	0.86	0.61	1.17	2.20	1.88	0.66
Ar-3-3H	56.9	79.4	161	22.5	93.0	20.8	4.77	21.1	2.79	16.7	3.08	8.37	1.12	6.46	0.86	442	0.86	0.63	1.10	2.18	1.98	0.68
Ar-3-3I	58.8	81.4	166	24.1	99.6	22.9	5.28	22.6	3.03	18.1	3.26	8.85	1.18	7.04	0.91	464	0.83	0.61	1.17	2.28	1.94	0.66
Ar-5-4A	76.7	164	345	52.2	213	46.5	10.6	42.5	5.17	27.8	4.53	11.1	1.37	7.39	0.89	932	0.78	0.54	0.61	2.12	3.48	0.62
Ar-5-4B	85.2	188	394	60.1	244	53.6	12.0	48.3	5.72	30.4	4.95	11.9	1.47	7.73	0.92	1063	0.77	0.55	0.56	2.11	2.78	0.63
Ar-5-4C	89.7	205	425	65.8	266	59.1	13.1	52.5	6.19	32.6	5.19	12.4	1.50	7.87	0.96	1153	0.76	0.54	0.52	2.10	4.04	0.63
Ar-5-4D	62.7	125	253	39.7	162	35.5	7.93	32.1	4.02	22.0	3.67	9.28	1.19	6.64	0.82	703	0.75	0.55	0.72	2.11	2.93	0.63
Ar-5-4E	45.2	58.5	110	17.3	70.6	15.7	3.63	15.9	2.22	13.9	2.60	7.25	0.98	5.97	0.81	325	0.75	0.60	1.38	2.23	1.61	0.64
Ar-5-4F	41.9	48.7	93.6	14.3	58.6	13.2	3.06	13.9	1.97	12.4	2.34	6.70	0.94	5.62	0.76	276	0.78	0.62	1.56	2.34	1.50	0.66
Ar-5-4G	38.5	42.5	90.0	12.5	50.7	11.7	2.74	12.5	1.78	11.2	2.13	6.01	0.83	5.09	0.68	250	0.85	0.63	1.62	2.41	1.49	0.66
Ar-5-4H	41.2	57.7	114	16.9	69.6	15.4	3.60	15.4	2.12	12.8	2.35	6.51	0.89	5.28	0.7	323	0.81	0.60	1.24	2.19	1.77	0.64
Ar-5-4I	43.9	69.8	136	20.2	83.2	18.2	4.22	17.6	2.36	13.8	2.48	6.73	0.89	5.25	0.68	381	0.81	0.60	1.02	2.07	2.03	0.65
Ar-9-1A	57.9	145	252	44.1	176	38.1	8.47	32.8	3.98	21.6	3.49	8.52	1.07	5.94	0.72	742	0.66	0.53	0.55	1.85	3.34	0.61
Ar-9-1B	59.2	155	269	47.0	185	39.8	8.76	34.0	4.12	22.3	3.56	8.55	1.08	5.98	0.71	785	0.65	0.52	0.52	1.80	3.44	0.61
Ar-9-1C	55.1	136	232	42.0	170	36.5	7.99	31.4	3.83	20.7	3.31	8.09	1.02	5.53	0.67	699	0.65	0.53	0.55	1.89	3.44	0.61
Ar-9-1D	45.1	95.3	162	29.4	118	25.6	5.61	22.5	2.87	15.8	2.64	6.79	0.87	4.95	0.64	493	0.64	0.55	0.70	1.94	2.75	0.63
Ar-9-1E	40.8	58.1	96.9	17.6	70.4	15.9	3.68	15.6	2.19	13.2	2.36	6.51	0.89	5.32	0.71	309	0.64	0.58	1.24	2.20	1.77	0.63
Ar-9-1F	42.3	58.7	102	17.2	69.9	15.6	3.61	15.6	2.13	13.1	2.39	6.57	0.89	5.27	0.69	314	0.70	0.60	1.22	2.18	1.79	0.65
Ar-9-1G	51.9	76.8	130	21.4	86.3	18.8	4.30	18.8	2.6	15.7	2.88	7.92	1.08	6.32	0.83	394	0.71	0.61	1.11	2.01	1.80	0.66
Ar-9-1H	48.9	81.2	138	22.6	91.2	19.7	4.42	19.0	2.54	15.4	2.81	7.65	1.03	6.10	0.80	412	0.71	0.59	1.02	1.92	1.88	0.64
Ar-9-1I	62.9	82.9	140	23.1	94.2	20.5	4.71	20.9	2.85	17.5	3.33	9.25	1.26	7.26	0.96	429	0.72	0.66	1.19	2.07	1.74	0.69
Xav(A-C)	70.8	155	315	48.4	196	42.6	9.55	38.4	4.65	25.3	4.14	10.2	1.29	7.01	0.86	858	0.76	0.55	0.63	2.04	3.32	0.63
σ(A-C)	12.1	27.1	65.3	9.24	37.5	8.64	1.92	7.62	0.85	4.18	0.66	1.58	0.18	0.94	0.12	160	0.09	0.02	0.11	0.15	0.45	0.01
min(A-C)	55.1	124	232	38.5	157	33.8	7.60	31.4	3.83	20.7	3.31	8.09	1.02	5.53	0.67	699	0.65	0.52	0.52	1.80	2.68	0.61
max(A-C)	89.7	205	425	65.8	266	59.1	13.1	52.5	6.19	32.6	5.19	12.4	1.50	7.89	1.00	1153	0.87	0.58	0.83	2.22	4.04	0.65
Xav(D-I)	49.6	73.7	142	21.6	88.3	19.5	4.47	19.2	2.58	15.4	2.79	7.62	1.03	6.03	0.80	405	0.78	0.60	1.16	2.16	1.93	0.65
σ(D-I)	7.67	18.9	40.1	6.10	24.9	5.34	1.16	4.45	0.51	2.54	0.41	1.01	0.13	0.71	0.09	104	0.08	0.03	0.23	0.13	0.37	0.02
min(D-I)	38.5	42.5	90.0	12.5	50.7	11.7	2.74	12.5	1.78	11.2	2.13	6.01	0.83	4.95	0.64	250	0.64	0.55	0.70	1.92	1.49	0.63
max(D-I)	62.9	125	253	39.7	162	35.5	7.93	32.1	4.02	22.0	3.67	9.28	1.26	7.26	0.96	703	0.88	0.66	1.61	2.41	2.93	0.69

Xav = mean value; σ = standard deviation; min = minimum value; max = maximum value. $Ce^* = Ce_N/(2Pr_N - Nd_N)$; $Y^* = Y_N/(½\ Dy_N + ½\ Ho_N)$ (after Bolhar et al. (2004)). Subscript 'N' stands for PAAS-normalized (Post-Archean Australian Shale, after Taylor and McLennan (1985)).

Table 12
Yttrium and REE concentrations (ppm) in carbonate ironstones, Arshintsevo outcrop: fresh carbonate cores of concretions and oxidized crusts, compared. ICP-MS data.

Sample	Y	La	Ce	Pr	Nd	Sm	Eu	Gd	Tb	Dy	Ho	Er	Tm	Yb	Lu	ΣREE	Ce*	Y*	Yb_N/La_N	Gd_N/La_N	Gd_N/Yb_N	Y_N/Ho_N
Ar-3-1-s†	32.0	47.8	88.9	13.6	54.8	12.2	2.87	13.0	1.67	10.0	1.78	4.88	0.65	3.74	0.49	256	0.76	0.60	1.06	2.23	2.10	0.66
Ar-3-1-ox	40.2	56.1	105	16.0	64.5	14.6	3.39	15.4	2.02	12.0	2.18	5.93	0.80	4.56	0.62	303	0.77	0.63	1.10	2.25	2.04	0.68
Ar-3-2-s	3.69	7.53	17.5	1.81	7.02	1.44	0.40	1.38	0.17	1.03	0.19	0.52	0.08	0.42	0.06	39.5	1.08	0.67	0.76	1.50	1.99	0.72
Ar-3-2-ox	22.6	18.1	45.8	4.91	20.2	4.90	1.27	6.17	0.85	5.46	1.09	3.13	0.43	2.64	0.36	115	1.11	0.74	1.98	2.79	1.41	0.76
Ar-5-1-s	3.79	7.28	14.3	1.65	6.43	1.28	0.32	1.32	0.15	0.89	0.16	0.43	0.06	0.33	0.05	34.7	0.98	0.79	0.61	1.49	2.42	0.85
Ar-5-1-ox	23.2	34.6	72.7	9.53	39.0	8.57	4.51	8.97	1.16	6.99	1.28	3.54	0.47	2.71	0.37	194	0.91	0.62	1.06	2.13	2.00	0.67
Ar-5-2-s	10.3	18.2	45.6	4.63	18.7	3.75	0.97	3.88	0.46	2.81	0.51	1.40	0.18	1.08	0.15	102	1.15	0.68	0.80	1.75	2.17	0.74
Ar-5-2-ox	16.3	26.9	64.9	6.61	27.0	5.40	1.37	5.72	0.69	4.06	0.77	2.14	0.28	1.59	0.22	148	1.16	0.73	0.80	1.74	2.18	0.78
Ar-5-3-s	16.4	28.0	56.2	7.23	29.4	6.11	1.86	6.35	0.77	4.57	0.82	2.24	0.29	1.77	0.23	146	0.92	0.67	0.86	1.86	2.17	0.73
Ar-5-3-ox	29.5	41.3	84.5	11.1	45.4	9.86	3.38	10.4	1.33	8.13	1.51	4.14	0.56	3.31	0.44	225	0.90	0.67	1.09	2.06	1.90	0.72
Ar-5-5-s	3.39	7.12	16.4	1.67	6.62	1.26	0.34	1.26	0.15	0.91	0.16	0.46	0.06	0.39	0.05	36.9	1.13	0.70	0.74	1.45	1.96	0.76
Ar-5-5-ox	10.3	16.5	36.6	3.83	15.5	3.08	0.79	3.22	0.40	2.35	0.44	1.21	0.16	0.92	0.13	85.1	1.12	0.81	0.75	1.60	2.12	0.86
Xav(s)	11.6	19.3	39.8	5.10	20.5	4.34	1.13	4.53	0.56	3.37	0.60	1.66	0.22	1.29	0.17	103	1.00	0.69	0.78	1.71	2.14	0.75
σ(s)	11.2	16.3	29.7	4.72	19.1	4.30	1.04	4.61	0.60	3.56	0.63	1.73	0.23	1.32	0.17	87.7	0.15	0.06	4.35	0.30	0.17	0.06
min(s)	3.39	7.12	14.3	1.65	6.43	1.26	0.32	1.26	0.15	0.89	0.16	0.43	0.06	0.33	0.05	34.7	0.76	0.60	1.06	1.45	1.96	0.66
max(s)	32.0	47.8	88.9	13.6	54.8	12.2	2.87	13.0	1.67	10.0	1.78	4.88	0.65	3.74	0.49	256	1.15	0.79	0.61	2.23	2.42	0.85
Xav(ox)	23.7	32.3	68.2	8.66	35.3	7.74	2.45	8.31	1.08	6.50	1.21	3.35	0.45	2.62	0.36	178	1.00	0.70	1.02	2.10	1.94	0.74
σ(ox)	10.4	15.1	25.1	4.52	18.2	4.18	1.50	4.30	0.57	3.39	0.61	1.64	0.22	1.28	0.17	79.5	0.16	0.07	3.45	0.42	0.28	0.07
min(ox)	10.3	16.5	36.6	3.83	15.5	3.08	0.79	3.22	0.40	2.35	0.44	1.21	0.16	0.92	0.13	85.1	0.77	0.62	1.96	1.60	1.41	0.67
max(ox)	40.2	56.1	105	16.0	64.5	14.6	4.51	15.4	2.02	12.0	2.18	5.93	0.80	4.56	0.62	303	1.16	0.81	0.75	2.79	2.18	0.86

Rock type: s = fresh carbonate cores, ox = oxidized crusts; † = fresh carbonate core of a concretion, with numerous Fe^{3+}-(oxy)hydroxide allochems. *Xav* = mean value; σ = standard deviation; min = minimum value; max = maximum value. $Ce^* = Ce_N/(2Pr_N - Nd_N)$; $Y^* = Y_N/(½\ Dy_N + ½\ Ho_N)$ (after Bolhar et al. (2004)). Subscript 'N' stands for PAAS-normalized (Post-Archean Australian Shale, after Taylor and McLennan (1985)).

mainly due to similar effective ionic radiuses of sixfold-coordinated Ca^{2+} (1.00 Å) and Eu^{3+} (0.947 Å) (Shannon, 1976). Furthermore, Schmidt et al. (2009) revealed structural incorporation of Eu^{3+} into aragonite. The incorporation of Eu^{2+} into the lattice of both $CaCO_3$ modifications occurs by isovalent substitutions, preferably for Sr^{2+}-bearing phases (such as Sr-rich biogenic aragonite), because sixfold-coordinated Sr^{2+} and Eu^{2+} have almost identical effective ionic radii of 1.18 Å and 1.17 Å, respectively (Barker, 2007). Thus, calcite and/or Sr-rich biogenic aragonite, being favorable hosts for lattice incorporation of both Eu^{2+} and Eu^{3+}, create a prerequisite for the positive Eu* anomaly in some marine sediments.

5.1.3. *Fe^{2+}-bearing phosphates*

The Kerch ironstone strata store high percentages of vivianite (and/or its oxidative derivatives) and less abundant anapaite, whereas apatite group minerals are scarce in these rocks and were found only as pseudomorphs after wood and bones of water mammals (Chukanov, 2005). The preferable formation of Fe^{2+}-bearing phosphates instead of apatite was maintained by high activity of Fe^{2+} in pore water at low fluorine activity (Rothe et al., 2016). Both vivianite and anapaite in the Kerch ooidal ironstones are poor REE carriers with only 0.58–30.0 ppm ΣREE (Table 13).

No direct measurements of REE + Y signatures in Fe^{2+}-bearing phosphates have been undertaken before, though these data are crucial for understanding REE fractionation during diagenesis of Fe-rich sediments (Yang et al., 2017). Vivianite and anapaite, which have been analyzed by LA-ICPMS, show similar PAAS-normalized REE + Y patterns, especially with regard to MREE and HREE: (i) HREE enrichment relative to LREE, (ii) negative Ce* anomaly, (iii) positive Y* and Eu* anomalies, and (iv) high Y_N/Ho_N ratios (Fig. 14; Table 13). Anapaite has higher ΣREE contents and prominent anomalies indicative of its seawater-derived REE + Y source. Vivianite contains lesser amounts of ΣREE (0.58–1.73 ppm; 0.93 ppm on average), with less distinct anomalies. These features turn out to be typical of hydrogenic compounds that formed in anoxic water (Yang et al., 2017).

Vivianite is an early-diagenetic mineral that grows immediately in Fe-rich sediments below the sulfate/methane transition zone, where pore waters are enriched in Fe^{2+} and $(PO_4)^{3-}$ while sulfidic sulfur has already precipitated (Hsu et al., 2014; Egger et al., 2015; Rothe et al., 2016; Yang et al., 2017). Fe^{3+}-(oxy)hydroxides were considered (Melton et al., 2014; Rothe et al., 2016) as an important precursor phase for vivianite as they can supply Fe^{2+} and $(PO_4)^{3-}$ into pore water due to microbial and/or chemical reduction of Fe^{3+} and subsequent re-adsorption of orthophosphate. Indeed, the textural features support the formation of vivianite after Fe^{3+}-(oxy)hydroxide allochems (Fig. 6B) in the Kerch ironstones. Some Fe^{2+} phosphates in the Kerch ooidal ores may have formed in this way, but the optimal conditions for the growth of abundant and perfect vivianite crystals existed in restricted volumes where degradation of protein bodies of large mollusks (Fig. 6D) released phosphorus as $(PO_4)^{3-}$ while microbial activity led to the reduction of Fe^{3+} by dissimilatory metal reducing bacteria (Rothe et al., 2016). Additionally, the sediment accumulated phosphorus that was released during decomposition of organic matter in aerobic organisms and became adsorbed onto large surfaces of predominant Fe^{3+}-(oxy)hydroxides and less abundant IS particles. The C, N and P nutrients liberated in this process were related as $(CH_2O)_{106}(NH_3)_{16}(H_3PO_4) + 138O_2 \rightarrow 106CO_2 + 122H_2O + 16HNO_3 + H_3PO_4$ (Rasmussen, 1996).

Perfect anapaite crystals (Fig. 6A,C) formed by another way in the open space of thin cracks that cut the upper oolite bed (Ar-3). The cracks result from brittle deformation of the solidified ore beds, i.e., the crystallization of anapaite obviously postdated the deposition and deformation of consolidated ironstones. It apparently occurred during a transgression of the shallow Cimmerian paleo-sea (Shnyukov, 1965; Nedumov, 1994; Golubovskaya, 2001; Popov et al., 2004, 2010; Kholodov et al., 2014), when the cracks became filled with brackish lagoonal water as the ore bed submerged. The anapaite crystals show

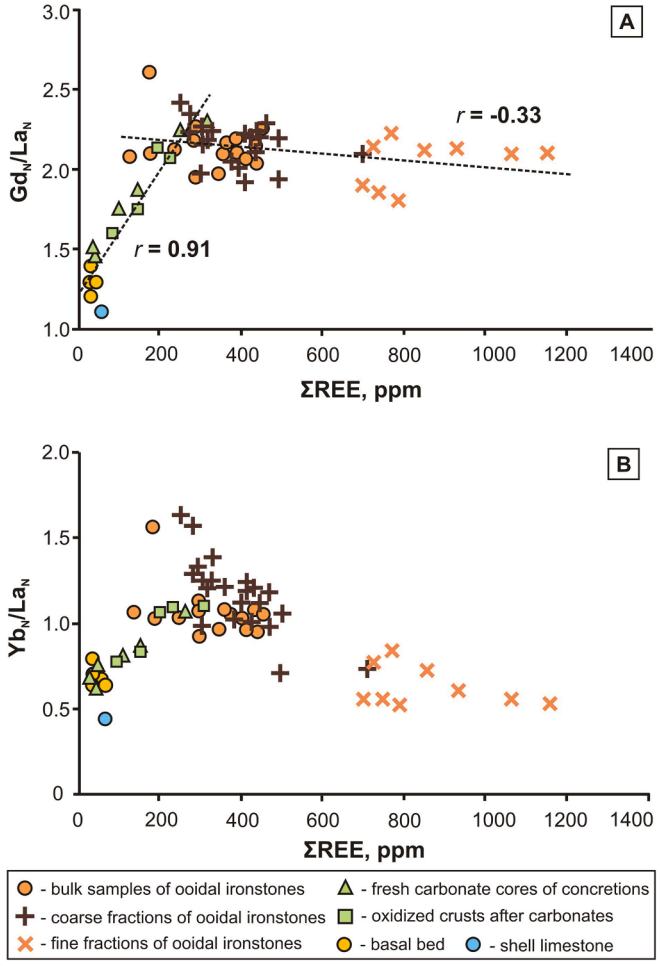

Fig. 15. Compositions of bulk samples and different constituents of the Kamysh-Burun ironstones in the coordinates Gd_N/La_N – ΣREE (A) and Yb_N/La_N – ΣREE (B). Element contents are as in Tables 10 and 12.

neither any zoning pattern, nor evidence of regeneration, etching or overgrowth that would indicate a single event of crack opening followed by an event of water injection and anapaite growth. Like the case of vivianite, the processes of Fe^{3+}-(oxy)hydroxide reduction to Fe^{2+} and related release of phosphates were mediated by metal reducing bacteria (Melton et al., 2014; Rothe et al., 2016). This inference is supported by the coexistence of anapaite with scarce siderite and pyrite. The brackish seawater contained high Mg^{2+} and $(SO_4)^{2-}$ contents, as well as moderate amounts of Ca (≥400 ppm) (Alibo and Nozaki, 1999). With these mineral-forming (Fe, Ca, and P) and impurity (Mg and S) elements mobilized into anapaite, it acquired the composition $(Ca_{1.93\text{-}2.0})(Fe_{0.89\text{-}1.01}Mg_{0.02\text{-}0.13}Mn_{0.01\text{-}0.08})(P_{1.96\text{-}2.01}S_{0.0\text{-}0.02})O_8{\cdot}4H_2O$ (N = 103).

5.1.4. REE phosphates

The REE-rich microphases revealed for the first time in the Kerch ooidal ironstones include predominant authigenic hydrous LREE phosphates (rhabdophane and more hydrated rhabdophane-like phases), less abundant Th-bearing detrital monazite, and scarce xenotime grains. The rhabdophane–like phases ($LREE(PO_4){\cdot}nH_2O$) commonly occur as a few micro-patches in layers with moderate bulk ΣREE contents (Fig. 10). The beds of cement-free ooidal ironstones (Ar-3, Ar-5 and Ar-9), with the highest ΣREE in bulk samples and especially in fine fractions (Fig. 11), contain clusters of subhedral grains of hydrous LREE phosphates. Their compositions correspond to a solid solution or a submicron mixture of a rhabdophane-like phase and tristramite. The textural relationships of REE minerals and the host Fe^{3+}-(oxy)hydroxides provide evidence that hydrous LREE-Ca phosphate-sulfate nucleated repeatedly and

Table 13
Yttrium and REE concentrations (ppm) in anapaite and vivianite, Arshintsevo outcrop. LA-ICPMS data.

Sample	Y	La	Ce	Pr	Nd	Sm	Eu	Gd	Tb	Dy	Ho	Er	Tm	Yb	Lu	ΣREE	Y*	Yb_N/La_N	Gd_N/La_N	Gd_N/Yb_N	Y_N/Ho_N
Anapaite																					
Anp-11-1	28.8	0.43	0.30	0.02	0.35	0.07	0.02	0.35	0.05	0.69	0.41	1.86	0.31	1.99	0.34	7.19	3.78	62.4	6.64	0.11	2.56
Anp-11-2	30.6	0.26	0.21	0.04	0.16	0.06	0.01	0.11	0.02	0.41	0.33	1.65	0.29	2.79	0.52	6.84	5.39	144	3.50	0.02	3.40
Anp-15	16.1	0.18	0.27	0.04	0.36	0.03	0.04	0.35	0.10	1.11	0.28	0.85	0.18	0.81	0.15	4.75	2.28	62.0	16.2	0.26	2.08
Anp-29	11.7	0.40	0.53	0.02	0.67	0.14	0.11	0.45	0.06	1.23	0.23	0.53	0.12	0.63	0.11	5.23	1.75	21.3	9.22	0.43	1.87
Anp-26	4.80	0.30	0.36	0.05	0.20	0.05	0.004	0.09	0.04	0.45	0.08	0.32	0.02	0.39	0.04	2.38	1.97	17.9	2.44	0.14	2.10
Anp-311	4.44	0.21	0.18	0.01	0.11	0.02	0.01	0.12	0.02	0.20	0.06	0.29	0.05	0.30	0.05	1.62	3.08	20.1	4.60	0.23	2.55
Anp-310	4.30	0.34	0.35	0.06	0.34	0.10	0.03	0.23	0.04	0.32	0.09	0.25	0.04	0.28	0.04	2.50	1.95	11.1	5.64	0.51	1.68
Anp-411	4.64	0.26	0.24	0.03	0.15	0.03	0.005	0.12	0.03	0.27	0.09	0.29	0.04	0.32	0.06	1.94	2.40	16.4	3.83	0.23	2.00
Anp-51	33.3	3.26	6.03	0.89	4.18	1.22	0.42	2.23	0.44	3.68	0.94	3.00	0.41	2.92	0.43	30.0	1.42	12.4	5.61	0.45	1.30
Vivianite																					
Viv-75331-1	0.70	0.02	0.06	0.01	0.04	0.03	0.01	0.06	0.01	0.10	0.03	0.11	0.02	0.17	0.03	0.68	1.09	116	26.6	0.23	0.98
Viv-75331-2	0.70	0.03	0.06	0.01	0.05	0.02	0.01	0.05	0.01	0.10	0.02	0.09	0.01	0.13	0.02	0.60	1.20	69.3	15.6	0.23	1.16
Viv-75331-3	0.72	0.01	0.05	0.01	0.03	0.02	0.01	0.06	0.01	0.10	0.02	0.11	0.01	0.16	0.03	0.63	1.17	145	33.9	0.23	1.12
Viv-75331-4	0.62	0.02	0.06	0.01	0.04	0.02	0.01	0.05	0.01	0.07	0.02	0.10	0.01	0.15	0.02	0.58	1.26	86.6	18.2	0.21	1.06
Viv-37863-1	1.40	0.07	0.22	0.03	0.23	0.10	0.04	0.22	0.03	0.27	0.04	0.17	0.03	0.24	0.03	1.73	1.02	43.4	24.3	0.56	1.17
Viv-37863-2	1.19	0.06	0.17	0.03	0.15	0.07	0.03	0.20	0.02	0.20	0.04	0.13	0.03	0.21	0.02	1.36	1.03	51.5	29.2	0.57	1.02

$Y^* = Y_N/(½\ Dy_N + ½\ Ho_N)$, after Bolhar et al. (2004). Subscript 'N' stands for PAAS-normalized (Post-Archean Australian Shale, after Taylor and McLennan (1985)).

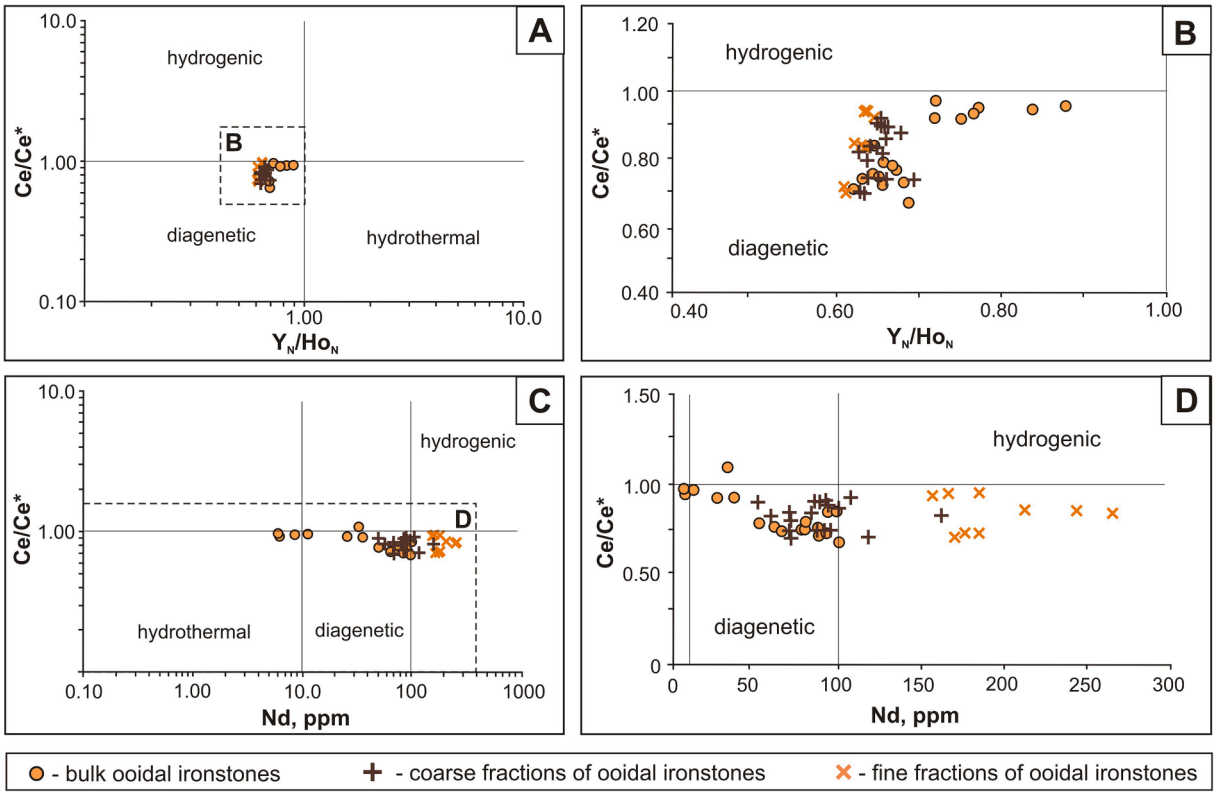

Fig. 16. Compositions of ooidal ironstones from the Kamysh-Burun deposit in Ce/Ce* – Nd (A) and Ce/Ce* – Y_N/Ho_N (B) diagrams. Different genetic types of marine Fe–Mn-(oxy)hydroxides according to (Bau et al., 2014).

precipitated with Fe^{3+}-(oxy)hydroxide films. The availability of both $(SO_4)^{2-}$ and Ca^{2+} in the growth medium may have been critical for the precipitation of relatively abundant least soluble LREE-rich phases. Most likely, the nucleation of LREE-Ca phosphate-sulfate was triggered by episodic inputs of oxygenated sea or brackish water (containing both $(SO_4)^{2-}$ and Ca^{2+}) into unconsolidated ooidal sediment that was exposed previously to suboxic-dysoxic conditions favorable for partial reduction of Fe^{3+} to Fe^{2+} and coupled desorption of LREE and $(PO_4)^{2-}$.

The Kerch ironstones lack authigenic LREE aluminophosphates typical of marine sediments, such as florencite ($CeAl_3(PO_4)_2(OH)_6$) or gorceixite ($(Ba,LREE)Al_3(PO_4)(PO_3OH)(OH)_6$). Only a single finding of rare microgranular Fe^{3+}-rich goyazite ($Sr(Al,Fe)_3(PO_4)_2(OH)_5{\cdot}H_2O$), Ca-rich svanbergite ($(Sr,Ca)Al_3(SO_4)(PO_4)(OH)_6$), Sr- and Pb-rich woodhouseite ($(Ca,Sr,Pb)Al_3(SO_4)(PO_4)(OH)_6$), and Sr- and Ba-rich hinsdalite ($(Pb,Sr,Ba)Al_3(SO_4)(PO_4)(OH)_6$) that filled cracks in brown ores was reported from the Old Karantin site (Chukanov, 2005). The lack of LREE aluminophosphates in the Kerch ores results from low Al_2O_3 contents and the absence of feldspar and mica, which are main sources of Al required for their formation (Rasmussen, 1996; Rasmussen et al., 1998). Furthermore, fluorine depletion of the growth environment led to the absence of common LREE carbonate-fluorides, such as bastnäsite ($Ce(CO_3)F$) or synchysite ($(CaREE(CO_3)_2F$) (Miyawaki and Nakai, 1996; Berger et al., 2008), as well as authigenic carbonate-fluorapatite. Note also the absence of Ce^{4+} oxide – cerianite ($(Ce,Th)O_2$) indicating strongly oxidizing conditions, for instance, in laterite profiles where its precipitation causes Ce fractionation from other trivalent REE (Berger et al., 2014). Cerianite was recently discovered among main Ce hosts in the Bakchar ooidal ironstones in West Siberia, where it may be responsible for Ce fractionation and for a distinct positive Ce* anomaly in the bulk samples (Fig. 13) (Rudmin et al., 2020a). Most of the samples we analyzed have REE spectra with a negative Ce* anomaly and lack cerianite. Therefore, the depositional history of Fe^{3+}-rich ooidal ironstones in the Kamysh-Burun deposit did not include the respective mineral formation events and/or diagenetic alteration in a highly oxidizing setting.

Thus, besides the adsorbed REEs (with marked MREE enrichment) predominant in the ΣREE budget, the Kerch ooidal ironstones contain disseminated LREE phosphates, including detrital Th-enriched monazite and authigenic Th-poor and Ca-enriched rhabdophane and rhabdophane-like phases. The fine fractions of ooidal ironstones are remarkable in the highest REE contents (with significant LREE and MREE enrichment and Y depletion; ΣREE = 699–1153 ppm) (Table 11; Fig. 13), which is mainly due to authigenic rhabdophane-like phases, specifically, the rhabdophane-tristramite series with Pr, Nd and Sm enrichment.

5.2. *The sources of iron and REE in the Kerch ooidal ironstones*

The net river flux to the oceans is considered to be a main source of REEs, along with submarine groundwater discharge (poorly documented up to now), submarine weathering of volcanic material, and unrecognized volcanic input. The bulk coagulated and suspended clay and Fe(Mn)-hydroxide particles with adsorbed REEs are removed from river water in estuarine and deltaic settings (Sholkovitz, 1995; Rasmussen et al., 1998; Maslov and Shevchenko, 2019). About 10% of ΣREE become remobilized during diagenesis of sediments and re-enter the water column (Sholkovitz, 1993). The REE river flux may be enhanced at the mouths of estuaries and deltas with REEs leached from particulate matter by seawater, but most of the released REEs may become rapidly re-adsorbed onto suspended particles and colloids (Rasmussen et al., 1998). The combination of conditions for co-precipitation and accumulation of REE-enriched Fe(Mn)-(oxy)hydroxides and/or clayey mud can be especially favorable in narrow gulfs, lagoons, and coastal wetlands where large rivers transport weathered material. Such paleogeographic settings optimal for accumulation of REE-enriched ooidal ironstones existed for a short time in the Early Pliocene (5.6–3.3 Ma) on

the northern border of the Paleo-Black Sea (Shnyukov, 1965; Kholodov et al., 2014).

In the time of Late Cenozoic deposition of ooidal ironstones, the Black Sea paleo-basin received most of its siliciclastic material from the Volhynian, Ukrainian, and Donetsk uplifts (low plateaus) on the northern periphery of the European Platform, which were dipping toward the Euxinian (Paleo Black Sea) Basin. The large paleo-river networks (Don, Dnieper, Danube, Dniester, and Bug) transported huge amounts of suspended and dissolved material into shallow basins of the northern East Paratethys. Cenozoic deposition in the region was fed by extensive weathering during Jurassic-Early Cretaceous, Paleogene, and Pliocene (Zanclean) events. Jurassic-Cretaceous weathered rocks, 2–6 to 60 m thick, cover almost the whole Ukrainian shield (~200,000 km^2); some weathering profiles are lateritic and enriched in Fe-(oxy)hydroxides. The Krivoy Rog Proterozoic jaspillite (with >83 wt% Fe_2O_3 and <14 wt% SiO_2) and mafic–ultramafic igneous complexes (12–14 wt% Fe_2O_3) of the Ukrainian shield have been commonly considered to be the main primary source of iron and some trace elements during the formation of ooidal ores (Muratov, 1964; Shnyukov, 1965; Popov et al., 2004, 2010; Kholodov et al., 2014).

As the sea level fell in the Mediterranean at 5.6 Ma, the Euxinian Sea dried from its northern outer shelf and shrunk. In Zanclean time (5.2–3.6 Ma), a system of connected fen bogs, freshened bays, and limans (lagoon-like brackish estuaries blocked by mouth-bar sediments) formed on the northern coast of the Black and Azov Seas (Muratov, 1964; Popov et al., 2010; Shnyukov, 1965; Kholodov et al., 2014). Iron and REE came to the Euxinian (Paleo Black Sea) restricted lagoons with particulate shuttle and colloids that large rivers drained from thick weathering profiles in the catchments of the southern Russian Platform. Note that the Ukrainian shield is one of Europe's largest metallogenic provinces of REEs mainly stored in granites, syenites, and their pegmatitic varieties, as well as in K-Na metasomatic rocks. Weathering of REE-rich rocks, transport and deposition of stable accessory minerals produced ilmenite-zircon-monazite placers of economic value in the Azov area (Kogarko et al., 1995; Gursky et al., 2005; Dubyna et al., 2014).

The greatest part of dissolved and colloidal matter entrained with rivers coagulated and precipitated on the saline/fresh water chemical barrier (Boyle et al., 1974; Sholkovitz, 1978; Gordeev and Lisitzin, 2014). Later the Fe-rich primary sediments were sorted and reworked by eustatically forced regression and redeposited, due to frequent storm activity. The redox regime in restricted lagoons oscillated from oxic to suboxic-dysoxic conditions and thus produced an oscillating lithological pattern with alternating Fe^{3+}-(oxy)hydroxide and Fe^{2+}-enriched illite–smectite or Fe-Mn carbonate rhythms.

The prevalent sources of REE stored in the Kerch ironstones were inferred from the Ce_N/Ce_N^* *vs* Nd and Ce_N/Ce_N^* *vs* Y_N/Ho_N bivariant diagrams for Fe(Mn)-rich marine sediments (Bau et al., 2014). All bulk samples of the Kerch ooidal ironstones and their coarse fractions show negative Ce anomalies at Nd concentrations between 51 and 100 ppm and a narrow range of Y_N/Ho_N ratios (0.64–0.69). They plot a compact cluster within the field of diagenetic marine Fe-Mn sediments (Fig. 16). The fine fractions with $Y_N/Ho_N = 0.64–0.69$ fall into the same area in the Ce_N/Ce_N^* *vs* Y_N/Ho_N diagram and are projected on the boundary between the diagenetic and hydrogenic fields in the Ce_N/Ce_N^* *vs* Nd diagram due to high Nd contents (107–266 ppm). The strong Nd enrichment of fine fractions appears to be due to the presence of Nd-rich authigenic LREE phosphate minerals (Table 3). This 'discrepancy' between the Ce_N/Ce_N^* *vs* Nd and Ce_N/Ce_N^* *vs* Y_N/Ho_N bivariant diagrams may be diagnostic of solids highly enriched in LREE and useful to discriminate other Fe-rich marine sediments. In general, most of REE + Y resources in the Kerch ooidal ironstones were scavenged from pore water during early diagenesis, while the siliciclastic inputs were minor, and no hydrothermal contribution has been revealed.

The Y_N/Ho_N ratios in the Fe^{2+} phosphates allow discriminating between clastic (~1.0) and hydrogenic/seawater (~1.8–2.0) sources of REEs (Chen et al., 2015). Since the average Y_N/Ho_N ratio of anapaite (2.17) fits that of sea water (~2.0) (Alibo and Nozaki, 1999), its limited REE + Y budget must be seawater-sourced. The shale-normalized REE + Y patterns of anapaite also strongly support the seawater source of rare earths incorporated into the mineral: anomalies in Ce (moderate negative) and Y (sharp positive), as well as high HREE enrichment (Fig. 14; Table 13). Vivianite shows smooth REE + Y patterns without Ce* and Y* anomalies. Widespread, although minor, LREE phosphates are authigenic minerals formed after the release of REEs and $(PO_4)^{3-}$ by reduction of Fe^{3+}-(oxy)hydroxides. Their localization inside allochems (as pore- and crack-filling precipitates) is evidence for the formation of the rhabdophane – tristramite phases postdating the allochem.

6. Conclusions

The reported data on mineralogy, major- and trace-element chemistry, and REE + Y patterns of the bulk Kerch ooidal ironstones and their constituents were used to estimate the depositional conditions and the contributions of various REE + Y carriers into the total ΣREE budget. These ironstones demonstrate efficient adsorptive scavenging of REE by Fe^{3+}-(oxy)hydroxides-dominated sediments, which occurred during multiple events of oxygenation and reduction. The ensuing hysteretic re-release and re-adsorption of REE by Fe^{3+}-(oxy)hydroxides after burial of Fe- and P-rich sediments eventually lead to REE accumulation with marked MREE enrichment. First, voluminous ultrafine Fe-rich mud, with a large total surface area of particles, coagulated on the geochemical barrier of fresh river and saline sea waters in limans and estuaries. Then the concentration of REE and P in pore waters of organic-rich coastal sediments increased greatly during early diagenesis, by the bacterial decomposition of organic matter, suboxic/anoxic reduction of Fe^{3+}-(oxy)hydroxides, and coupled leaching of adsorbed REEs and P. The early diagenetic processes in the Kerch ironstones are recorded in the presence of LREE hydrous phosphates and phosphate-sulfates, which became a new sink for LREE (with Pr, Nd, and Sm enrichment and depletion in Th and U) in lagoonal P-rich sediments. Due to preferential accumulation of authigenic LREE phosphates of rhabdophane-tristramite series (with Ce > La ≈ Nd ≈ Ca > Pr > Sm) in fine fractions, they are markedly enriched in ΣREE (*Xav* = 858 ppm, up to 1153 ppm) relative to other constituents of the Kerch ores.

The average ΣREE concentrations in the Kerch ooidal ironstones (~400 ppm) are commensurate with the respective amounts in the bulk ore samples from the giant Bakchar ooidal ironstones deposit in West Siberia (Rudmin et al., 2019, 2020a, 2020b) and the Chinese industrial ion-adsorbed clay (Wu et al., 1996; Bao and Zhao, 2008; Hatch, 2012; Kynicky et al., 2012; Wall, 2014), which store, respectively, an average of ~300 ppm and a range of 500–2000 ppm ΣREE. As ooidal ironstones are abundant worldwide and occur as geologically simple orebodies suitable for open-cast mining, these rock type may be of special interest as unconventional REE mineral resources.

Declaration of Competing Interest

The authors declare that they have no known competing financial interests or personal relationships that could have appeared to influence the work reported in this paper.

Acknowledgements

The manuscript benefited much from the encouraging support of Professor Franco Pirajno, Editor-in-Chief of Ore Geology Reviews, Professor Olga Plotinskaya, Associated editor of Ore Geology Reviews, and the thoughtful criticism of anonymous reviewers. We kindly appreciate the fruitful scientific collaboration of our colleagues from the Department of Marine Geology and Sedimentary Ore Formation, NAS of the Ukraine (Kiev, Ukraine) and personally academician Ye.F. Shnyukov. We would like to thank Prof. I.V. Pekov (Moscow State University,

Russia) and colleagues from Fersman Mineralogical Museum (Moscow, Russia) for providing historical samples of Fe^{2+}-bearing phosphate minerals from Kerch ironstone deposits. We further thank T. Perepelova as well as M. Khlestov and V. Danilovsky (IGM, Novosibirsk) for their helpful advice to the present work. The study was supported by the Russian Science Foundation, grant 17-17-01056P.

Appendix A. Supplementary data

Supplementary data to this article can be found online at https://doi.org/10.1016/j.oregeorev.2020.103827.

References

Afify, A.M., Sanz-Montero, M.E., Calvo, J.P., Wanas, H.A., 2015. Diagenetic origin of ironstone crusts in the lower Cenomanian Bahariya formation, Bahariya depression, Western Desert, Egypt. J. Afr. Earth Sci. 101, 333–349. https://doi.org/10.1016/j.jafrearsci.2014.10.005.

Afify, A.M., Sanz-Montero, M.E., Calvo, J.P., 2018. Differentiation of ironstone types by using rare earth elements and yttrium geochemistry – a case study from the Bahariya region, Egypt. Ore Geol. Rev. 96, 247–261. https://doi.org/10.1016/j.oregeorev.2018.04.019.

Alibo, D.S., Nozaki, Y., 1999. Rare earth elements in seawater: particle association, shale-normalization, and Ce oxidation. Geochim. Cosmochim. Acta 63 (3–4), 363–372.

Arbuzov, V.A., Bobrushkin, L.G., Litvinenko, A.U., Morokhovskaya M.S., Muratov, M.V., Naumenko, P.I., Nevoisa, G.G., 1967. The Kerch Iron Ore Basin. Nedra, Moscow, pp. 576. (in Russian).

Artemyev, D.A., Ankushev, M.N., 2019. Trace elements of Cu-(Fe)-sulfide inclusions in bronze age copper slags from South Urals and Kazakhstan: ore sources and alloying additions. Minerals 9, 746. https://doi.org/10.3390/min9120746.

Baioumy, H.M., Ahmed, A.H., Khedr, M.Z., 2014. A mixed hydrogenous and hydrothermal origin of the Bahariya iron ores, Egypt: evidences from the trace and rare earth element geochemistry. J. Geochem. Explor. 146, 149–162. https://doi.org/10.1016/j.gexplo.2014.08.008.

Baioumy, H., Omran, M., Fabritius, T., 2017. Mineralogy, geochemistry and the origin of high-phosphorus oolitic iron ores of Aswan, Egypt. Ore Geol. Rev. 80, 185–199. https://doi.org/10.1016/j.oregeorev.2016.06.030.

Balaram, V., 2019. Rare earth elements: a review of applications, occurrence, exploration, analysis, recycling, and environmental impact. Geosci. Front. 10 (4), 1285–1303. https://doi.org/10.1016/j.gsf.2018.12.005.

Bao, Z., Zhao, Z., 2008. Geochemistry of mineralization with exchangeable REY in the weathering crusts of granitic rocks in South China. Ore Geol. Rev. 33 (3–4), 519–535. https://doi.org/10.1016/j.oregeorev.2007.03.005.

Barker, S., 2007. Dynamics of fluid flow and fluid chemistry during crustal shortening (PhD thesis). The Australian National University, pp. 1–217.

Bau, M., Dulski, P., Möller, P., 1995. Yttrium and holmium in South Pacific seawater: vertical distribution and possible fractionation mechanisms. Chem. Erde 55, 1–15.

Bau, M., Koschinsky, A., 2009. Oxidative scavenging of cerium on hydrous Fe oxide: evidence from the distribution of rare earth elements and yttrium between Fe oxides and Mn oxides in hydrogenetic ferromanganese crusts. Geochem. J. 43 (1), 37–47. https://doi.org/10.2343/geochemj.1.0005.

Bau, M., Schmidt, K., Koschinsky, A., Hein, J., Kuhn, T., Usui, A., 2014. Discriminating between different genetic types of marine ferro-manganese crusts and nodules based on rare earth elements and yttrium. Chem. Geol. 381, 1–9. https://doi.org/10.1016/j.chemgeo.2014.05.004.

Bekker, A., Planavsky, N.J., Krapež, B., Rasmussen, B., Hofmann, A., Slack, J.F., Rouxel, O.J., Konhauser, K.O., 2014. Iron formations: their origins and implications for ancient seawater chemistry. In: Holland, H., Turekian, K. (Eds.), Treatise on Geochemistry, second ed. Elsevier Ltd, pp. 561–628. https://doi.org/10.1016/B978-0-08-095975-7.00719-1.

Berger, A., Gnos, E., Janots, E., Fernandez, A., Giese, J., 2008. Formation and composition of rhabdophane, bastnäsite and hydrated thorium minerals during alteration: implications for geochronology and low-temperature processes. Chem. Geol. 254 (3–4), 238–248. https://doi.org/10.1016/j.chemgeo.2008.03.006.

Berger, A., Janots, E., Gnos, E., Frei, R., Bernier, F., 2014. Rare earth element mineralogy and geochemistry in a laterite profile from Madagascar. Appl. Geochem. 41, 218–228. https://doi.org/10.1016/j.apgeochem.2013.12.013.

Bolhar, R., Kamber, B.S., Moorbath, S., Fedo, C.M., Whitehouse, M.J., 2004. Characterization of early Archaean chemical sediments by trace element signatures. Earth Planet. Sci. Lett. 222, 43–60. https://doi.org/10.1016/j.epsl.2004.02.016.

Boyle, E., Collier, R., Dengler, A.T., Edmond, J.M., Ng, A.C., Stallard, R.F., 1974. On the chemical mass-balance in estuaries. Geochim. Cosmochim. Acta 38 (11), 1719–1728. https://doi.org/10.1016/0016-7037(74)90188-4.

Byrne, R.H., Kim, K.H., 1990. Rare earth element scavenging in seawater. Geochim. Cosmochim. Acta 54 (10), 2645–2656. https://doi.org/10.1016/0016-7037(90)90002-3.

Carvalho, L., Monteiro, R., Figueira, P., Mieiro, C., Almeida, J., Pereira, E., Magalhães, V., Pinheiro, L., Vale, C., 2018. Vertical distribution of major, minor and trace elements in sediments from mud volcanoes of the Gulf of Cadiz: Evidence of Cd, As and Ba fronts in upper layers. Deep Sea Res Part I: Oceanogr. Res. Pap. 131, 133–143. https://doi.org/10.1016/j.dsr.2017.12.003.

Chakhmouradian, A.R., Zaitsev, A.N., 2012. Rare earth mineralization in igneous rocks: sources and processes. Elements 8 (5), 347–353. https://doi.org/10.2113/gselements.8.5.347.

Chakhmouradian, A.R., Wall, F., 2012. Rare earth elements: minerals, mines, magnets (and more). Elements 8 (5), 333–340. https://doi.org/10.2113/gselements.8.5.333.

Chen, J., Algeo, T.J., Zhao, L., Chen, Z.-Q., Cao, L., Zhang, L., Li, Y., 2015. Diagenetic uptake of rare earth elements by bioapatite, with an example from Lower Triassic conodonts of South China. Earth Sci. Rev. 149, 181–202. https://doi.org/10.1016/j.earscirev.2015.01.013.

Chukanov, N.V., 2005. Minerals of the Kerch iron-ore basin in Eastern Crimea. Mineralogical Almanac, vol. 8. Mineral. Almanac Association Ecost, Moscow, pp. 112.

Cutter, G.A., Moffett, J.G., Nielsdóttir, M.C., Sanial, V., 2018. Multiple oxidation state trace elements in suboxic waters off Peru: in situ redox processes and advective/diffusive horizontal transport. Mar. Chem. 201, 77–89. https://doi.org/10.1016/j.marchem.2018.01.003.

Dai, S.F., Yan, X.Y., Ward, C.R., Hower, J.C., Zhao, L., Wang, X., Zhao, L., Ren, D., Finkelman, R.B., 2018. Valuable elements in Chinese coals: a review. Int. Geol. Rev. 60, 590–620. https://doi.org/10.1080/00206814.2016.1197802.

De Carlo, E.H., Wen, X.-Y., Irving, M., 1997. The influence of redox reactions on the uptake of dissolved Ce by suspended Fe and Mn oxide particles. Aquat. Geochem. 3, 357–389. https://doi.org/10.1023/A:1009664626181.

Dubinin, A.V., 2004. Geochemistry of rare earth elements in the ocean. Lithol. Miner. Resour. 39, 289–307. https://doi.org/10.1023/B:LIMI.0000033816.14825.a2.

Dubyna, A.V., Kryvdik, S.G., Sharygin, V.V., 2014. Geochemistry of alkali and nepheline syenites of the Ukrainian Shield: ICP-MS data. Geochem. Int. 52 (10), 842–856. https://doi.org/10.1134/S0016702914080023.

Egger, M., Jilbert, T., Behrends, T., Rivard, C., Slomp, C.P., 2015. Vivianite is a major sink for phosphorus in methanogenic coastal surface sediments. Geochim. Cosmochim. Acta 169, 217–235. https://doi.org/10.1016/j.gca.2015.09.012.

Emsbo, P., McLaughlin, P.I., Breit, G.N., du Bray, E.A., Koenig, A.E., 2015. Rare earth elements in sedimentary phosphate deposits: solution to the global REE crisis? Gondwana Res. 27, 776–785. https://doi.org/10.1016/j.gr.2014.10.008.

Fan, H.R., Yang, K.F., Hu, F.F., Liu, S., Wang, K.Y., 2016. The giant Bayan Obo REE-Nb-Fe deposit, China: controversy and ore genesis. Geosci. Front. 7 (3), 335–344. https://doi.org/10.1016/j.gsf.2015.11.005.

Franceschelli, M., Puxeddu, M., Carta, M., 2000. Mineralogy and geochemistry of Late Ordovician phosphate-bearing oolitic ironstones from NW Sardinia, Italy. Mineral. Petrol. 69 (3–4), 267–293. https://doi.org/10.1007/s007100070024.

Garnit, H., Bouhlel, S., 2017. Petrography, mineralogy and geochemistry of the Late Eocene oolitic ironstones of the Jebel Ank, Southern Tunisian Atlas. Ore Geol. Rev. 84, 134–153. https://doi.org/10.1016/j.oregeorev.2016.12.026.

Gloaguen, E., Branquet, Y., Boulvais, P., Moëlo, Y., Chauvel, J.J., Chiappero, P.J., Marcoux, E., 2007. Palaeozoic oolitic ironstone of the French Armorican Massif: a chemical and structural trap for orogenic base metal-As-Sb-Au mineralisation during Hercynian strike-slip deformation. Miner. Deposita 42 (4), 399–422. https://doi.org/10.1007/s00126-006-0120-4.

Golubovskaya, E.V., 1997. Problem of the origin of the "caviar" near-share facies "roe" ores in iron ore deposits of the Kerch Peninsula. Lithol. Miner. Resour. 67, 661–667 (in Russian).

Golubovskaya, E.V., 1999. Origin of the "brown" ore in iron ore deposits of the Kerch Peninsula. Lithol. Miner. Resour. 3, 244–251 (in Russian).

Golubovskaya, E.V., 2001. Facies and geochemical features of the iron ore complex of the Kerch Peninsula. Lithol. Miner. Resour. 36 (3), 224–235. https://doi.org/10.1023/A:1010425324458.

Golubovskaya, E.V., 2003. Some geochemical features of iron ores from the Lisakov deposit. Lithol. Miner. Resour. 38, 275–281. https://doi.org/10.1023/A:1023920812064.

Gordeev, V.V., Lisitzin, A.P., 2014. Geochemical interaction between the freshwater and marine hydrospheres. Russ. Geol. Geophys. 55 (5–6), 562–581. https://doi.org/10.1016/j.rgg.2014.05.004.

Gursky D.S., Esipchuk K.E., Kalinin V.I., Kulish E.A., 2005. Metal and non-metallic minerals of Ukraine, vol. 1. Center of Europe, Kiev and Lviv, pp. 783. (In Russian).

Hatch, G.P., 2012. Dynamics in the global market for rare earths. Elements 8 (5), 341–346. https://doi.org/10.2113/gselements.8.5.341.

Hsu, T.W., Jiang, W.T., Wang, Y., 2014. Authigenesis of vivianite as influenced bymethaneinduced sulfidization in cold-seep sediments off southwestern Taiwan. J. Asia Earth Sci. 89, 88–97. https://doi.org/10.1016/j.jseaes.2014.03.027.

Jeffery, P.G., 1970. In: Chemical Methods of Rock Analysis. Pergamon Press, Oxford and New York, p. 507.

Kafle, B., 2011. Stratigraphy, petrography and geochemistry of the Bad Heart Formation, Northwestern Alberta (Ms thesis). University of Alberta, Edmonton, p. 150. https://doi.org/10.7939/R31P5Z.

Kholodov, V.N., Golubovskaya, E.V., Nedumov, R.I., 2014. Origin and prospects of the Cimmerian iron ore basin in Ukraine and Russia. Lithol. Miner. Resour. 49 (5), 383–405. https://doi.org/10.1134/S0024490214050046.

Kim, J.H., Torres, M.E., Haley, B.A., Kastner, M., Pohlman, J.W., Riedel, M., Lee, Y.J., 2012. The effect of diagenesis and fluid migration on rare earth element distribution in pore fluids of the northern Cascadia accretionary margin. Chem. Geol. 291, 152–165. https://doi.org/10.1016/j.chemgeo.2011.10.010.

Kogarko, L.N., Kononova, V.A., Orlova, M.P., Wooley, A.R., 1995. In: Alkaline Rocks and Carbonatites of the World. Part Two: Former USSR. Chapman & Hall, London and New York, p. 226.

Kokh, S.N., Shnyukov, E.F., Sokol, E.V., Novikova, S.A., Kozmenko, O.A., Semenova, D.V., Rybak, E.N., 2015. Heavy carbon travertine related to methane generation: a case

study of the Big Tarkhan cold spring, Kerch Peninsula, Crimea. Sediment. Geol. 325, 26–40. https://doi.org/10.1016/j.sedgeo.2015.05.005.
Krenn, E., Finger, F., 2007. Formation of monazite and rhabdophane at the expense of allanite during Alpine low temperature retrogression of metapelitic basement rocks from Crete, Greece: microprobe data and geochronological implications. Lithos 95 (1–2), 130–147. https://doi.org/10.1016/j.lithos.2006.07.007.
Krishnamurthy, N., Gupta, C.K., 2005. In: Extractive Metallurgy of Rare Earths. CRC Press, Boca Raton, p. 504.
Kynicky, J., Smith, M.P., Xu, C., 2012. Diversity of rare earth deposits: the key example of China. Elements 8 (5), 361–367. https://doi.org/10.2113/gselements.8.5.361.
Lakshtanov, L.Z., Stipp, S.L.S., 2004. Experimental study of europium (III) coprecipitation with calcite. Geochim. Cosmochim. Acta 68 (4), 819–827. https://doi.org/10.1016/j.gca.2003.07.010.
Li, F., Webb, G.E., Algeo, T.J., Kershaw, S., Lu, C., Oehlert, A.M., Gong, Q., Pourmand, A., Tan, X., 2019. Modern carbonate ooids preserve ambient aqueous REE signatures. Chem. Geol. 509, 163–177. https://doi.org/10.1016/j.chemgeo.2019.01.015.
Lugovskaya, I.G., Alikberov, V.M., Pechenkin, I.G., Tigunov, L.P., 2015. Contribution of VIMS to the investigation of Kerchian iron ores. Explor. Prot. Miner. Res. 2, 3–11 (in Russian).
Malakhovsky, V.F., 1956. In: Geology and Geochemistry of Iron Ores and their Major Components. Publishing House of Academy of Sciences Ukrainian SSR, Kiev, p. 210 (in Russian).
Mariano, A.N., Mariano, A., 2012. Rare earth mining and exploration in North America. Elements 8 (5), 369–376. https://doi.org/10.2113/gselements.8.5.369.
Maslov, A.V., Shevchenko, V.P., 2019. REE-Th systematics of the suspended particulate matter and bottom sediments from the mouth zones of the world rivers of different categories/classes and some large Russian Arctic rivers. Geochem. Int. 57 (1), 56–73. https://doi.org/10.1134/S0016702919010075.
Melton, E.D., Swanner, E.D., Behrens, S., Schmidt, C., Kappler, A., 2014. The interplay of microbially mediated and abiotic reactions in the biogeochemical Fe cycle. Nat. Rev. Microbiol. 12, 797–808. https://doi.org/10.1038/nrmicro3347.
Miyawaki, R., Nakai, I., 1996. Crystal chemical aspects of rare earth minerals. In: Jones, A.P., Wall, F., Williams, C.T. (Eds.), Rare Earth Minerals. The Mineralogical Society Series. Chapman and Hall, London, pp. 21–40.
Mosar, J., Kangarli, T., Bochud, M., Glasmacher, U.A., Rast, A., Brunet, M.F., Sosson, M., 2010. Cenozoic-Recent tectonics and uplift in the Greater Caucasus: a perspective from Azerbaijan. In: Sosson, M., Kaymakci, N., Stephenson, A., Bergerat, F., Starostenko, V. (Eds.), Sedimentary basin tectonics from the Black Sea and Caucasus to the Arabian Platform, Geological Society Special Publications. MPG Books Ltd, Bodmin, pp. 261–280. https://doi.org/10.1144/SP340.12.
Muratov, M.V., 1964. Paleogeography of the Cimmerian Age (Middle Pliocene) in the Black Sea-Caspian basin. Lithol. Miner. Resour. 4, 3–20 (in Russian).
Nedumov, R.I., 1994. Lithology, geochemistry, and paleogeography of Cenozoic deposits in the Caucasus foothills. Lithol. Miner. Resour. 1, 69–77 (in Russian).
Novoselov, K.A., Belogub, E.V., Kotlyarov, V.A., Filippova, K.A., Sadykov, S.A., 2018. Mineralogical and geochemical features of oolitic ironstones from the Sinara-Techa deposit, Kurgan district, Russia. Geol. Ore Depos. 60 (3), 265–276. https://doi.org/10.1134/S1075701518030066.
Ohta, A., Kawabe, I., 2000. Rare earth element partitioning between Fe oxyhydroxide precipitates and aqueous NaCl solutions doped with $NaHCO_3$: determinations of rare earth element complexation constants with carbonate ions. Geochem. J. 34, 439–454. https://doi.org/10.2343/geochemj.34.439.
Ohta, A., Kawabe, I., 2001. REE(III) adsorption onto Mn dioxide (δ-MnO_2) and Fe oxyhydroxide: Ce(III) oxidation by δ-MnO_2. Geochim. Cosmochim. Acta 65, 695–703. https://doi.org/10.1016/S0016-7037(00)00578-0.
Paton, C., Hellstrom, J., Paul, B., Woodhead, J., Hergt, J., 2011. Iolite: freeware for the visualisation and processing of mass spectrometric data. J. Anal. At. Spectrom. 26, 2508–2518.
Philip, H., Cisternas, A., Gvishiani, A., Gorshkov, A., 1989. The Caucasus: an actual example of the initial stages of continental collision. Tectonophys. 161 (1–2), 1–21. https://doi.org/10.1016/0040-1951(89)90297-7.
Popov, S.V., Rögl, F., Rozanov, A.Y., Steininger, F.F., Shcherba, I.G., Kováč, M., 2004. Lithological-paleogeographic maps of Paratethys. 10 maps Late Eocene to Pliocene. E.Schweizerbrat'sche Verlagsbuchhandlung, Stuttgart, pp. 73.
Popov, S.V., Antipov, M.P., Zastrozhnov, A.S., Kurina, E.E., Pinchuk, T.N., 2010. Sea-level fluctuations on the northern shelf of the Eastern Paratethys in the Oligocene-Neogene. Stratigr. Geol. Correl. 18 (2), 200–224. https://doi.org/10.1134/S0869593810020073.
Quinn, K.A., Byrne, R.H., Schijf, J., 2006a. Sorption of yttrium and rare earth elements by amorphous ferric hydroxide: influence of pH and ionic strength. Mar. Chem. 99 (1–4), 128–150. https://doi.org/10.1016/j.marchem.2005.05.011.
Raiswell, R., Canfield, D.E., 2012. The iron biogeochemical cycle past and present. Geochem. Perspect. 1 (1), 156 pp. https://doi.org/10.7185/geochempersp.1.1.
Quinn, K.A., Byrne, R.H., Schijf, J., 2006b. Sorption of yttrium and rare earth elements by amorphous ferric hydroxide: influence of solution complexation with carbonate. Geochim. Cosmochim. Acta 70 (16), 4151–4165. https://doi.org/10.1016/j.gca.2006.06.014.
Rahiminejad, A.H., Zand-Moghadam, H., 2018. Synsedimentary formation of ooidal ironstone: an example from the Jurassic deposits of SE central Iran. Ore Geol. Rev. 95, 238–257. https://doi.org/10.1016/j.oregeorev.2018.02.028.
Rasmussen, B., 1996. Early-diagenetic REE-phosphate minerals (florencite, gorceixite, crandallite, and xenotime) in marine sandstones: a major sink for oceanic phosphorus. Am. J. Sci. 296, 601–632. https://doi.org/10.2475/ajs.296.6.601.
Rasmussen, B., Buick, R., Taylor, W.R., 1998. Removal of oceanic REE by authigenic precipitation of phosphatic minerals, Earth Planet. Sci. Lett. 164, 135–149. https://doi.org/10.1016/S0012-821X(98)00199-X.
Rollinson, H., 1993. In: Using Geochemical Data: Evolution, Presentation, Interpretation. Longman Scientific & Technica, Harlow, Essex, England: New York, p. 352.
Romanek, C.S., Jiménez-López, C., Navarro, A.R., Sánchez-Román, M., Sahai, N., Coleman, M., 2009. Inorganic synthesis of Fe-Ca-Mg carbonates at low temperature. Geochim. Cosmochim. Acta 73, 5361–5376. https://doi.org/10.1016/j.gca.2009.05.065.
Rothe, M., Kleeberg, A., Hupfer, M., 2016. The occurrence, identification and environmental relevance of vivianite in waterlogged soils and aquatic sediments. Earth Sci. Rev. 158, 51–64. https://doi.org/10.1016/j.earscirev.2016.04.008.
Rudmin, M., Banerjee, S., Abdullayev, E., Ruban, A., Filimonenko, E., Lyapina, E., Kashapov, R., Mazurov, A., 2020a. Ooidal ironstones in the Meso-Cenozoic sequences in western Siberia: assessment of formation processes and relationship with regional and global earth processes. J. Palaeogeogr. 9, 1–21. https://doi.org/10.1186/s42501-019-0049-z.
Rudmin, M., Mazurov, A., Banerjee, S., 2019. Origin of ooidal ironstones in relation to warming events: Cretaceous-Eocene Bakchar deposit, South-East Western Siberia. Mar. Pet. Geol. 100, 309–325. https://doi.org/10.1016/j.marpetgeo.2018.11.023.
Rudmin, M., Reva, I., Sokol, E., Abdullayev, E., Ruban, A., Kudryavtsev, A., Tolkachev, O., Mazurov, A., 2020b. Minerals of rare earth elements in high-phosphorus ooidal ironstones of the Western Siberia and Turgai Depression. Mineral 10 (1), 11. https://doi.org/10.3390/min10010011.
Rudnick, R.L., Gao, S., 2003. Composition of the continental crust. In: Rudnick, R.L. (Ed.), Treatise on Geochemistry. Elsevier, Amsterdam, pp. 1–64. https://doi.org/10.1016/B0-08-043751-6/03016-4.
Rue, E.L., Smith, G.J., Cutter, G.A., Bruland, K.W., 1997. The response of trace element redox couples to suboxic conditions in the water column. Deep-Sea Res. 44, 113–134.
Ruttenberg, K.C., 2003. The global phosphorus cycle. In: Holland, H., Turekian, K. (Eds.), Treatise on Geochemistry. Elsevier Ltd, pp. 585–643.
Salama, W., El Aref, M., Gaupp, R., 2012. Mineralogical and geochemical investigations of the middle Eocene ironstones, El Bahariya depression, Western Desert, Egypt. Gondwana Res. 22 (2), 717–736. https://doi.org/10.1016/j.gr.2011.11.011.
Schmidt, M., Stumpf, T., Walther, C., Geckeis, H., Fanghänel, T., 2009. Incorporation versus adsorption: substitution of Ca^{2+} by Eu^{3+} and Cm^{3+} in aragonite and gypsum. Dalton Trans. 33, 6645–6650. https://doi.org/10.1039/b822656c.
Seredin, V.V., Dai, S., 2012. Coal deposits as potential alternative sources for lanthanides and yttrium. Int. J. Coal. Geol. 94, 67–93. https://doi.org/10.1016/j.coal.2011.11.001.
Shannon, R.D., 1976. Revised effective ionic radii and systematic studies of interatomic distances in halides and chalcogenides. Acta crystallogr. Sect. A: Cryst. Phys., Diffr., Theor. Gen. Crystallogr. 32 (5), 751–767.
Shatsky, V., Sitnikova, E., Kozmenko, O., Palessky, S., Nikolaeva, I., Zayachkovsky, A., 2006. Behavior of incompatible elements during ultrahigh-pressure metamorphism (by the example of rocks of the Kokchetav massif). Russ. Geol. Geophys. 47, 482–496.
Shnyukov, E.F., 1965. The genesis of the Cimmerian iron ores of the Azov-Black Sea ore province. Naukova Dumka, Kiev, pp. 195. (in Russian).
Shnyukov, E., Sheremetiev, V., Maslakov, N., Kutniy, V., Gusakov, I., Trofimov, V., 2005. In: Mud Volcanoes of the Kerch-Taman Region. GlavMedia Publishing House, Krasnodar, p. 173 (in Russian).
Sholkovitz, E.R., 1978. The flocculation of dissolved Fe, Mn, Al, Cu, Ni, Co and Cd during estuarine mixing. Earth Planet. Sci. Lett. 41 (1), 77–86. https://doi.org/10.1016/0012-821X(78)90043-2.
Sholkovitz, E.R., 1993. The geochemistry of rare earth elements in the Amazon River estuary. Geochim. Cosmochim. Acta 57 (10), 2181–2190. https://doi.org/10.1016/0016-7037(93)90559-F.
Sholkovitz, E.R., 1995. The aquatic chemistry of rare earth elements in rivers and estuaries. Aquat. Geochem. 1 (1), 1–34. https://doi.org/10.1007/BF01025229.
Smith, A. J. B., Gutzmer, J., Beukes, N. J., Reinke, C., Bau, M., 2008. Rare earth elements (REE) in Banded Iron Formations – link between geochemistry and mineralogy. In: Australasian Institute of Mining and Metallurgy Publication Series 2008, 9th International Congress for Applied Mineralogy, ICAM 2008; Brisbane, QLD; Australia; 8 September 2008 through 10 September 2008, pp. 651-658.
Sokol, E.V., Kokh, S.N., Kozmenko, O.A., Novikova, S.A., Khvorov, P.V., Nigmatulina, E. A., Belogub, E.V., Kirillov, M.V., 2018. Mineralogy and geochemistry of mud volcanic ejecta: a new look at old issues (a case study from the Bulganak field, Northern Black Sea). Mineral 8 (8), 344. https://doi.org/10.3390/min8080344.
Sokol, E.V., Kokh, S.N., Kozmenko, O.A., Lavrushin, V.Y., Belogub, E.V., Khvorov, P.V., Kikvadze, O.E., 2019. Boron in an onshore mud volcanic environment: case study from the Kerch Peninsula, the Caucasus continental collision zone. Chem. Geol. 525, 58–81. https://doi.org/10.1016/j.chemgeo.2019.07.018.
Sposito, G., Skipper, N.T., Sutton, R., Park, S.H., Soper, A.K., Greathouse, J.A., 1999. Surface geochemistry of the clay minerals. Proc. Nat. Acad. Sci. 96 (7), 3358–3364. https://doi.org/10.1073/pnas.96.7.3358.
Sturesson, U., 2003. Lower Palaeozoic iron oolites and volcanism from a Baltoscandian perspective. Sediment. Geol. 159, 241–256. https://doi.org/10.1016/S0037-0738(02)00330-5.
Surya Prakash, S.L., Ray, D., Paropkari, A.L., Mudholkar, A.V., Satyanaraynan, M., Sreenivas, B., Chandrasekharam, D., Kota, Dalayya, Raju, Kamesh, Sujata Kaisary, K. A., Balaram Gurav, V Tripti, 2012. Distribution of REEs and yttrium among major geochemical phases of marine Fe-Mn-oxides: comparative study between hydrogenous and hydrothermal deposits. Chem. Geol. 312–313, 127–137. https://doi.org/10.1016/j.chemgeo.2012.03.024.
Taylor, S.R., McLennan, S.M., 1985. In: The Continental Crust: Its Evolution and Composition. Blackwell Scientific Publications, Oxford, p. 312.

Taylor, K.G., Konhauser, K.O., 2011. Iron in Earth surface systems: a major player in chemical and biological processes. Elements 7, 83–88. https://doi.org/10.2113/gselements.7.2.83.

Tsipursky, S.I., Golubovskaya, E.V., 1989. Smectites of "tobacco" ores of the Kerch deposits. Lithol. Miner. Resour. 2, 58–73 (in Russian).

USEPA, 2007. Method 3051A – microwave assisted acid digestion of sediments. Sludges, Soils, and Oils 1–30.

Wall, F., 2014. Rare earth elements. In: Gun, G. (Ed.), Critical Metals Handbook, first ed. John Wiley & Sons, Ltd, pp. 312–339.

Wang, J., Shen, S., Kang, J., Li, H., Guo, Z., 2010. Effect of ore solid concentration on the bioleaching of phosphorus from high-phosphorus iron ores using indigenous sulfur-oxidizing bacteria from municipal wastewater. Process Biochem. 45, 1624–1631. https://doi.org/10.1016/j.procbio.2010.06.013.

Williams-Jones, A.E., Migdisov, A.A., Samson, I.M., 2012. Hydrothermal mobilisation of the rare earth elements – a tale of "ceria" and "yttria". Elements 8 (5), 355–360. https://doi.org/10.2113/gselements.8.5.355.

Wu, C., Yuan, Z., Bai, G., 1996. Rare earth deposits in China. In: Jones, A.P., Wall, Frances, Williams, C.T. (Eds.), Rare EARTH Minerals-chemistry, Origin and Ore Deposits. The Mineralogical Society Series. Chapman and Hall, London, pp. 281–310.

Xiao, Y., Huang, L., Long, Z., Feng, Z., Wang, L., 2016. Adsorption ability of rare earth elements on clay minerals and its practical performance. J. Rare Earths 34 (5), 543–548. https://doi.org/10.1016/S1002-0721(16)60060-1.

Yang, J., Torres, M., McManus, J., Algeo, T.J., Hakala, J.A., Verba, C., 2017. Controls on rare earth element distributions in ancient organic-rich sedimentary sequences: role of post-depositional diagenesis of phosphorus phases. Chem. Geol. 466, 533–544. https://doi.org/10.1016/j.chemgeo.2017.07.003.

Young, T.P., 1989. Phanerozoic ironstones: an introduction and review. In: Young, T.P., Gordon Taylor, W.E. (Eds.), Phanerozoic Ironstones. Geological Society Special Publications. Alden Press, Oxford, pp. ix–xxv. https://doi.org/10.1144/GSL.SP.1989.046.01.02.

Zhao, Y., Zhou, Y., Zhang, J., Zheng, C., 2019. Trace element resource recovery from coal and coal utilization by-products. In: Zhao, Y., Li, H., Yang, J., Zheng, C. (Eds.), Emission and Control of Trace Elements from Coal-derived Gas Streams. Woodhead Publishing, p. 424. https://doi.org/10.1016/b978-0-08-102591-8.00009-x.

Zitzmann, A., 1978. The iron ore deposits of Europe and adjacent areas: explanatory notes to the International Map of the iron ore deposits of Europe, 1:2500000. Bundesanstalt für Geowissenschaften und Rohstoffe, Hannover, pp. 386.

Zonenshain, L.P., Le Pichon, X., 1986. Deep basins of the Black Sea and Caspian Sea as remnants of Mesozoic back-arc basins. Tectonophys. 123, 181–240. https://doi.org/10.1016/0040-1951(86)90197-6.